THESIS

CHARACTERIZATION OF DIRECT INJECTED PROPANE AND ISO-OCTANE SPRAY AT ENGINE-LIKE CONDITIONS IN A HIGH-PRESSURE SPRAY CHAMBER

Submitted By

Brye Thomas Windell

Department of Mechanical Engineering

In partial fulfillment of the requirements

For the Degree of Master of Science

Colorado State University

Fort Collins, Colorado

Spring 2022

Master's Committee:

Advisor: Bret C Windom

Daniel Olsen
Subhas Karan Venayagamoorthy

ABSTRACT

CHARACTERIZATION OF DIRECT INJECTED PROPANE AND ISO-OCTANE SPRAY AT ENGINE-LIKE CONDITIONS IN A HIGH-PRESSURE SPRAY CHAMBER

This thesis focuses on the recommission, modification, and testing of a high-pressure spray chamber (HPSC) and its role in aiding the experimental and numerical examination of direct injection (DI) propane at various engine-like conditions to address fundamental limitations of achieving near diesel efficiencies in heavy duty on-road liquified petroleum gas (LPG) engines. The HPSC was reconstructed and is capable of incorporating optical diagnostic techniques including high-speed Schlieren and planar Mie scattering imaging. High-speed Schlieren was used to characterize the global spray morphology and vapor phase regions while planar Mie scattering allowed for individual plume resolution providing insights into the liquid regions of the spray. These optical imaging techniques unveiled propane's spray propagation was fed by flash boiling effects, spray collapse, and high degree of vaporization, unlike iso-octane. This resulted in a direct proportionality of propane's penetration length to temperature, an inversely proportional relationship to ambient pressure, and a direct proportionality to injection pressure. Contrary to propane, iso-octane's spray morphology exhibited minor changes as temperatures and pressures were varied. Due to these unique effects, flash boiling, spray collapse, and high degree of vaporization, propane is classified as an unconventional spray, dissimilar to iso-octane's spray morphology. Experimental testing provided corrections to numerical models that were developed to reproduce the under-expanded jet dynamics. The numerical modeling results were found to be sensitive to cone and inclusion angles. The current work serves as preliminary

results for an experimental validation campaign which aid in the numerical model development for future heavy duty on-road LPG engines.

ACKNOWLEDGEMENTS

The author would like to acknowledge and thank the unwavering support, direction, and trust of his advisor Dr. Bret Windom. The author would also like to acknowledge and thank the support of Manav Sharma for his help in data collection, processing, and assistance in the lab. The author would also like to thank the committee members, Dr. Daniel Olsen and Dr. Subhas Karan Venayagamoorthy for the opportunity to present this thesis. The author would also like to thank his colleagues at the Powerhouse for their help and constructive conversations. The author would also like to thank Lorenzo Nocivelli and Katherine Asztalos for the extensive work and effort on the computational modeling and analysis front.

The author is very thankful for the unwavering support and guidance of his family (Brad, Heidi, and Bridgette) and friends over the past two years.

This research is funded by the U.S. Department of Energy under grant number DE-EE0009198.

TABLE OF CONTENTS

LIST OF FIGURES

Chapter 1 - Introduction

1.1 Thesis Focus

This thesis focuses on the recommission and design of a high-pressure spray chamber (HPSC) and its role in aiding an experimental and numerical investigation of directly injected propane at engine-like conditions. Additionally, this thesis is a contributing effort to help understand the fundamental limitations to achieve near diesel efficiencies in a heavy duty on-road direct injected liquified petroleum gas (LPG) engine platform. The Department of Energy is funding multiple sub-projects, contributing to the understanding of direct injection (DI) using LPG within an engine. The project as a whole will utilize: (1) a rapid compression machine (RCM) and laser ignition system, that will measure laminar flame speed and end gas autoignition (EGAI) at engine like conditions, (2) a high pressure spray chamber (HPSC), to study injection penetration, vaporization, and mixing, (3) a cooperative fuel research (CFR) engine to examine knock propensity, end gas recirculation (EGR) limits, emission trade-offs, and controlled end gas autoignition (C-EGAI), and (4) a Cummins single cylinder 2.5 L heavy duty research engine, to demonstrate near-diesel efficiencies using a final combustion/control recipe.

The first part of this thesis gives an overview of issues within the heavy-duty on-road vehicle industry today and the use of LPG as a potential solution. A few challenges associated with LPG are misfires and knock, which decrease the vehicles overall efficiency. These issues can be mitigated by the incorporation of C-EGAI and EGR. The second part of this thesis describes the recommission and updates made to the HPSC. This section also explains the methodology and equipment used to conduct high-speed Schlieren and planar Mie scattering experiments to investigate iso-octane and propane and their spray structures. This section also provides the methodology and setup behind the numerical investigation. The third part of this thesis presents both the experimental and numerical results. The experimental results obtained through Schlieren and planar Mie imaging help direct the numerical modeling techniques to capture the unconventional spray structure of propane accurately. Finally, conclusions and future research, present potential methods that can be used to further characterize propane's spray characteristics.

1.2 Issues with Heavy Duty on-road Engines

Development of new combustion technologies and alternative transportation platforms are areas of interest to help reduce greenhouse gas emissions (GHG) and other pollutants. The most recent Intergovernmental Panel on Climate Change (IPCC) revealed that if GHG are not significantly reduced in the next several decades, an expected or greater than 1.5 °C increase in the global-mean temperature will be expected [1]. The United States' plans to reach net zero emission economy-wide by 2050, indicating that all transportation sectors need to make efforts to reduce CO_2 emissions [2]. Electrification of vehicles supplied by renewable electricity, is taking the United States by storm and becoming a popular alternative for passenger and light-duty vehicles but, with the lack of charging infrastructure and high initial cost, these issues prove to be challenges for the heavy-duty transportation sector. Additionally, there are concerns regarding the power densities of batteries, and their ability to meet the high expectations of long-range transportation for internal combustion vehicles [3]. To combat these issues, automobile and trucking manufactures have shifted their focus to reducing emissions and improving fuel economy in hybrid and diesel vehicles [4], [2].

Heavy duty on-road engines are a vital part of the economy, transporting goods and other products across the country. Heavy duty on-road vehicles transported roughly 72.5% of the nation's freight by weight in 2020. Within the transportation sector, 36.5 billion gallons of diesel were consumed and around a quarter of GHG emissions were produced in 2019 by medium and heavy-duty vehicles in the United States [5], [6]. Additionally, heavy-duty vehicles are responsible for a larger amount of emissions that are harmful to the environment, such as nitrogen oxides (NO_X) and particulate matter (PM).

Heavy-duty vehicles are mainly powered by diesel engines due to their ability to provide a high power-to-weight ratio and torque that is needed to transport extremely heavy loads. Diesel combustion utilizes compression ignition engines which are able to produce thermal efficiencies up to 45% [7]. Compression ignition engines inject diesel fuel close to the end of the compression stroke of a 4-cycle engine, where only air is drawn in during the intake stroke. A fundamental issue arises when operating heavy-duty diesel engines, where NO_X is largely produced due to higher combustion temperatures at lean mixtures. To reduce the production of NO_X and produce a stochiometric mixture, more fuel is injected. While the added fuel creates a stochiometric mixture, and reduces NO_X, combustion temperatures are decreased causing an increase in PM. This issue has been referred as 'The Diesel Dilemma' and the PM-NO_X trade-off [8], [9]. To reduce NO_X and PM further, aftertreatment systems (ATS) are added to the vehicle but, with regulations growing more stringent more or larger ATS will be needed, causing more expensive and complicated engine platforms. Alternatively, spark ignited engines (SI) utilize gasoline blends that are mixed with air during the intake stroke. This fuel/air mixture is then ignited with a spark plug creating a suitable combustion event which produce less PM and NO_x emissions compared to diesel counterparts. Although less emissions are produced, the power densities and fuel efficiencies of this premixed air and gasoline blend, are reduced due to knock and misfire occurrences in the engine. Utilizing direct injection techniques in a SI engine help increase the efficiency, decrease fuel consumption, and reduce emissions further. The following sections provide insight into injection techniques, strategies, and how coupling traditional and alternative fuels with these techniques can further improve efficiency and decrease emissions.

1.3 Types of Injection Methods

There have been numerous injection techniques implemented in internal combustion engines (ICE) over the last century. With technology improving through the decades, engines have become more efficient, cleaner burning, and producing less emissions. Fuel delivery/injection techniques such as carburetors, throttle-body injection, multiport injection, direct injection, and compression ignition/injection have all been used in light, medium, and heavy-duty engines. This thesis will address a few of these injection techniques and their benefits to reducing emissions and increasing efficiency.

1.3.1 Compression Ignition/Injection

Compression ignition (CI) engines in their simplest form utilize direct injection (DI) to inject fuels such as diesel into the cylinder near top dead center. Once the fuel is injected into the cylinder extreme pressures and temperatures will cause controlled autoignition of the fuel, producing power for the engine. Compression ignition engines utilize a high compression ratio compressing air as much as 14:1 to 22:1 [10], [11]. The type of fuel used within a compression ignition engine is extremely important for the correct operation of the engine. Fuels such as diesel, heavy fuel oils, biodiesels, and vegetable oils provide good physical and chemical properties for autoignition hence, their usage in compression ignition engines. A general schematic demonstrating the inner workings of a compression ignition engine are seen in Figure 1-1. Injectors used in compression ignition engines usually operate at pressures of 700 – 2100 bar (10,000 – 30,000 psi), providing homogenous mixing within the chamber [10], [12], [13].

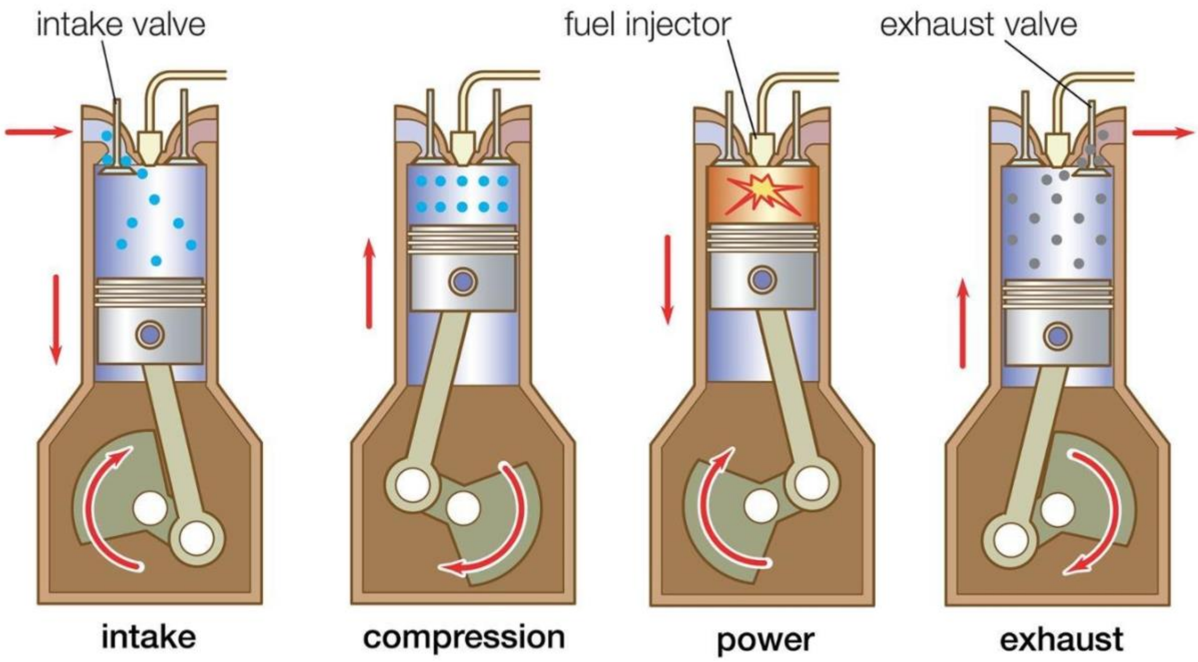

Figure 1-1 Compression ignition/injection engine cycles [14]. Displaying the intake stroke drawing in only air. The compression stroke compresses the air to extreme temperatures and pressures. Near top dead center, fuel is injected into the cylinder, and the fuel/air mixture auto-ignites. The exhaust stoke releases the spend gases

Compression ignition engines operate at high pressures and temperatures which in turn help the efficiency of the engine. The main downside to compression ignition engines is the higher production of PM and NOx compared to their spark ignited gasoline engine counterparts.

1.3.2 <u>Multiport Fuel Injection</u>

Multiport injection utilizes a fuel injector in each intake port. This provides the ability to time injection events when the intake valve is opening and the piston is in the intake stoke phase, which will draw in air and fuel as shown in Figure 1-2. This technique allows for fuel to be injected into each intake port wasting less fuel compared to other injection techniques such as carbureted or throttle-body injection. Multiport injection usually injects fuels at pressures around 2.5 – 4.5 bar (35 to 65 psi) [15], [16]. With less fuel being consumed, the vehicle is more efficient and economical. Multiport injection also poses multiple issues that influence the efficiency of the vehicle. As the fuel is drawn into the cylinder small amounts of fuel are deposited on the walls of the inlet port and the intake valve. This issue can cause carbon build up on the intake valve reducing air and fuel flow into the cylinder.

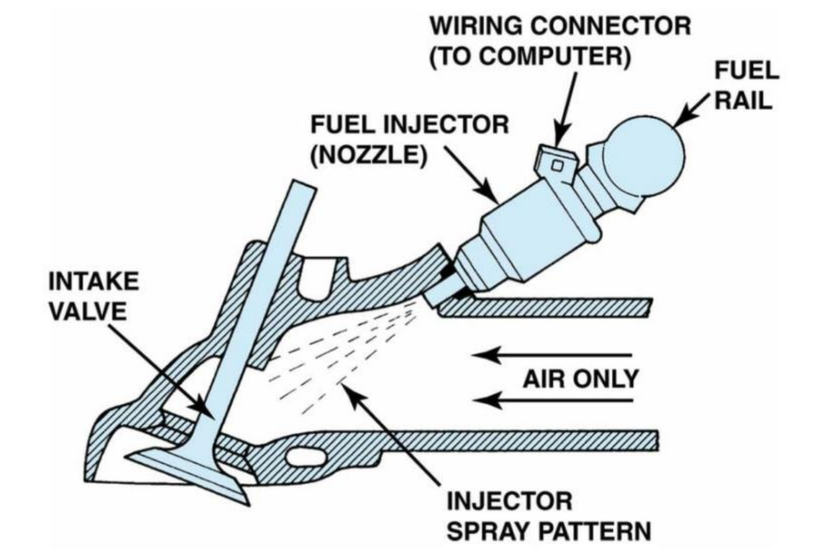

Figure 1-2 Multiport injection event [17]. Displaying fuel being injected into air during the intake stroke creating a homogenous air/fuel mixture

1.3.3 Direct Injection

Direct injection (DI) enables the ability to inject fuel directly into the combustion chamber, while avoiding further upstream wall wetting. Wall wetting is when fuel is injected in the chamber and some fuel is deposited on the chamber walls or piston face. This can cause carbon build up from incomplete combustion and decreases in efficiency. DI has shown to increase fuel economy and efficiencies while reducing emissions. DI injectors usually inject fuel into the combustion chamber at pressures of 70 – 350 bar (1,000 – 5000 psi) [18], [19].

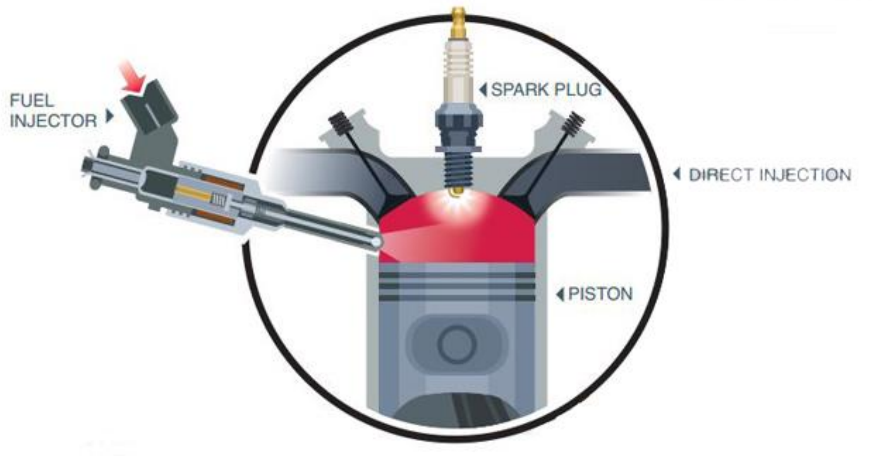

Figure 1-3 Direct injection event [20]. Fuel is directly injected into the combustion chamber during the compression stroke. Then once the piston is near top-dead-center the spark plug will ignite the mixture

DI has gained considerable traction in the industry due to its proven fuel efficiency benefits over conventional, port fuel injected engines by enabling down sized boosted engine platforms [8], [9]. Recent advancements in high-pressure gasoline direct injected (GDI) fueling systems have made DI more viable. While DI provides better efficiency and less emissions, carbon build up within the cylinder proves to be undesirable and producing more PM emissions than multiport fuel injection.

1.4 Fuels

In today's transportation sector there are two main fuels that are used in medium and heavy duty on-road applications: diesel and gasoline. Diesel and gasoline comprise of 89.4% and 9.8%, respectively, of fuel consumption within the market [5]. Natural gas and LPG are two alternative fossil-based fuels being explored. Given their ubiquitous abundancy throughout the world these fuels will help reduce GHG. Their unique properties of producing less emissions with a similar amount of energy produced, compared to that of diesel and gasoline, make these fuels a viable alternative [21]. Due to these fuels' clean burning properties, both have been increasingly popular within the electrical generation and transportation sectors. In addition to biomass derived fuels, hydrogen is also being considered as a potential alternative cleaner burning fuel. Hydrogen offers a higher energy density compared to gasoline; hence the same amount of power can be produced as a gasoline engine with less fuel. Furthermore, hydrogen produces less emissions than both gasoline and diesel.

1.4.1 Diesel

Diesel fuel consist of thousands of hydrocarbon compounds, namely, paraffins, olefins, aromatics, and naphthenes. Diesel when injected into a combustion chamber of high pressures and temperatures will auto ignite (compression ignition engines). Diesel has a higher energy density per volume compared to gasoline, with around 113% of the energy per 1 gallon of gasoline equivalent (GGE) [22]. While diesel has the ability to ignite and combust at higher pressures producing higher thermal efficiency, as mentioned earlier, diesel produces large amounts of NO_X and PM which is undesirable.

1.4.2 Gasoline

Gasoline also consists of hundreds of hydrocarbons such as paraffins, olefins, aromatics, and naphthenes. Gasoline is a petroleum byproduct, and to meet Renewable Fuel Standards program demanded by the United States Environmental Protection Agency, ethanol (10% by volume) is added to the mixture to reduce greenhouse gas emissions and oil imports from other countries

[23]. Gasoline has an energy density of around 46 MJ/kg, which is slightly more than diesel. Given, diesel has a higher density than gasoline, diesel has around 15% more energy per volume equivalent. While there are efforts to reduce emissions produced by gasoline engines, alternative fuels pose greater benefits.

1.4.3 <u>Liquified Petroleum Gas</u>

Liquefied petroleum gas (LPG) consists of approximately 90% propane, 5% propylene, and 5% of other trace gases such as butane and butylene based on a HD-5 standard within the United States [24]. LPG's octane ratings (RON 95-109.4 for varying global blends vs. 84-93 for gasoline) offer combustion advantages over many traditional fuels such as gasoline and also offer higher flame speeds than natural gas [22], [25]. LPG compared to compressed natural gas (CNG), is stored as a liquid at moderately low pressures, while retaining a significantly higher energy density (LPG: 350 psi, 27 MJ/L, CNG: 3,600 psi, 9MJ/L) [24]. Additionally, since LPG is stored as a liquid at lower pressures this allows for easier handling and transportation. LPG's higher hydrogen:carbon (H:C) ratio is significantly higher than gasoline and diesel, which in turn reduces GHG emissions at similar energy conversion efficiencies. LPG is a byproduct of natural gas and liquid petroleum refining and despite being the largest exporter, the United States maintains a substantial surplus of LPG. Currently, LPG engines are in production and conversion kits are available that operate using port injection or carbureted delivery system, and spark ignition systems. The industry is interested in utilizing direct injection strategies and LPG. However, due to LPG's tendency to flash boil due to its super-heat degree at engine relevant conditions, this poses additional challenges that must be overcome when considering an engine's design and will be discussed below.

1.4.3.1 __Challenges with LPG (Propane)__

While LPG has numerous benefits proving to be a potential alternative fuel, there are unique challenges that LPG poses. Propane is largely the main component of LPG and is considered to be a surrogate. Both propane and LPG have unique physical properties such as high vapor pressure, high volatility, and low viscosity that prove to be quite different than traditional fuels.

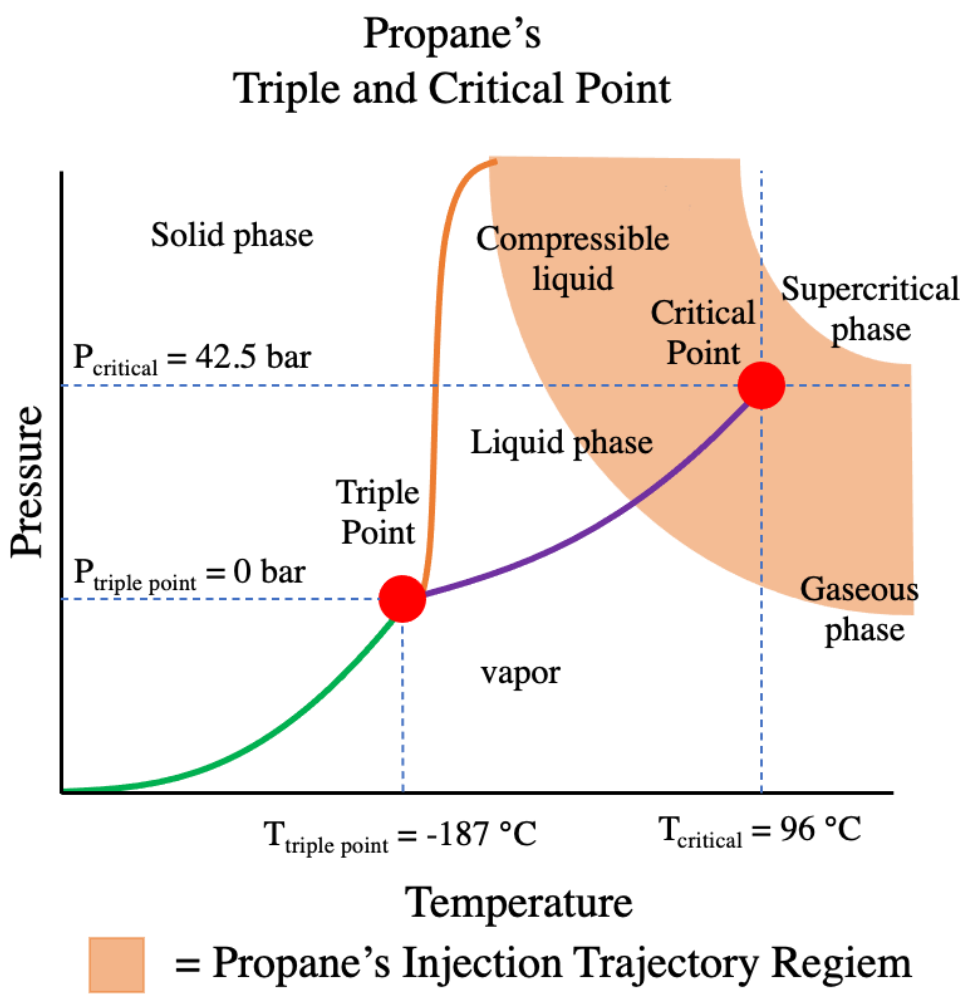

Figure 1-4 Propane's triple point and critical point plot. Displaying possible regimes where propane would exist at engine like conditions. Propane's vapor pressure is 9.25 bar,135 psi @25 °C

DI fuel injection events operate on the order of 100's of bar of pressure and temperatures ranging from -20 °C to 90 °C. When injected in the combustion chamber at potentially much higher pressures and temperatures, propane can fall into different phases that influence the spray morphology. Usually when propane is stored in a tank, it exists as a liquid given its vapor pressure (9.5 bar, 135 psi @ 25 °C) at higher pressures propane exists as either a compressible liquid or super critical fluid [26] as seen in Figure 1-4. Once injected into an engine, propane potentially falls into numerous regimes which can be liquid, compressible liquid, super critical fluid, or a vapor. At certain temperatures and pressures, propane will exhibit flash boiling or flare flashing effects that in turn influence the mixing of the fuel within a combustion chamber. Flash boiling occurs when there is a rapid depressurization of the liquid fuel which falls below that of the fuel's vapor pressure. When the pressure in the chamber is below the fuel's vaporization pressure, the liquid fuel almost instantaneously transitions into a vapor jet that greatly effects the dynamics of the spray. This unique physical phenomenon exhibited in propane proves to be a complicated dynamic that affects spray patterns exhibited in DI engines.

1.5 Direct Injection and Propane

To decrease emissions and increase efficiency, propane-fueling technologies and DI provide a clear path forward to achieving a cleaner heavy-duty engine. DI provides the ability to inject directly into the combustion chamber, which offers the capability to achieve a suitable fuel vapor distribution, a degree of homogenous stratification, and avoid wall wetting within the chamber. Utilizing both propane and DI, it is necessary to characterize the fuel vaporization and mixing of the fuel injection system in the combustion chamber and to inspect and characterize the combustion process. Propane's high volatility and low viscosity affects the vaporization and spray break up process within the combustion chamber [27]. Given propane's high volatility, the production of soot and PM are nearly eliminated due to a lack of formation of fuel films within the combustion cylinder. Previous studies have explored DI strategies using LPG and have shown significant improvements in both emissions and efficiencies. Splitter et al. utilized DI and LPG to achieve a significant reduction in soot and PM across all particle size ranges, as well as a 45% net thermal efficiency at stochiometric engine operation [28]. Additionally, propane's unique spray morphology formation has been well characterized over multiple engine-like conditions.

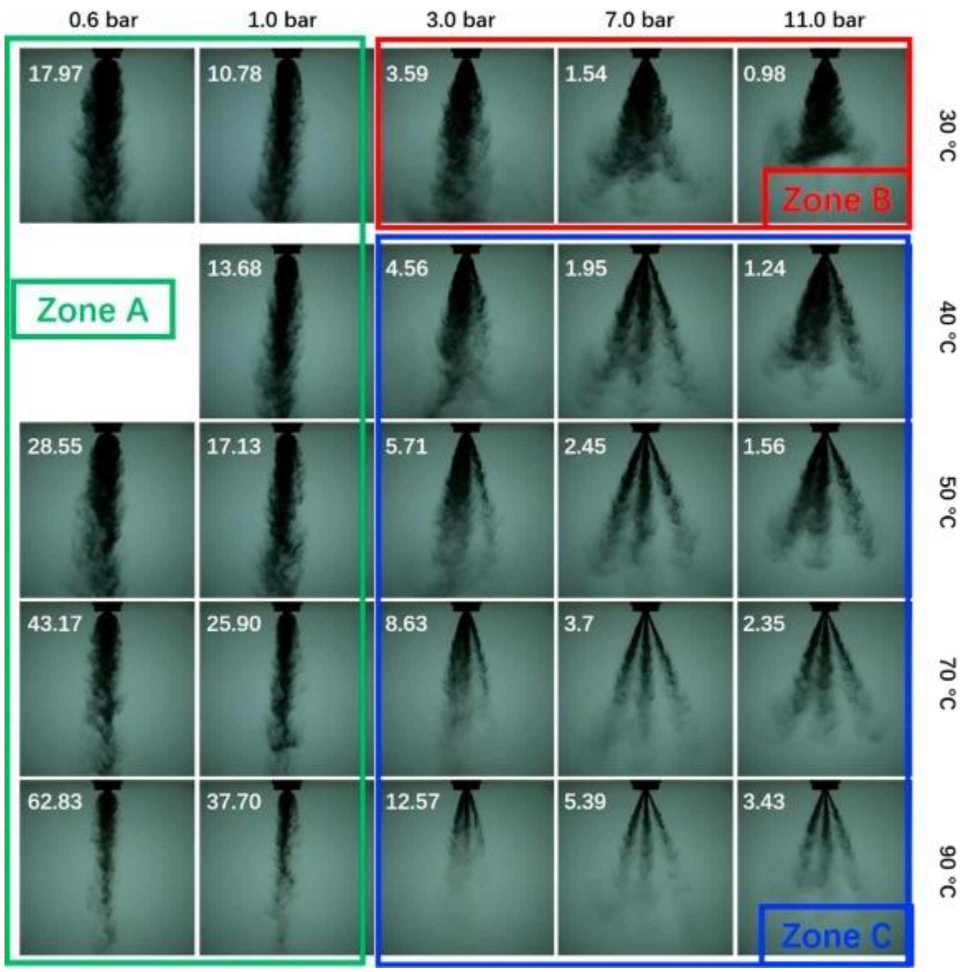

Figure 1-5 Propane sprays displayed using DBI, which present the unique spray morphology of propane at a wide range of engine operating conditions

Li et al. characterized multiple fuel sprays including propane utilizing diffuse background illumination (DBI), revealing that under certain conditions, propane exhibits liquid spray collapse caused by flash boiling when ambient pressure under 3.0 bar is experienced. As seen in Figure 1-5, propane can be categorized into three zones based off of morphological features. Zone A features a long narrow liquid jet, which becomes shorter as fuel temperature is increased. Zone B displays the transition of propane between non-superheated and superheated cases, which alter the spray morphology significantly. Finally, Zone C represents the increase in both ambient pressure and fuel temperature, displaying the transition from a somewhat collapsed liquid jet to individual shorter liquid jets that follow the inner structure of the injector [29].

To help understand the unique dynamics of flash boiling for propane spray, Lacey et al. found the conventional definition of flashing ratio (R_p) used with iso-octane, did not accurately capture the extreme spray collapse caused by flash boiling for propane. To accurately define the right threshold for propane, Lacey et al. introduces a new pressure ratio (R^*_p) that takes into account the static pressure at the choked throat of the nozzle and also the pressure in the chamber. This new pressure ratio indicated that if $R^*_p = 1$, the threshold is choked, while $R^*_p > 1$ denotes that the flow is under expanded. This pressure ratio gives a new more accurate definition of whether a fuel will undergo flashing conditions, as the pressure and temperature in the fuel rail are now accounted for as parameters which influence the spray dynamics. Additionally, in this study, Lacey et al. explains when propane has a $R^*_p > 1$ (under expanded), the individual jets expand significantly to the point where the jets grow so much in width, they begin to interact with the other jets, eventually resembling that of a single jet [30].

To assure that high thermal efficiencies and low production of soot, PM, and NO_X are met, there will likely be a need for the modification of injection hardware, combustion chamber, and piston designs. Different operation strategies (pulse duration, injection timing, number of injections, etc.) will also enable greater efficiencies. Hence, before LPG and DI can be implemented in heavy-duty engines more research is needed to characterize the mixing process in a combustion chamber.

1.6 Modeling Techniques

The implementation of accurate injection requires numerical models which have become a pivotal design and optimization tool for DI fueled engines. To accurately represent the spray morphology within an engine-sized domain, multiple modeling approaches are needed. Lagrangian spray modeling is a technique that avoids detailed solutions of a liquid-gas interface by treating sprays as a cloud of discrete parcels that are tracked by their trajectory and coupled with the gas phase [31]. Lagrangian spray modeling has been extensively used in the field of energy applications, atmospheric meteorology, and many more [32]. In previous studies, Bracco et al. explored experimental and numerical diesel spray injection measurements using a Lagrangian approach to track penetration lengths and breakup regimes [33]. While the numerical simulations followed a general trend similar to the experimental results, this method proved to be a helpful comparison tool but not a prediction tool. Although, Lagrangian spray simulations over the past few decades have greatly improved their accuracy for liquid dominant cases. This approach considers the spray as an incompressible fluid which lacks accuracy in the representation of an under-expanded jet such as propane at engine-like conditions [30], [34].

To help further enhance the accuracy of both the liquid and gaseous regimes of the spray, a Lagrangian-Eulerian (LE) approach is taken. As stated earlier, Lagrangian spray modeling provides information regarding distinct spray parcels. Eulerian modeling helps provide information regarding more dense regions of the spray and is helpful to capture the entirety of the spray morphology.

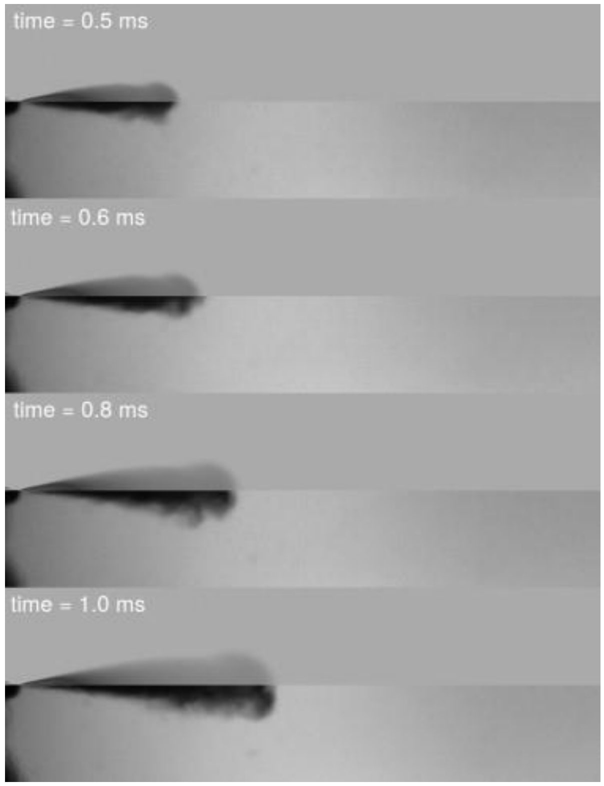

Figure 1-6 Representation of diesel spray injections results over a multiple time stamps. Displaying Eulerian modeling (top half of each time stamp) and experimental (bottom half of each time stamp) (Payri et al.) concluding a good agreement between results [35],[36].

For example, Salvador et al. utilized a Eulerian modeling approach to capture high pressure diesel spray penetration lengths and angles. Salvador et al. concluded that there is a good indication for spray penetration lengths (Figure 1-6) with errors less than 5%. However, numerical spray angle predictions were larger than experimental [36]. Although Eulerian modeling provides detailed information regarding the overall denser regions of the spray morphology, combining both Lagrangin and Eulerian modeling approaches provides a better understanding of the entire spray morphology and utilizes the advantages from both approaches.

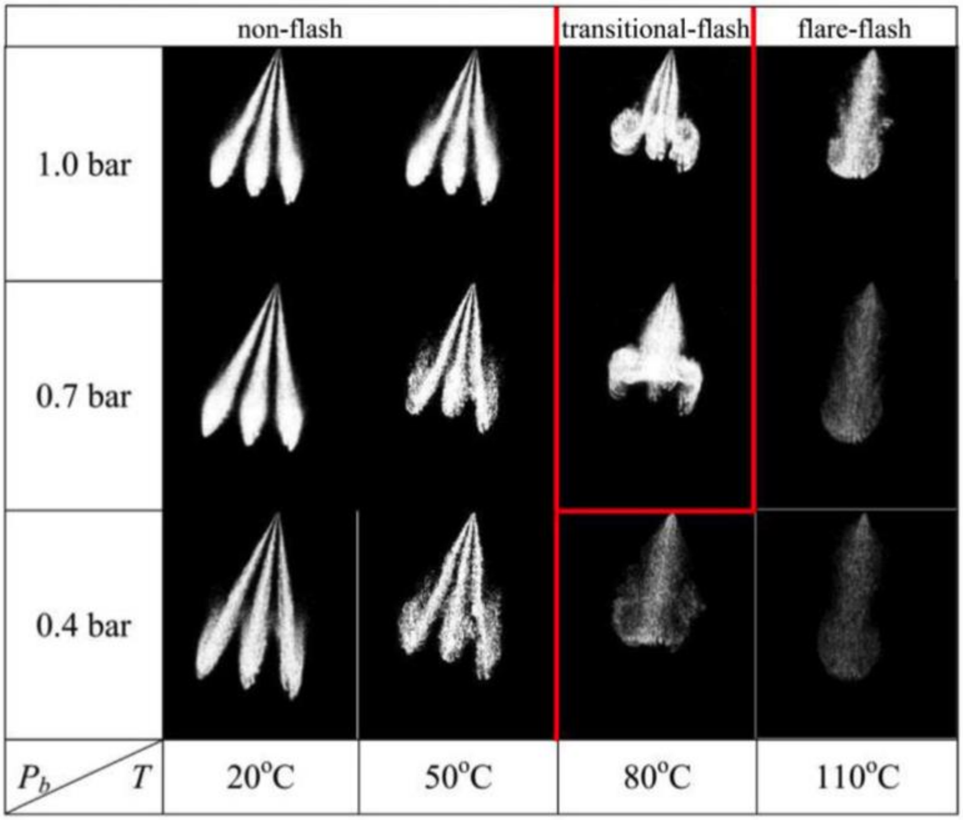

Figure 1-7 Simulated results for n-hexane utilizing a Lagrangian-Eulerian approach to model the transition between non-flare flashing conditions and flare-flashing conditions. Concluding a good agreement with experimental results [37]

Shen et al. utilized a Lagrangian-Eulerian approach to resolve two-phase flow spray dynamics of directly injected n-hexane. As shown in Figure 1-7, Shen et al. displays simulated spray morphology structures of n-hexane over a range of engine operating conditions. When the simulations are compared to the experimental results there is a good agreement between the spray morphology. The simulations are able to capture the individual plume development as well as the transitional flashing regime, capturing strong plume-to-plume interactions. While n-hexane has a similar volatility and viscosity to gasoline, propane's extreme flashing effect, with higher volatility and lower viscosity, proves to be a greater spray morphology challange [37].

Additionally, studies have conducted modeling campaigns for propane using Eulerian-Eulerian approaches, which have proven accuracy in modeling propane's spray morphology. As seen in Figure 1-8, Rachakonda et al. displays non-condensing gas mass fractions and liquid-gas interface density areas of propane. This study and others have also modeled propane, but further investigation is needed to truly map out all conditions and feature of propane's spray morphology [38].

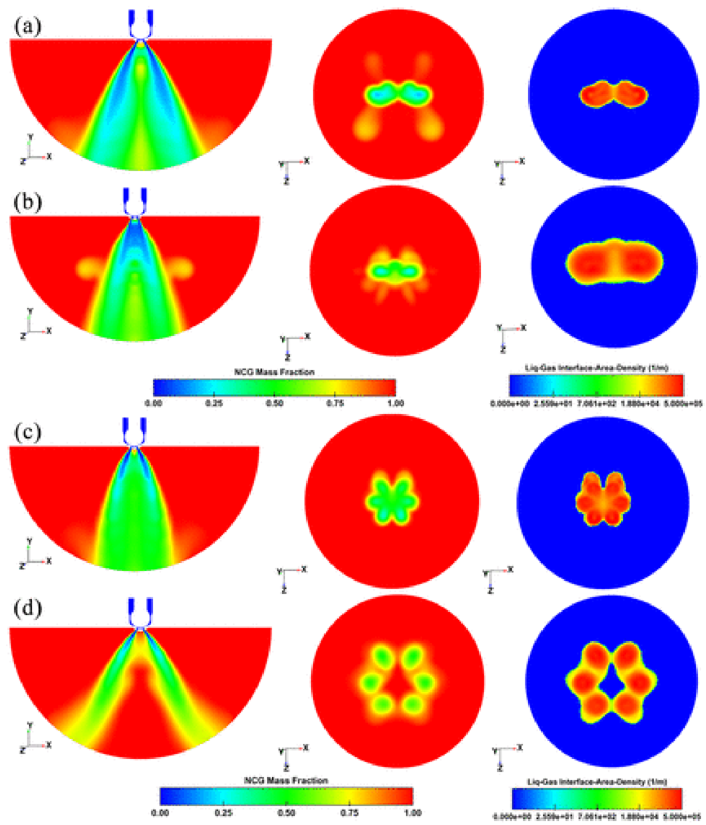

Figure 1-8 Propane's non-condensing gas mass fraction side view (left column), non-condensing gas mass fraction cross section, oriented facing up (center column), and liquid-gas interface area density oriented facing up [38]

The end goal of the spray modeling development for engine applications is to predict the liquid phase penetration and the fuel entrainment in the combustion chamber. These features are relevant to capture the performance and the emission propensity of the engine operation and are usually based on preliminary correlation studies in a constant volume and inert environment. Experimental testing campaigns are a key element to validating spray modeling to ensure accurate representation. Given propane's unique physical characteristics, producing accurate spray models would be extremely difficult without the guidance of experimental results.

1.7 Experimental Imaging of LPG Sprays

Researchers have investigated the behavior of gasoline, diesel, and a variety of surrogates and alcohol fuels using Schlieren and Mie scattering imaging techniques. These researchers have visualized spray morphology and species/phase distributions during cold injection and combustion events [33], [39]–[44]. However, only a limited number of validated spray models [45]–[47] and experimental data [27], [48] are available regarding the spray dynamics of LPG at engine-relevant conditions.

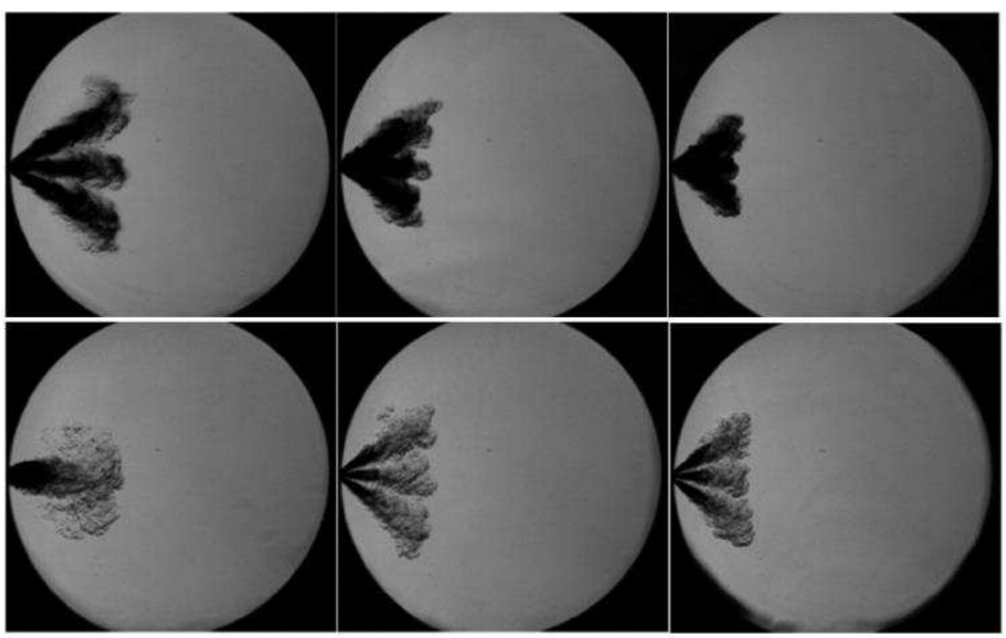

Figure 1-9 Schlieren imaging for iso-octane (top) and propane (bottom) [27]

Schlieren imaging is a well-established, line-of-sight technique that is commonly used to visualize variations in the refractive index of a transparent medium, created by gradients in the corresponding density field, providing information that would be unseen by the naked eye. This technique is commonly used in literature for both qualitative visualization and quantitative fuel spray measurements, such as vapor phase penetration [27], [30], [44], [49]. As seen in Figure 1-9, Lacey et al. displays both iso-octane and propane sprays at multiple engine operating conditions utilizing Schlieren imaging. Here, Schlieren is able to capture the overall global morphology of the spray, while recording the transition between non-flashing and flare flashing sprays.

Additionally, to Schlieren, Lacey et al. also uses Mie scattering imaging which is an elastic light scattering technique used extensively in prior literature to measure liquid penetration through a medium. When a spray is exposed to a specific wavelength of light, the liquid region scatters light in all directions, but vapor regions do not illuminate. Hence, Mie scattering imaging is often used to capture the liquid regions of the spray [30], [50]–[52]. When Mie scattering is combined with Schlieren imaging, a strong contrast between liquid, high density vapor, and low-density vapor regions can be distinguished. Like Schlieren, Mie scattering captures the liquid regions of the spray globally, i.e., no clear distinction between each plume can be observed. Lacey et al. uses Mie scattering to capture liquid penetration lengths and speeds. While this data provides valuable information regarding the overall liquid spray behaviors, it is difficult to extract plume specific information, which is critical for spray model validation. Furthermore, Lacey et al. also utilizes planar Mie scattering in another study, which employs a sheet of laser light, that captures a finer resolution of liquid penetration and entrainment within an engine. The liquid region of the spray as seen in Figure 1-10, is within an optically accessible quartz cylinder window within an engine. With the use of planar Mie scattering, Lacey et al. was able to capture liquid propane injected into a cylinder and capture extreme flash boiling effects presented at engine operating conditions [50].

Similar to this previous work, this project seeks to develop an experimental setup for visualization of LPG sprays. A planar laser Mie scattering imaging technique was utilized to map out the liquid regions for an individual plume. Utilizing this data will assist to develop, validate, and tune numerical LPG spray models for use in full cycle engine simulations.

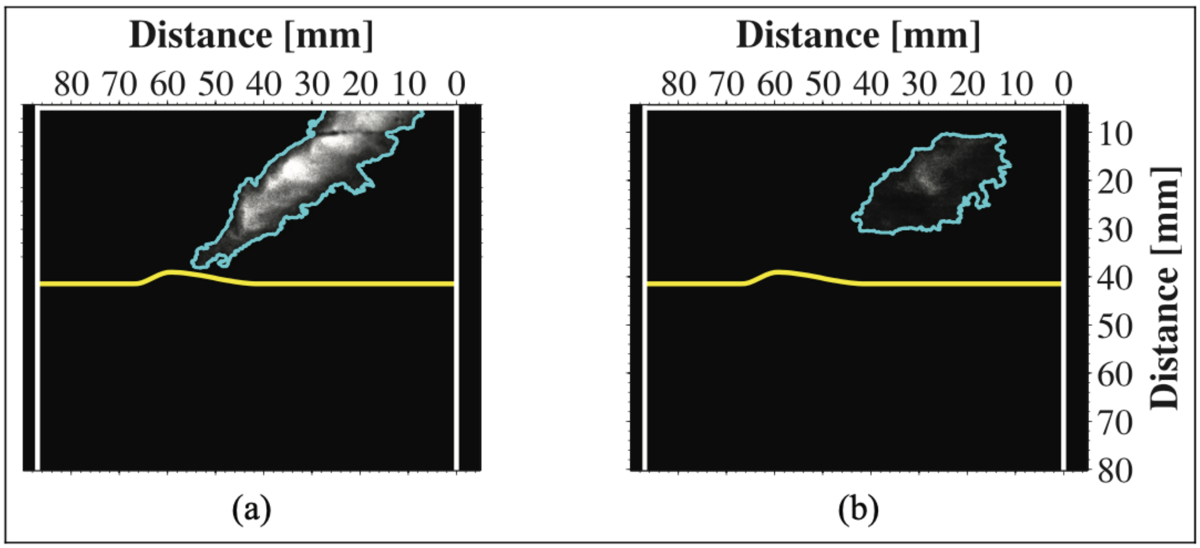

Figure 1-10 Propane spray imaged using planar Mie scattering technique to capture liquid penetration within an optically accessible engine cylinder. Image of liquid-phase propane with (a) P_{inj} = 4.5 MPa and (b) P_{inj} = 7 MPa

Chapter 2 – Experimental Methods

2.1 Introduction

To capture the spray morphology, and reduce in-cylinder flows and heat transfer effects, an alternative test facility such as a constant volume chamber (CVC) test facility was deployed. The simple operation and convenient optical access of this facility makes it attractive for controlled investigations that can be used to validate physics-based models and provide important insight into spray processes. The high-pressure spray chamber (HPSC) provides a fixed volume of trapped gas, which can be inert and quasi-quiescent, allowing for the study of spray morphology free of complex in-cylinder turbulence and combustion. This chapter entails the design, modification, and recommission of an existing CVC. Additionally, the usage of high-speed Schlieren and planar Mie scattering imaging techniques, post processing, and the numerical simulation methodology and setup will be discussed.

2.2 Design and Updating

The HPSC was initially used to study micro-pilot injections for diesel-like engine conditions previously capable of reaching temperatures up to 745 K and pressures of 70 bar. As seen in Figure 2-1, the HPSC is a 300 mm by 300 mm by 100 mm piece of 304 stainless steel. Since the previous study utilized such high pressures and temperatures that a rarely seen during injection events of a direct injection spark ignited (DISI) engine, multiple alterations were needed to adapt the HPSC to expected temperatures and pressures for this study. Additionally, existing seals and heating apparatus’s were no longer available, a new design was needed to recommission the HPSC for desirable conditions. The design and updating section of this thesis will be divided into four sections addressing the main body, connections and flanges, HPSC heating, and finally HPSC pressurization.

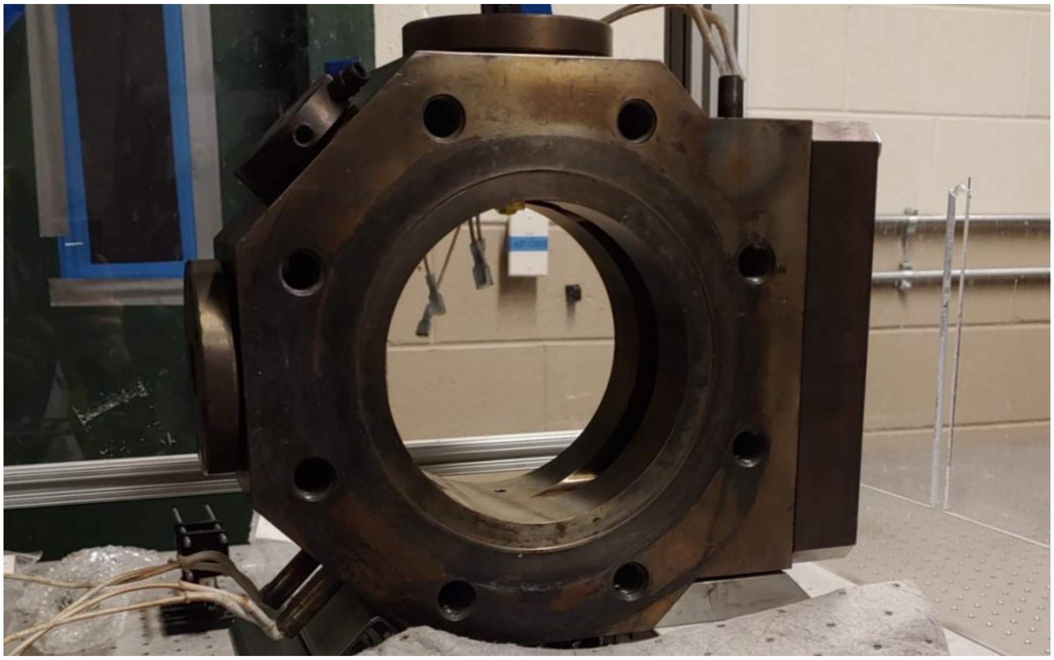

Figure 2-1 The high-pressure spray chamber main body with previous studies flanges. This also displays the bolting arrangement for each round window that is attached on either side

2.2.1 Main Body

The main body of the high-pressure spray chamber is the heart of the system and provides an interface for adapters and optical windows. The main body is designed with the idea of reconfiguration in mind, and with 3 large ports, and the ability to incorporate new instrumentation into the body. In the case of this study, a newly designed and manufactured thermocouple flange and injector adapter flange were designed and manufactured. The internal volume of the chamber is 1.85 liters and provides a large enough volume and dimensions (100 mm wide by 150 mm diameter) to be comparable to the physical size of a heavy-duty engine’s combustion chamber and to avoid unwanted effects such as wall-wetting. The main body also incorporates heating cartridge holes that help maintain desirable temperatures within the chamber, this will be elaborated more in-depth in the HPSC heating section. One of the most desirable features of the HPSC are the optical access that provide the ability to use multiple diagnostic imaging techniques to study spray phenomenon.

2.2.1.1 HPSC Optical Access

The HPSC's three-way optical access provides adequate visualization for imaging spray morphology. This configuration allows for both line-of-sight and orthogonal visualization of the fuel spray.

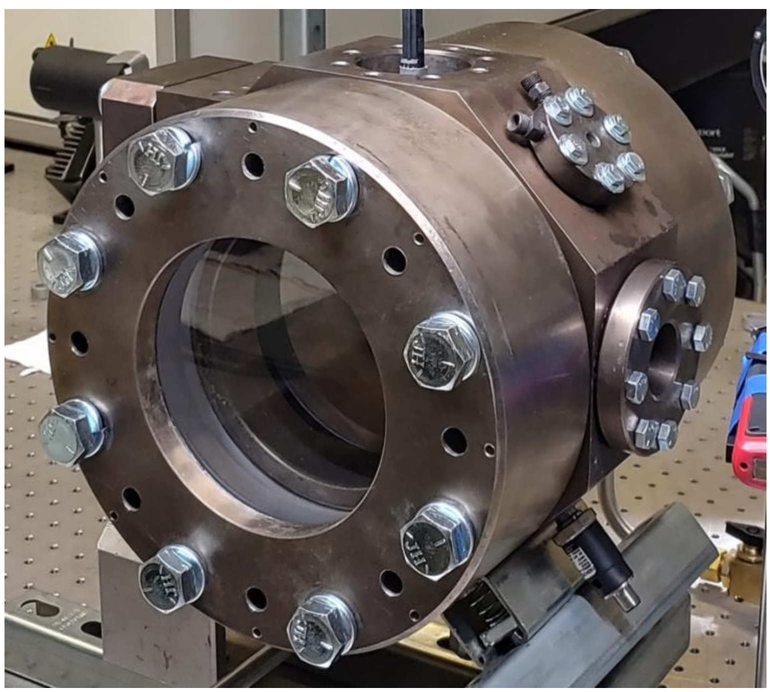

Figure 2-2 The high-pressure spray chamber with fused quartz silica windows on both sides as well as on the front side of the chamber as seen at the top left of the photo. Also, displaying bolting arrangement with all windows and flanges adapted to the chamber

As seen in Figure 2-2, on both sides of the chamber, fused quartz silica windows are used as the optical access to image a spray. These windows are 100 mm wide by 150 mm diameter and are held on to the chamber with additional 125 mm by 300 mm diameter 304 stainless steel hold-downs. These hold-downs are held to the chamber with eight Grade 8 bolts to provide an even and distributive clamping force.

When these windows were acquired, scratches, pitting, and ablation were evident problems that arose when viewing sprays through Schlieren imaging techniques. Different options were assessed to either polish the windows in-house, send the windows to an external polishing company, or to purchase new windows. It was determined that polishing the windows in house was the most cost and time effective option. Fused quartz silica is an extremely hard material where normal silicon carbide sandpaper would not last and most likely would damage the windows. Instead, polycrystalline diamond sanding fluid and mats of different grades were used to sand and polish the windows to a desirable clarity.

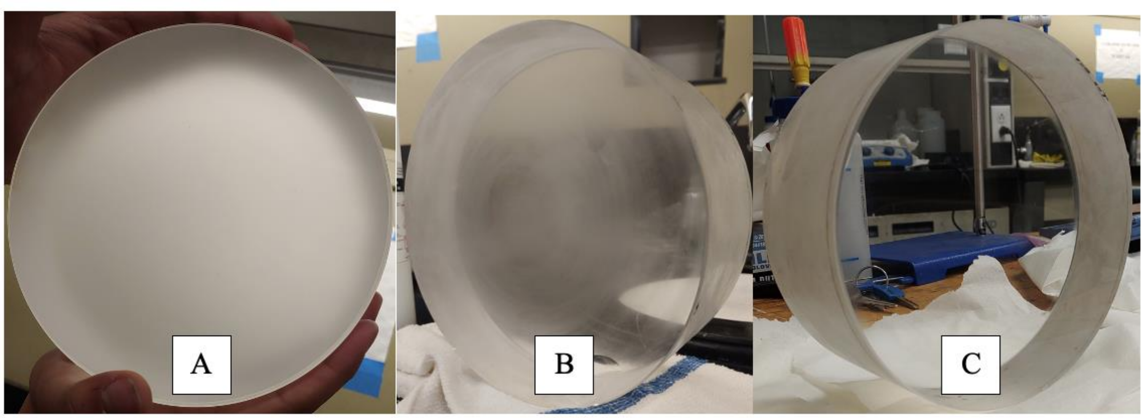

Figure 2-3 Progression of sanding and polishing stages of windows (A) after metal woven mesh mat, (B) after 1 µm DIAMAT (polycrystalline diamond sanding fluid) sanding, (C) after silicon polishing

A 200 mm lapping wheel along with a coarse metal woven mat, 20 µm, 15 µm, 6 µm, 3 µm, 1 µm diamond suspension fluids, and 0.02 µm silica polishing fluid were used with an array of diamond fluid suspension mats to produce a final acceptable clarity. Figure 2-3 gives a brief overview of the progression of quality of the windows as finer and finer sanding is used. Once sanding and polishing was finished, a significant improvement in the quality of Schlieren imaging was seen.

In addition, a third window was mounted perpendicular, on a side of the chamber. This fused quartz silica window is a rectangular prism of dimensions 38 mm by 25 mm by 170 mm and provides optical access for a laser sheet that is used as a light source for planar Mie scattering imaging. The rectangular window is also similarly attached to the chambers main body by a 304 stainless steel hold-down. This window was purchased from Advanced Glass Industries.

2.2.2 Connections and Flanges

The HPSC has multiple connections and adapters that make the chamber operational and measurable for imaging techniques. Previously designed ports allowed for easy access for temperature and pressure measurements. There are also two ports (inlet and exhaust) at the bottom of the chamber that allow for pressurization and depressurization of the chamber.

Additional ports on the top and side of the chamber allow for easy integration of adapters into the main body of the chamber. A flange was designed and manufactured from aluminum, which incorporated a modular design, capable of adapting multiple GDI fuel injectors. This flange composed of three separate parts to secure the injector to the chamber. Additionally, this flange incorporated a water jacket to regulate and maintain the fuel temperature in the injector. This injector flange was manufacture by Colorado State University's Rapid Prototyping Laboratory (RPL) at the Powerhouse Energy Institute. An additional flange was manufactured to incorporate direct access for a thermocouple to be placed millimeters away from the tip of the injector. This thermocouple measured ambient temperatures within the chamber. Figure 2-4 shows both the injector flange and the thermocouple flange that were adapted to the chamber.

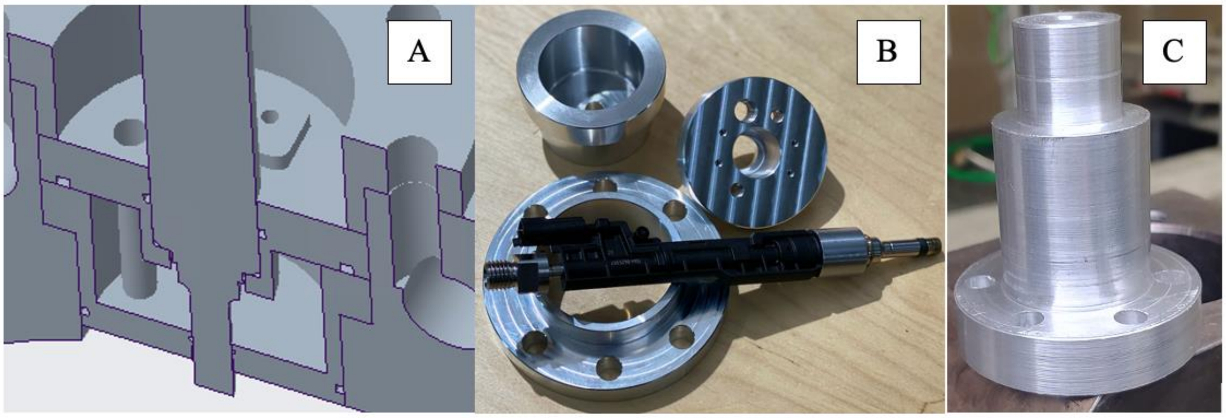

Figure 2-4 Images of flanges incorporated into the HPSC (A) PTC-Creo solid model of injector flange assembly displaying dummy injector and water jacket flange used to maintain fuel temperature, (B) manufactured flange assembly manufacture by Rapid Prototyping Lab at CSU, and (C) manufactured thermocouple flange which allows for the placement of a thermocouple near the injector tip

2.2.3 HPSC Heating

The HPSC is capable of reaching temperature up to 393 K by utilizing ten, 150 W heating cartridges placed strategically around the chamber and two 750 W tape heaters, one wrapped around each window hold-down. With the help of both heating cartridges and tape heaters the chamber is able to reach temperatures of 373 K within a few hours. Initially, the chamber used the two tape heaters and a 750 W inline duct heater to heat compressed nitrogen gas, and or air entering the chamber. It was eventually discovered that using the inline heater marginally improved the rate at which the chamber was heated. Additionally, the tape and cartridge heaters increased the temperature of the chamber walls while subsequently heating the internal ambient air. Earlier in the project, ceramic fiber insulation mats were used to accelerate the heating process. Eventually, these mats were discarded as they provided little benefit and were very cumbersome.

2.2.4 HPSC Pressurization

The HPSC for this study, is capable of reaching pressures up to 16 bar, using compressed nitrogen gas. As stated earlier there is an inlet and exhaust port that provide the regulation of pressure that is needed. Figure 2-5 demonstrates the piping and instrumentation diagram (PID) that depicts the general piping setup to pressurize the chamber.

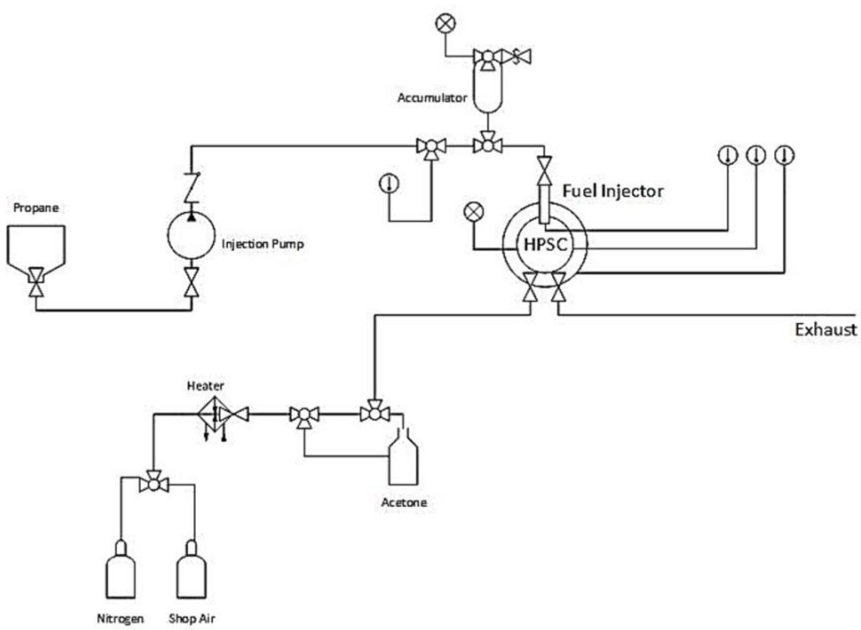

Figure 2-5 PID of the HPSC, with thermocouple and pressure transducer attachments. Additionally, the fuel injections system utilizes a propane tank, where liquid propane is drawn into a syringe pump and then pressurized into the fuel injection system. Also, the HPSC pressurization system as seen utilized shop air and nitrogen

To regulate the pressure within the chamber a series of valves, pressure regulators, and pressure transducers were utilized. A combination of O-rings and gaskets were used on all flanges and window interfaces to seal the chamber. Gaskets were used to both provide a soft interface for the windows and to seal the chamber.

A challenge that was encountered while sealing the chamber, was the interface between the injector tip and the injector flange assembly. Initially, the flange and injector were designed to incorporate an O-ring, that would provide an airtight seal while also having the capability to be removed. This proved to be a difficult task given that such tight tolerances were needed, and the O-ring and injector tip would not fit through together. To combat this issue, a quick setting rubber epoxy was used. This epoxy was applied to the base of the injector flange and on the sides of the injector tip. Once cured, this epoxy provided an airtight seal that could be easily removed and reapplied.

2.3 <u>Fuel Injection System</u>

As shown in Figure 2-5, the fuel injection system can be seen integrated in to the overall HPSC system. The fuel injection system provides relevant engine injection pressures typically seen in GDI events. The fuel injections system is pressurized with an ISCO 350D high-pressure syringe pump, providing pressures up to 350 bar. With pressures reaching up to 350 bar, the fuel injection system was designed with a safety factor of 2, and subsequent parts were chosen appropriately. To provide an adequate amount of liquid fuel to the injector, an accumulator was designed and manufactured to hold 10 mL of fuel so the injector would not run dry. To fill the accumulator before operation would occur, a conventional propane tank would be placed upside down to allow for liquid propane to sit at the exit port of the tank. The tank would then be adapted to Swage-Lok tubing that would then be fitted to the syringe pump. The syringe pump would draw in liquid propane at a slow enough rate to where the vapor pressure would never decrease to a point were gaseous propane would enter the syringe pump. Once an adequate amount of fuel was extracted, the syringe pump would then fill and pressurize the accumulator to the desired pressure.

2.3.1 Fuel Injection

The fuel injector flange manufactured by RPL was designed to interface with most commercial fuel injectors. This provided the convenience of not needing to manufacture a new flange for each injector tested. This flange also incorporated a water jacket around the injector to provide either cooling or heating of the fuel within the injector. To control and maintain the temperature of the injector, a modified circulating pump, a 1 kW heater, a temperature controller, and a thermally insulated bath of glycol were used. Although the injector flange was adaptable to each injector geometry, an additional adapter was needed to connect each injector to the fueling system to be pressurized correctly and safely. These adapters as seen in Figure 2-9, required an additional supporting hold-down mechanism as the Spray-G and Delphi injectors utilize a press fit fuel adapter. This hold-down mechanism seen in Figure-2-6, provides a clamping force to the adapter which secured the adapter to the injector. The hold-down mechanism utilized all-thread rods, nuts, a waterjet cut hold-down plate, and machined fuel adapter.

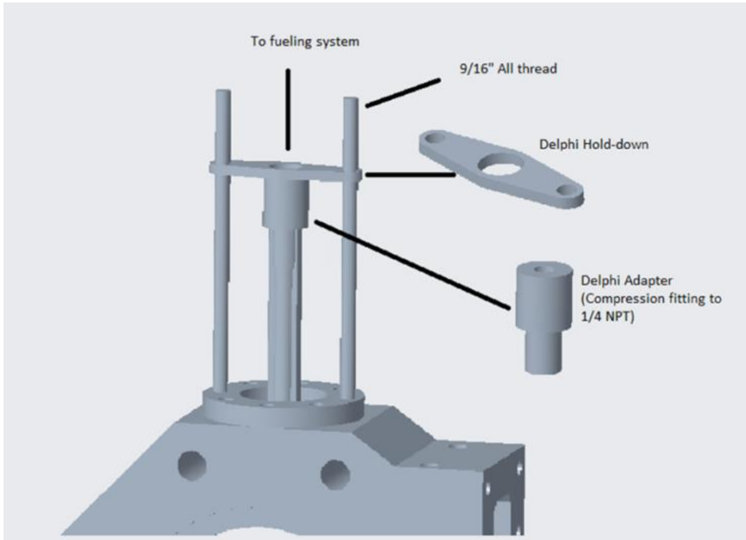

Figure 2-6 Hold-down clamping mechanism used to secure fuel system adapter to corresponding GDI injector. A combination of all-thread, waterjet plate, and adapter are used to ensure a high-pressure seal is created

2.3.1.1 __Spray-G Injector__

The Spray G fuel injector is an experimental, Delphi manufactured, axisymmetric, 8-hole, solenoid driven, GDI fuel injector. The Spray-G AV67–012 DI fuel injector provided by the Engine Combustion Network (ECN) has been used extensively in prior literature and has been well characterized [45], [53]–[55] and hence will be used to validate the HPSC as an adequate test facility. The nominal geometry of the Spray-G injector tip provided by ECN is shown in Figure 2-7.

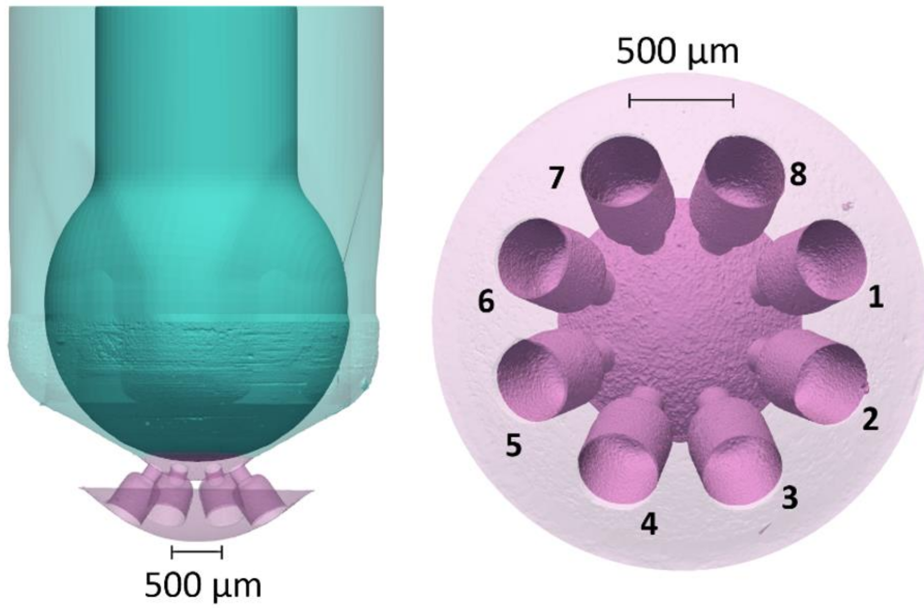

Figure 2-7 General depiction of internal geometry for Spray-G 8-hole, solenoid driven injector with scale

The Spray G fuel injector is capable of reaching injection pressures up to 250 bar. The Spray-G injector also requires a press fit adapter to mate and seal to the fuel injection system correctly. Both the injector and adapter can be seen in Figure 2-9.

2.3.1.2 __Delphi Injector__

The Delphi injector is a seven-hole, axisymmetric, 5° nozzle offset, solenoid driven, GDI fuel injector, manufactured by Delphi capable of reaching pressures up to 300 bar. This injector was chosen as the studies main stock injector of choice due to its larger mass flow rate, and high-pressure capability. An external company, CZero, was tasked with providing detailed information regarding the mass flow rate and nozzle geometry, given that there is no public information for the Delphi injector. While the geometry was measured, experimental testing and numerical modeling revealed discrepancies, and were traced back to the measurements of the geometry. The geometry of the Delphi injector is depicted in Figure 2-8.

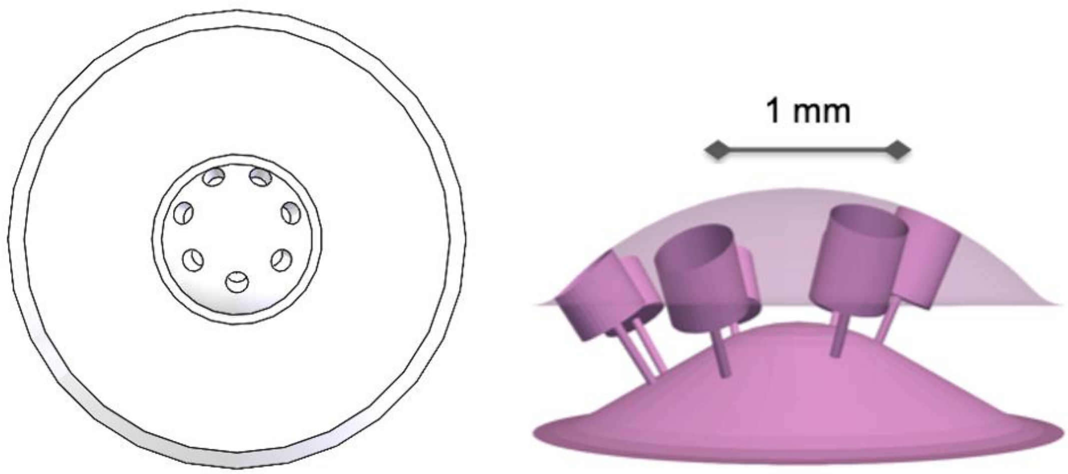

Figure 2-8 General depiction of external Delphi 7-hole injector geometry (left) and internal geometry with relative scale provided by Argonne National Labratory

The Delphi injector requires a press fit adapter to mate with the fueling system correctly. An aluminum adapter for the Delphi injector was designed and manufactured in-house. To make sure the injector and adapter would seal correctly and be able to withstand high pressures seen during injection, extremely tight tolerances of ± 0.001 inches needed to be held. As seen in Figure 2-9, both the Delphi injector and its' adapter are displayed.

GDI Injector	Injector	Connection/Fitting	Adapter
Spray-G			
Delphi			

Figure 2-9 Matrix of Delphi and Spray-G GDI injectors displaying connection points on the injector where a manufactured injector adaptor would ensure a high-pressure sealing surface with the fuel injection system

2.4 HPSC Controls and Instrumentation

To monitor the temperature and pressures of both the HPSC and fuel injection systems a virtual interface was created with LabVIEW. This interface is capable of reading both fuel and chamber temperatures and pressures. The LabVIEW virtual interface proved to be suitable as temperatures and pressures would change quickly depending on targeted conditions.

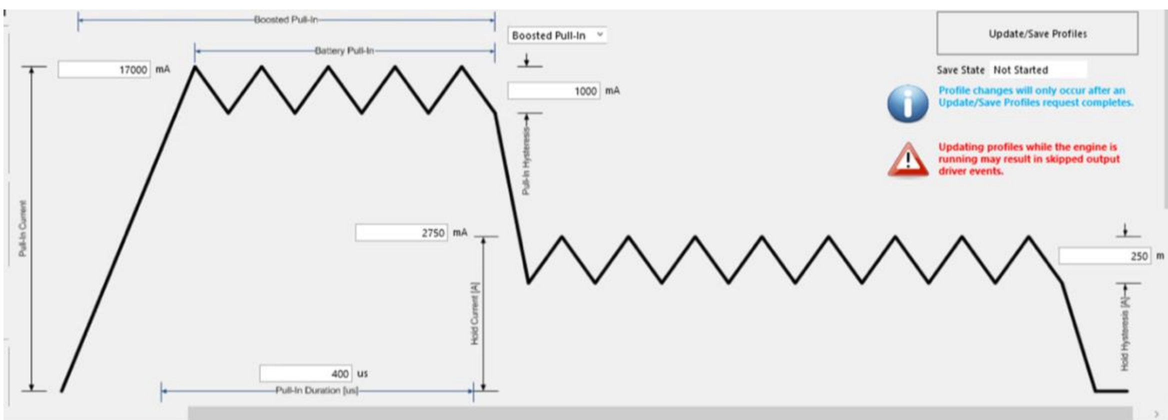

Figure 2-10 User interface on LECM to program injector current profiles for a certain injector. Displaying pull-in current and duration as well as boosted pull-in current

Each injector requires a specific injector profile which provides the correct voltage and current to the solenoid, which can raise and lower the internal needle. Most injectors are current driven electronics, requiring a specific current to operate consistently and reliably. To control the injection profile and duration, a Woodward large engine control module (LECM) was utilized. This control module is capable of single injections or creating a "pseudo" RPM, where the injector would be activated once per revolution as desired by the user. This feature was extremely useful for running the injector quickly and simultaneously with the Nd:YAG laser.

Figure 2-10 displays the user interface where the user can input the required current and duration for the injector.

2.5 <u>Optical Measurments</u>

A set of parameters such as vapor and liquid penetration lengths, widths, and speeds were chosen to map out the spray morphology and provide a qualitative and quantitative comparison to numerical models. To measure these set of parameters at engine-like conditions, Schlieren and planar Mie scattering optical diagnostic imaging techniques were utilized.

2.5.1 Schlieren Imaging

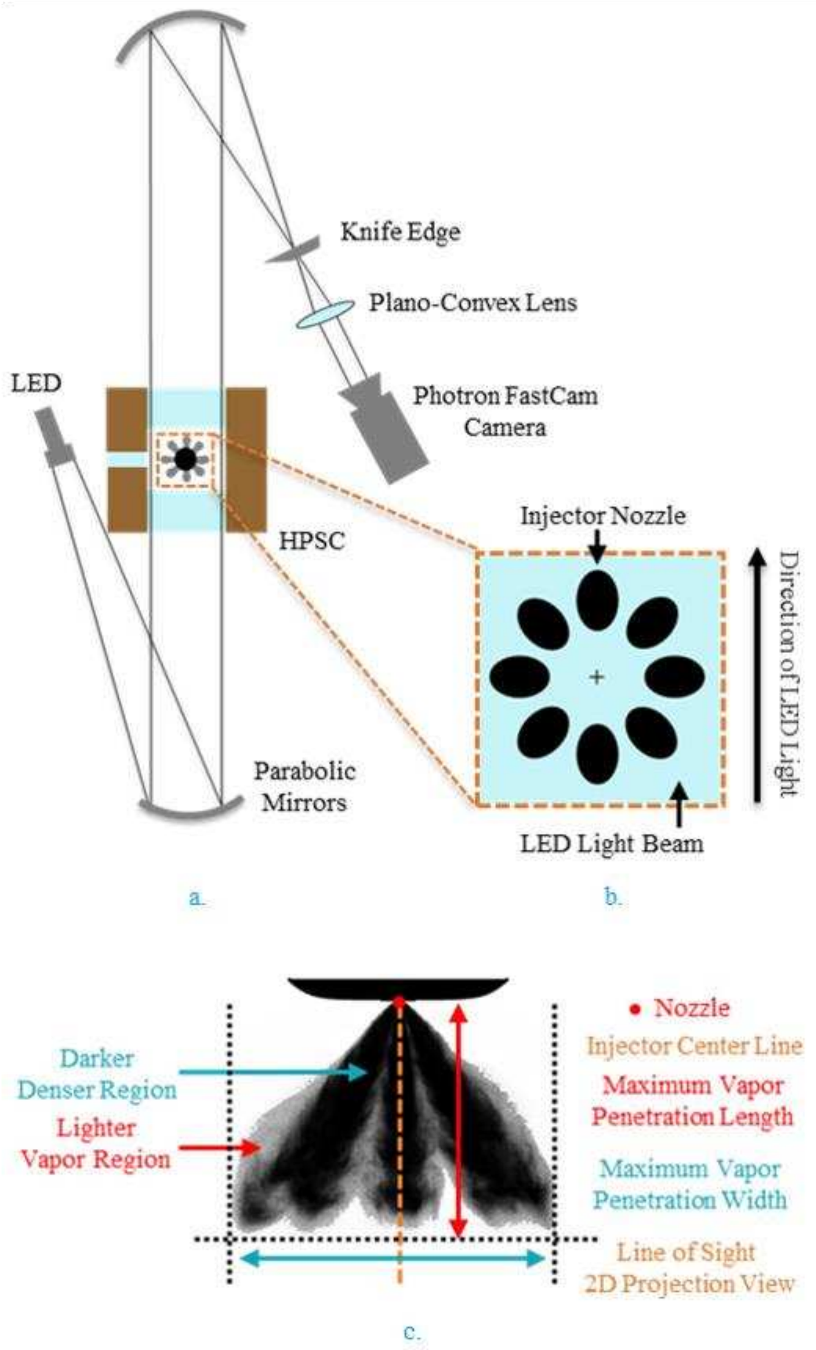

Figure 2-11 (a) Top-View schematic of Schlieren imaging setup, (b) nozzle-alignment relative to the LED light for Spray-G injector, and (c) resulting Schlieren spray image, features, and nomenclature.

2.5.2 Schlieren Imaging Set-up

Figure 2-11a demonstrates a schematic of the high-speed Schlieren setup used to visualize fuel injection events. A continuous, 200-lumen white LED was collimated through the HPSC by a 150 mm parabolic mirror of 750 mm focal length and received by an identical parabolic mirror placed in a z-type configuration. 3-D printing was considered as a fast and reliable solution to mount the parabolic mirrors for Schlieren imaging. The 3-D adapter provided a secure press fit of the mirrors. To add additional support security tabs, seen in Figure 2-12, were also printed. The 3-D printed mounts and tabs can be seen in Figure 2-12, mounted on an optical stand.

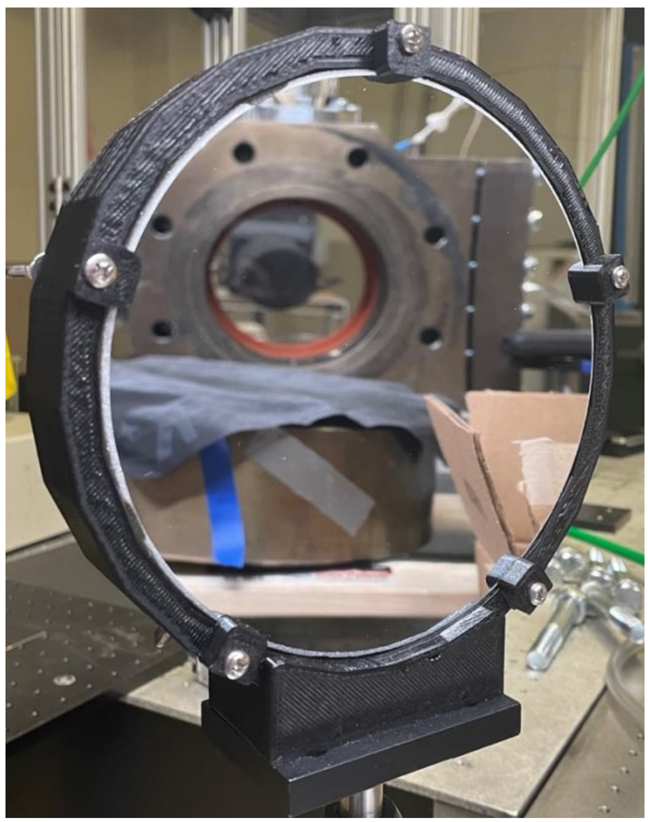

Figure 2-12 3-D printed mounting adapter and security tabs used to hold parabolic mirrors and adapt to laser stands and posts. These 3-D printed mounts provided fine tuning adjustments of height and angle, ensuring a correctly positioned parabolic mirror for Schlieren imaging

A knife-edge was used as the Schlieren cut-off at the focal point of the converging mirror to amplify the contrast and intensity variations. The images were finally sized with a 50 mm plano-convex achromatic lens of 150 mm focal length and acquired using a Zeiss Milvus 2/100M lens and Photron FASTCAM SA5 high-speed camera. The frame rate of the imaging was set to 30,000 frames per second (33 µs between frames) and provided images free of undesired flow features, such as dynamic pressure waves and temperature gradients. The high-speed Schlieren images, had a spatial image resolution of 298 µm/px capturing 376 x 640 pixel image. These Schlieren images were recorded for a range of chamber and fuel conditions of the spray to study the axial vapor penetration length, width, and penetration rate.

2.5.3 Schlieren Imaging Timing

With the use of a current probe and LECM, the injector current profile was measured using an oscilloscope. The Delphi injector profile, seen in Figure 2-13, was directly measured using the current probe attached to the Delphi stock injector electrical leads.

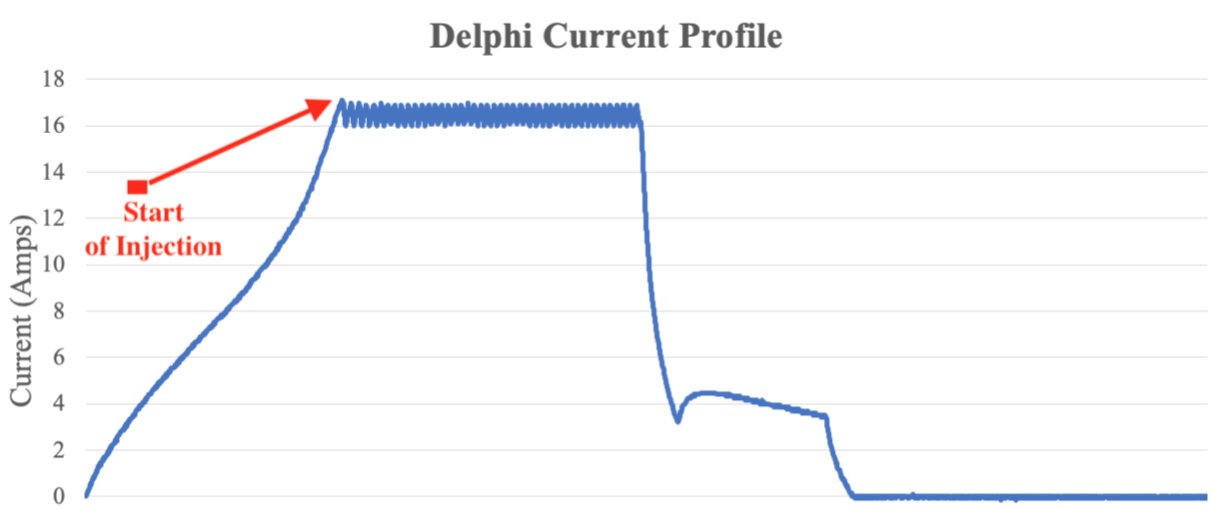

Figure 2-13 Delphi current profile over 1400 µs duration measured using an oscilloscope and also displaying the of start of injection

To synchronize the injector and camera, the start of injection needed to be found. As seen in Figure 2-13, the start of injection was found to be at the peak of the rise of the current profile. This signal then triggered the DDG, which had a correct delay. This delay provided an appropriate amount of time to trigger the Photron camera and capture the entire duration of the spray. Figure 2-14 represents a timing diagram for high-speed Schlieren setup.

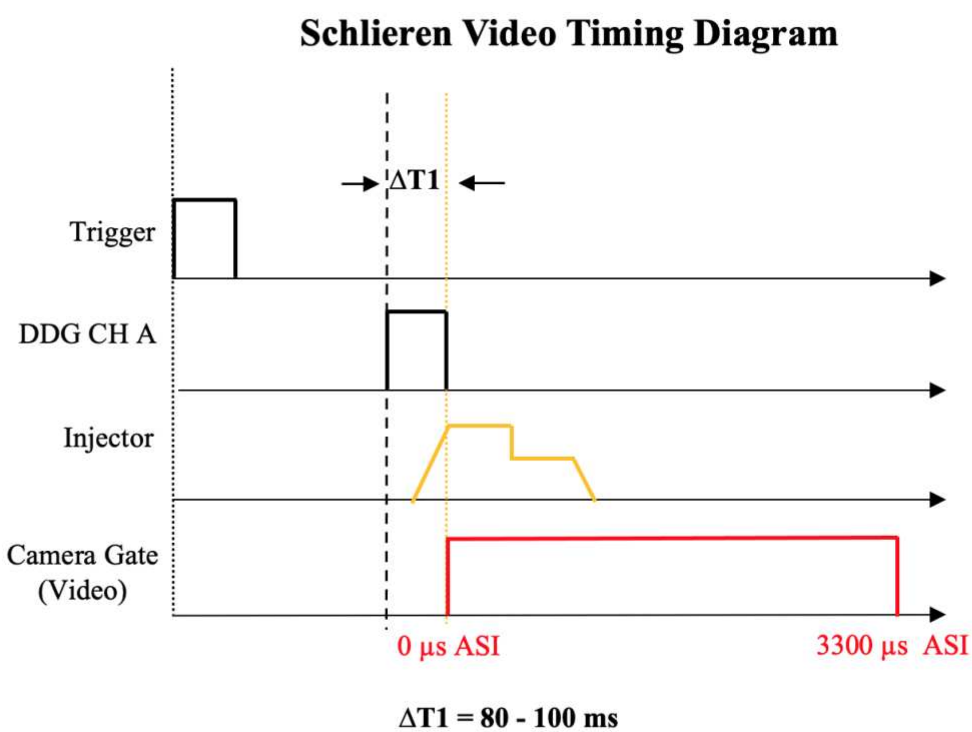

Figure 2-14 Timing diagram for high-speed Schlieren imaging. Displaying the timing scheme needed to capture the start of injection using the Photron camera

2.5.4 Schlieren Imaging Post Processing

Each Schlieren images was scaled to provide a consistent light intensity for the entire data set and compensate for any light fluctuations caused by the LED. The background was subtracted from each respective set of experiments clearly defining the boundaries of the spray. However, background subtraction produced undesired remnants in the spray core of the image, which was fixed by replacing the non-zero pixels of the image. This helped to enhance the resolution and fix spray defects with minimal manipulation to raw data. Delphi Schlieren image's backgrounds were subtracted from each respective set of experiments defining the spray boundaries. An accumulation image for each photo within a set of experiments was placed over the given image to present the spray morphology at a given time.

Once the images were processed, maximum axial vapor penetration lengths and maximum normal penetration widths, as seen in Figure 2-11c, were measured using simple edge finding algorithms in MATLAB, and plotted with respect to time. The vapor penetration speed was calculated by taking a first-order derivative with respect to time of the formally measured maximum penetration lengths. For the Spray-G data set, three tests were recorded for each test condition and the collected data was averaged to improve repeatability and increase accuracy of the measurements. The spray was imaged for 1200 μs after spray injection (ASI) for each condition. Similarly, for the Delphi data set, three tests were recorded at each test condition to increase reliability and accuracy. These measurements help to provide detailed quantitative analysis in addition to the qualitative Schlieren images characterizing the spray morphology. Schlieren provides a global image of both vapor and liquid regions of the spray and a 3-dimensional spray structure (Figure 2-11b). This structure is then accumulated into one plane, decreasing plume-to-plume distinctions and resolution.

Since propane when injected is considered a two-phase mixture Schlieren does not provide a clear distinction between the vapor and liquid regions of the spray as shown in Figure 2-11c. While Schlieren provides detailed visualization of the global spray morphology there is a need for an advanced diagnostic techniques to compensate for limitations of Schlieren imaging.

2.6 Mie Imaging

As previously stated, Mie scattering is an elastic light scattering technique used to capture scattered light off of liquid droplets within a spray. In this study liquid penetration lengths are recorded and plotted to provide information to help tune modeling efforts.

2.6.1 Mie Imaging Set-up

A Continuum Nd: YAG laser was used to produce a 532 nm beam with 25 ns pulse width and 7 mJ of energy per shot. The setup for Mie testing consisted of two 50 mm Nd: YAG mirrors designed to reflect 532 nm light to the height of the injector tip. Two cylindrical optics: a converging lens with a focal length of 1000 mm, and a diverging lens with a focal length of -75 mm (Figure 2-15a) were used to create a thin laser sheet. This laser sheet was 100 µm thick, bisecting the front nozzle of the fuel injector shown in Figure 2-15b. The laser sheet provides the ability to precisely bisect the leading nozzle for both Spray-G and Delphi injectors, as seen in Figure 2-15c.

An Andor iStar sCMOS camera was used along with a Vivitar 75-300 mm macro focusing camera lens to capture the spray image with a spatial resolution of 49 µm/px and image size of 2560 x 2160 pixels at various instances of time, ranging from 25 µs to 1200 µs ASI for the Spray-G injector and 250, 500, and 750 µs for the Delphi injector.

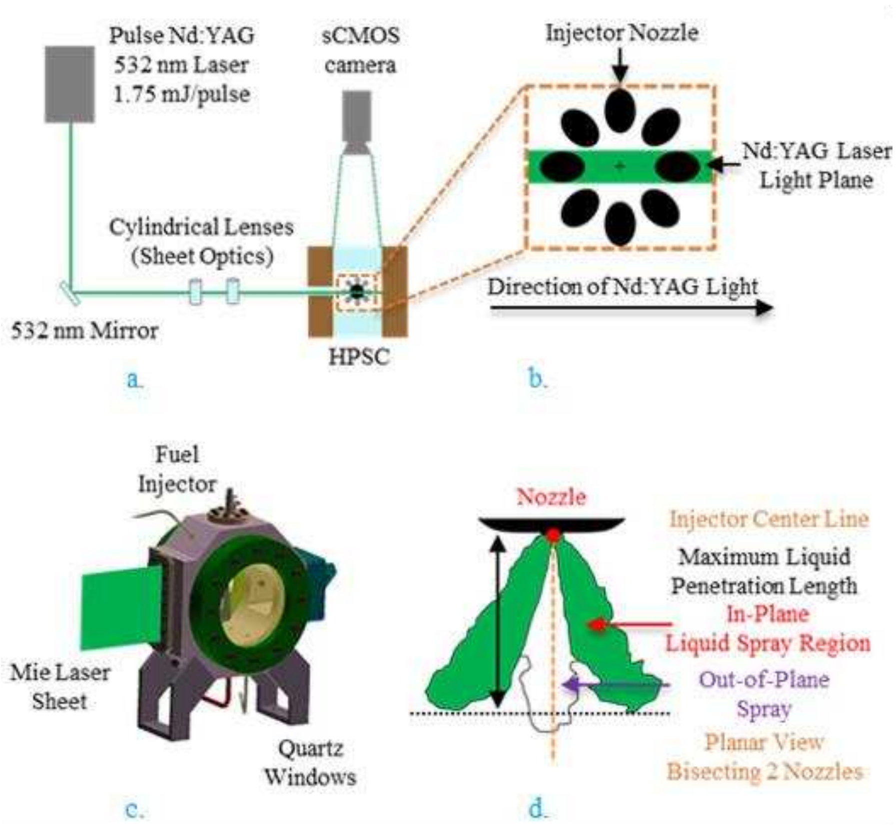

Figure 2-15 (a) Top-view schematic of planar Mie scattering imaging setup, (b) alignment of Spray-G injector relative to the laser sheet bisecting the front and back nozzles, (c) isometric rendering of HPSC and Mie laser sheet, and (d) Mie schematic with corresponding illuminated liquid spray plumes in the plane of the laser sheet, and associated nomenclature.

2.6.2 Mie Imaging Timing

Similar to the Schlieren timing setup, the camera, fuel injector, and laser were synchronized using the external DDG triggered by the LECM. The actual laser and camera shot timings relative to the start of injection were measured using an additional current probe and oscilloscope and was found to be within ± 15 µs. The Andor camera was gated for 15 ns to capture the center of the laser pulse. Figure 2-16 shows, a general Mie imaging timing diagram. This diagram portrays a generalized timing diagram as ΔT2 would change to appropriately capture the spray at a time the user would desire.

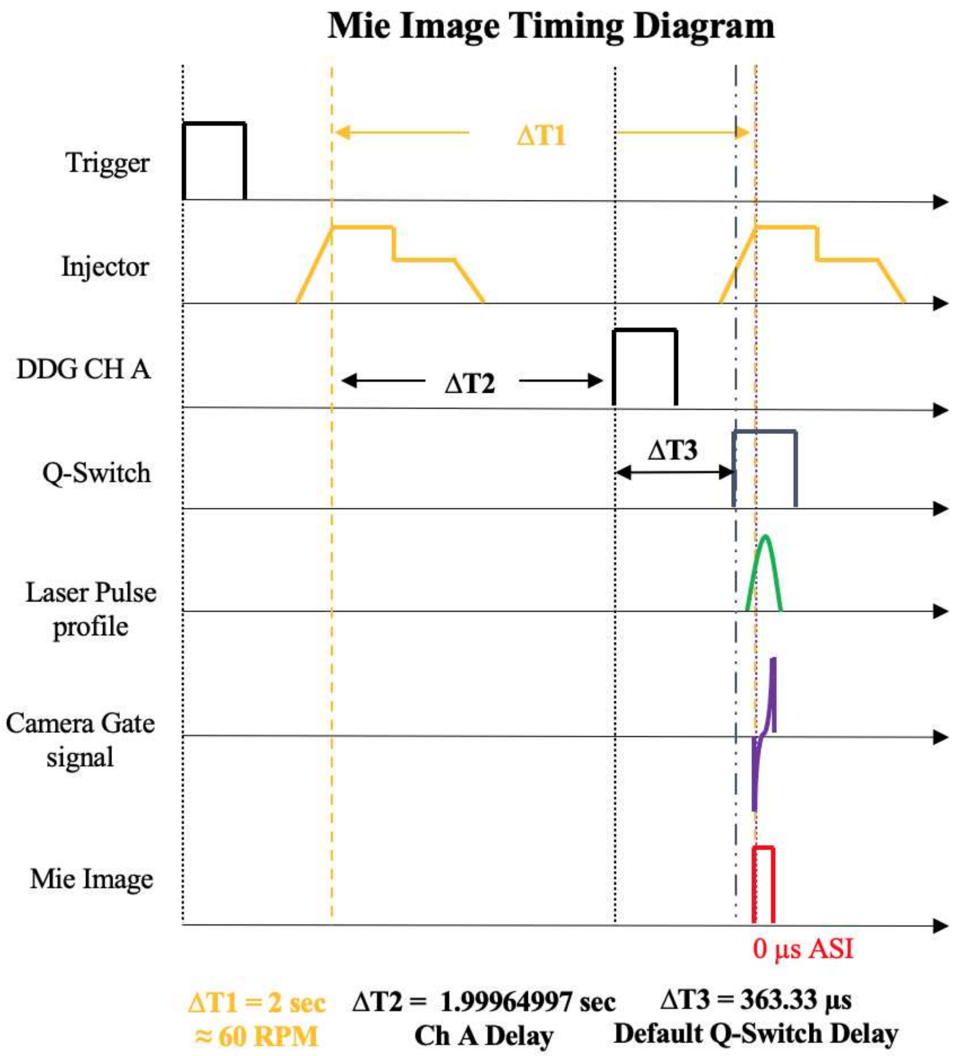

Figure 2-16 General timing diagram for planar Mie imaging. Displaying the need of an initial injection event to trigger the system and capture the correct time initiated by the use. Timing intervals would change which would correspond to 200 μs, 500 μs, and 750 μs ASI

2.6.3 Mie Imaging Post Processing

The collected 16-bit Spray-G Mie images, were processed using a set of standard multi-step image processing techniques. It was observed that the laser energy had a gaussian distribution along the axis of injection; to address this, each Mie images were normalized using the spatial energy distribution to make the energy of the laser sheet spatially constant. Minimum and maximum thresholds were set to eliminate background noise, reflections from the chamber, and secondary Mie scattered light from out of plane spray. Once processed, similar techniques to Schlieren were employed to binarize the spray image and detect edges of the individual plume, i.e., the front plume (left as seen in Figure 2-16d). It was also observed that the laser sheet attenuates as it propagates through the chamber perpendicular to the axis of injection, due to the presence of spray. This, however, did not have an impact on the measurements, as the front edge of the spray was free of this aberration and hence, was used for quantitative measurements. Delphi Mie images were measured using ImageJ software, where the furthest edge of the spray was recorded and then plotted to obtain liquid penetration lengths. Unlike Spray-G Mie images, Delphi Spray-G images did not have a consistent trend in laser intensity across the spray structure, and a correction factor could not have been applied. Similarly, to Schlieren imaging, both Spray-G and Delphi datasets were tested three times for each test condition to provide reliability and accuracy. Once the front edge was defined, the corresponding pixels were calibrated, averaged over three iterations, and then plotted to obtain maximum liquid penetration lengths, widths, and speeds as a function of time.

2.7 Testing Conditions

To observe the spray morphology at engine-like conditions as well to validate the experimental testing facility, test conditions specified by ECN using the Spray-G injector were utilized. Table 1, displays a testing array of conditions that have been standards within the ECN community [27], [55]–[58]. These test conditions are denoted as G2, G2C, G3, and G3C. The G2 conditions are representative of an early injection event creating a homogenous mixture, likewise, G3 conditions represent part-load, throttled, early injection conditions in a DI engine cylinder. Iso-octane and propane are widely used as surrogates for gasoline and LPG fuels, respectively [27], [48], [59]. As many studies have explored the spray morphology and mixing processes of iso-octane using the ECN Spray G fuel injector, iso-octane was used to verify the experimental setup [53], [54], [59].

Table 1: Test matrix including Engine Combustion Network's identified experimental conditions for Spray-G fuel injector

Control Parameter	**Test Conditions**			
	G2C	**G2**	**G3C**	**G3**
Fuel	Iso-octane and Propane			
Injector	Spray G – 8-hole Axisymmetric			
Electric Injection Duration [μsec]	680			
Actual Injection Duration [μsec]	870			
Ambient Temperature (T_{amb}) [K]	293	333	293	333
Fuel Temperature (T_{fuel}) [K]	293	363	293	363
Ambient Pressure (P_{amb}) [Bar(a)]	0.5	0.5	1	1
Injection Pressure (P_{inj}) [Bar(g)]	200			

Along with the verification of the experimental setup, an additional large test campaign was also designed and tested using the Delphi 7-hole injector to study propane. The test matrix was designed with the notion of conditions that would be seen within an engine at different operating conditions, such as start-up and idle. Figure 2-17 displays targeted pressures that are representative of in-cylinder engine pressure traces.

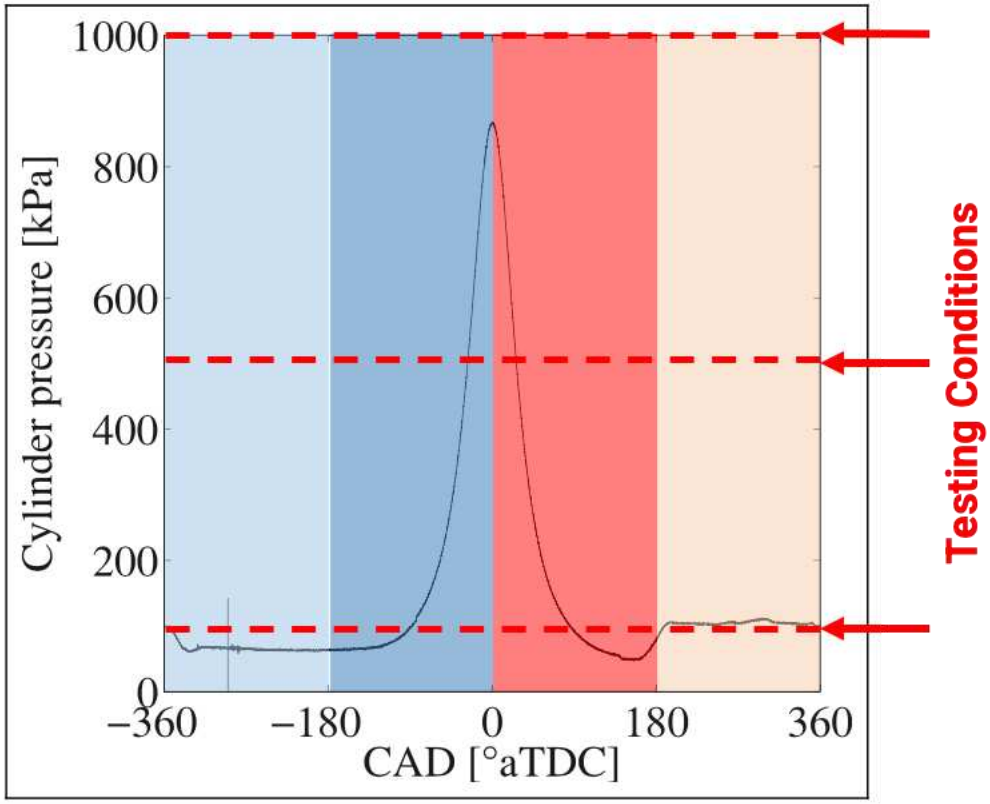

Figure 2-17 Engine In-cylinder pressure traces at specified testing conditions [50]. Displaying potential strategies for either early or late injection schemes. Additionally displaying pressure traces that were considered in the Delphi test matrix

The targeted pressures of 0, 5, 10 bar (gage) cover a wide range of engine conditions and should provide information for most operating conditions. A pressure measurement of 0 bar (gage) similarly to ECN conditions, represents an early injection event with homogenous mixing or part-load, throttled conditions. A pressure measurement of 5 bar (gage) represents, a late injection when the compression stroke has already started, and 10 bar (gage) represents a late injection, when the compression stroke has almost finished and potentially has a forced induction device (Turbocharger, super charger). Similar to pressure traces seen in a combustion chamber, temperatures are also targeted at similar conditions for both the fuel injector and chamber. Figure

2-18 shows a test array with varying of both chamber and fuel injector, temperatures and pressures.

Test #	T_cvc [C]	T_inj [C]	P_cvc [Bar]	P_inj [Bar]
1				100
2			0 (gage)	200
3				300
4				100
5		15	5 (gage)	200
6				300
7				100
8			10 (gage)	200
9	50			300
10				100
11			0 (gage)	200
12				300
13				100
14		50	5 (gage)	200
15				300
16				100
17			10 (gage)	200
18				300
19				100
20			0 (gage)	200
21				300
22				100
23		15	5 (gage)	200
24				300
25				100
26			10 (gage)	200
27				300
28	85			100
29			0 (gage)	200
30				300
31				100
32		85	5 (gage)	200
33				300
34				100
35			10 (gage)	200
36				300

Figure 2-18 Testing array at engine-like conditions for Delphi fuel injector. This test matrix covers a wide range of potential injection strategies that would be used in a field study

2.8 Numerical Spray Simulations

This simulation campaign was carried out solely by Lorenzo Nocivelli and Katherine Aszalos at Argonne National Laboratory, to whit provided guidance and previous knowledge to help the experimental campaign.

The simulation campaign was carried out with the commercial CFD software CONVERGE (v3.0) [60]. The injection was modeled with a two-tiered approach. First, the simulation of the two-phase internal nozzle flow was carried out to provide insight into the trends of the mass flow rates, and the initial development of the spray plumes for each fuel. Secondly, the results were used to inform the Lagrangian parcel spray model, which was then implemented to simulate the full HPSC domain.

2.8.1 Nozzle-Flow Simulation Setup

Nocivelli et al. follows the approach from previous work [61], which characterizes fuel jet dynamics produced by a nozzle. The nominal geometry of the Spray-G injector is a defining feature of the computational system, which was joined with a hemispherical open-outlet boundary as shown in Figure 2-19a. The multi-phase flow was handled by a single-fluid mixture model which considers the relative velocity between phases in local equilibrium. Liquid, gas, and fuel vapor were treated as different phases in a multi-component mixture, where the phase change was handled through source terms in the species equation. This assumes local and instantaneous vapor quality evolves towards an equilibrium value according to a linear trend, based on a characteristic time scale. The characteristic time scale depends on the properties of the fluids and the local pressure and void fraction values, and its magnitude was determined according to an empirically obtained constant. Previous results [62], show that the value of the constant allows modification of the speed during phase-change, and the behavior of the spray in the near nozzle region.

A base mesh of 240 µm grid was created using the cut-cell method and was then refined to 15 µm at regions of interest, as shown by the center-plane of the injector in Figure 2-19b. Adaptive mesh refinement was used to identify the dynamic grid to track plume evolution in the open chamber. The adaptive mesh refinement was based on the second derivative of the velocity and species mass fraction.

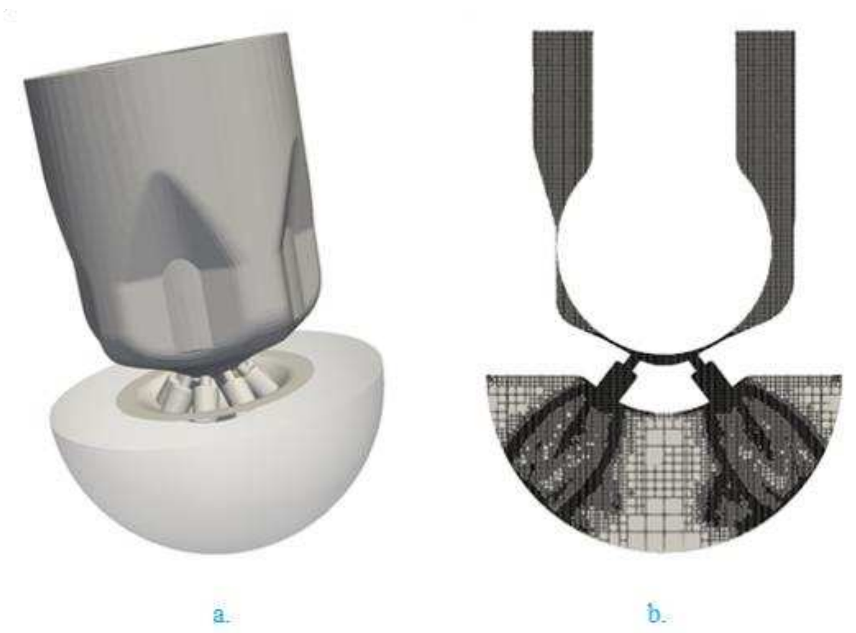

Figure 2-19 (a) Eulerian nozzle flow CFD domain for the ECN's Spray-G injector, and (b) centerline of full needle lift of the numerical grid

Both iso-octane and propane's, needle motion was prescribed according to the X-ray measurement by Sforzo et al. [45]. These measurements were collected for different fuel at previously defined ECN's G2 conditions [55], and initializing the motion from a minimum gap of 6.6 µm, according to the setup proposed by Yue [31], [63].

As stated earlier, the nozzle geometry of a fuel injector influences the numerical modeling significantly, increasing the chances for inaccurate geometry measurements. Figure 2-20 depicts the CFD domain for the Delphi injector and a model of the injector tip and individual nozzles. The nozzle hole diameter that was considered a “best-fit” was a diameter of 138 µm, which was based on provided nozzle measurements from CZero at a variety of nozzle flow simulations that varied the nozzle diameter.

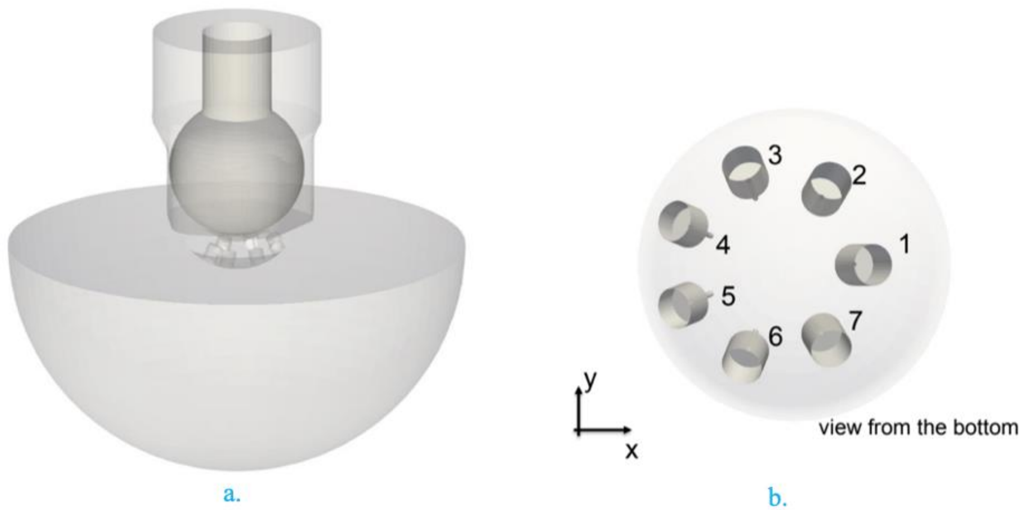

Figure 2-20 (a) Eulerian nozzle flow CFD domain and internal geometry for 7-hole Delphi injector, and (b) bottom-view of Delphi injector tip and orientation

2.8.2 Lagrangian Spray Simulations

The simulation of the spray in the HPSC was obtained with the Lagrangian-Eulerian method and the liquid phase was modeled according to the discrete droplet model [31]. The geometry of the chamber was discretized with the Cartesian cut-cell method (Figure 2-21a). This is where a base grid size of 1.6 mm was created and relied on adaptive-mesh refinement (AMR) to improve the cells according to the second derivative of velocity and fuel vapor mass fraction, as shown in

Figure 2-21b. To introduce phase-change caused by flash-boiling, the model proposed by Adachi et. al [47] was implemented into the numerical simulation. This model accounts for local and instantaneous super-heat degree of the fuel in the chamber in terms of differences between the local temperature and saturation temperature of the fuel at a local pressure. The implementation in CONVERGE is reported by Nocivelli in a previous study [62]. The blob-injector model initialized the spray parcels, which informed the results obtained by the nozzle-flow simulation, in terms of mass flow rate, and droplet momentum, plume direction, and plume angle to best represent the ensuing spray.

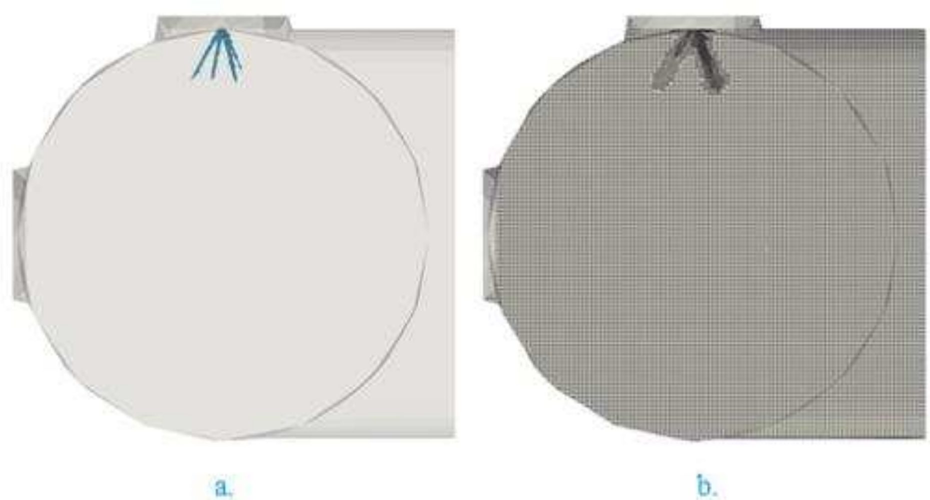

Figure 2-21 Lagrangian spray CFD domain for the injection in HPSC (a), and (b) numerical grid on the centerline with AMR.

Since propane has an unconventional spray behavior, where vaporization and collapse play a major role, the numerical spray results were processed to reproduce experimental Schlieren and Mie scattering data. Two processing routines aim to describe the full spray morphology and the liquid phase development respectively.

The Schlieren images were reproduced by projecting the magnitude of the gradient of the gas-phase density along the line-of-sight, as shown in Figure 2-22a. The resulting 2D data was normalized on its maximum value to provide a qualitative image of the spray morphology as in Eq. 1.

$$I_{Sch,norm} = \frac{\sum_i^{cell\_X} grad_X(rho)}{\max\left(\sum_i^{cell\_X} grad_X(rho)\right)} \tag{1}$$

The light scattered from the liquid phase was reproduced by projecting over the line-of-sight, with the frontal area of the spray parcels. Figure 2-22b shows a sampling region representative of the laser sheet. This 2D projection was then normalized on its maximum value which produced a qualitative representation of measure light scattered, according to Eq. 2.

$$I_{norm} = \frac{\sum_i^{Nparcels} n\_drop_i D_i^2}{\max\left(\sum_i^{Nparcels} n\_drop_i D_i^2\right)} \tag{2}$$

The location and thickness of the sampling region replicates the experimental setup. The resulting images from both routines are proportional to the measured light intensity trends, but without implementing the laser scattering detailed dynamics, the focus of the validation is set on the boundaries of the spray profiles.

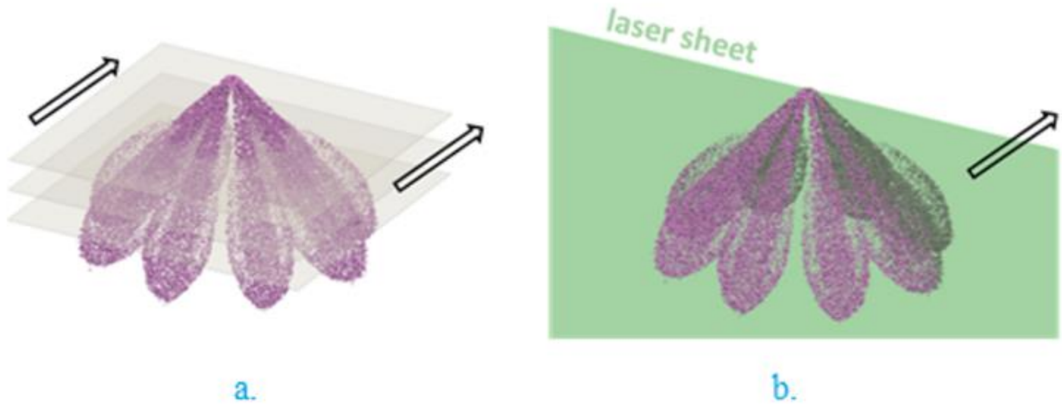

Figure 2-22 Schematic of the spray simulation processing regions of interest: sampling region representing the (a) planar gradient density sampling of the gas phase to reproduce Schlieren data, and (b) the Mie laser sheet.

To highlight the fuel jet evolution within the HPSC the gathered light intensity profiles are binarized. The vapor penetration was determined by the maximum axial distance computed from binarized images generated with a threshold of $I_{Sch,norm} > 0.02$. To be consistent with the experimental results and validate the simulation, these proposed techniques were used as a comparison method.

Chapter 3 - Experimental Results

3.1 Introduction

The next section presents the experimental measurements that were gathered using both Schlieren and planer Mie scattering imaging techniques. These imaging techniques assisted in mapping out the spray morphology for propane and iso-octane for the Spray-G injector and propane for the Delphi injector. The qualitative and quantitative results produced by the experimental spray visualization techniques provided a strong comparison to aid the development of numerical models that would accurately portray the spray morphology.

3.2 Validation of Experimental Setup

To ensure the correct operation of the experimental facility, direct qualitative and quantitative comparisons were made with both experimental and numerical results from previous literature using iso-octane. Lacey et al. conducted similar studies using the Spray-G injector at G3 conditions. As shown in Figure 3-1, a direct qualitative comparison can be made between Lacey et al. experimental results for iso-octane and the experimental results presented in this study. These two series show iso-octane at similar time stamps, exhibiting distinct features, such as individual spray plumes, a wide spray angle, and overall, the two sprays seem identical in size and shape. Additionally, Nocivelli et al. also displays numerical simulations of iso-octane at G3 conditions, seen in Figure 3-1. These numerical simulations, likewise, closely resemble both experimental results produced from Lacey et al. and this study. There is an overall good qualitative agreement between previous experimental and numerical results.

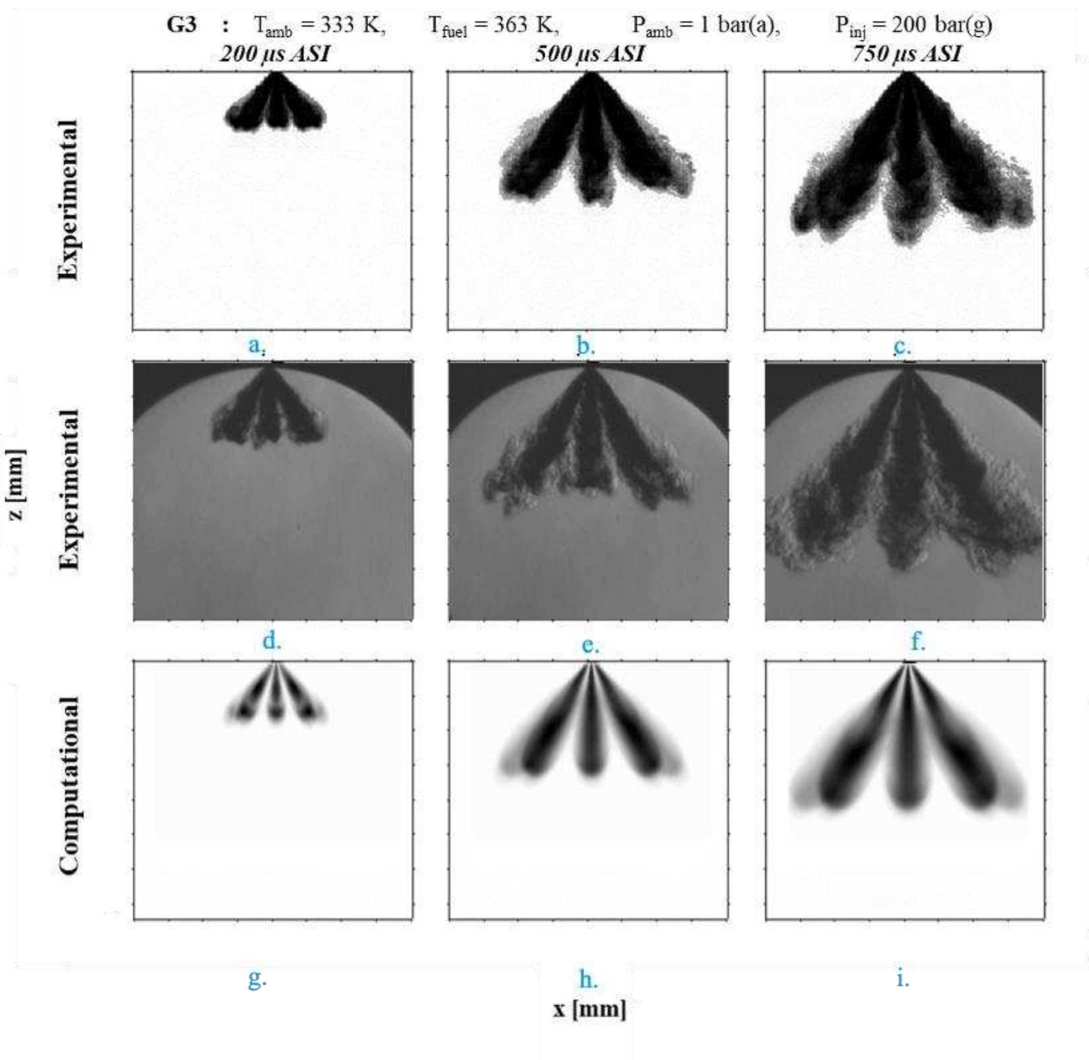

Figure 3-1 Direct qualitative comparison of experimental results produced in this study with experimental results produce from Lacey et al. and numerical results produced by Nocivelli et al. Images not to scale.

Qualitative and quantitative comparisons provide meaningful information which help confirm the experimental results are similar to previous studies. As seen in Figure 3-2, two lines representing experimental and numerical results, are plotted displaying the vapor penetration length of iso-octane at G3 conditions. These data driven results represent a good qualitative agreement between these two methods.

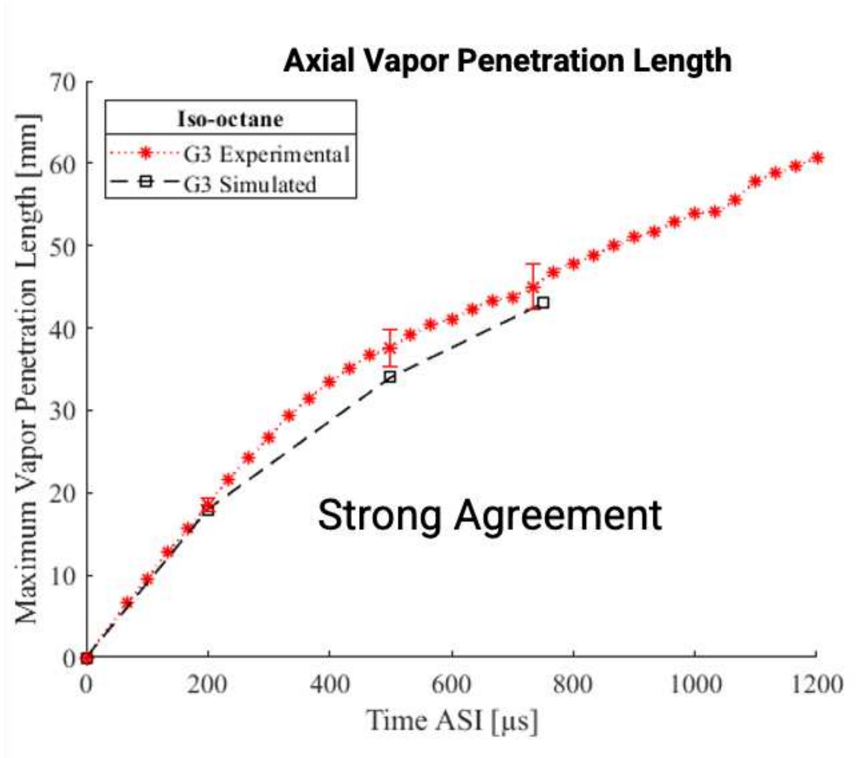

Figure 3-2 Quantitative agreement for iso-octane at G3 conditions between numerical and experimental results displaying a strong agreement

Although the numerical simulations slightly underpredict the vapor penetration length, there is an overall good agreement between the results. Both qualitative and quantitative results from previous literature have displayed a similar outcome to the experimental results presented in this study, therefore validating the experimental setup and facility.

3.3 Experimental Spray-G High-Speed Schlieren Results

The results presented in this study for the Spray-G injector represent the work and results of Windell et al. [64]. Figure 3-3 shows Schlieren imaging for iso-octane and propane at G3C and G3 conditions at three timesteps: 200 µs, 500 µs, and 750 µs ASI. Figures 3-3 (a-f), depicts iso-octane, having a wide injection angle, typical spray pattern, and three individual plumes are clearly distinguishable. The spray also appears to be symmetric at the presented time stamps for both G3C and G3 conditions. When increasing temperature from G3C ($T_{fuel} = T_{amb} = 20$ °C) to G3 ($T_{fuel} = 90$ °C and $T_{amb} = 60$ °C) iso-octane's spray structure is marginally affected, when observing the penetration lengths and widths. Additionally, for iso-octane, a clear distinction between darker/liquid spray cores and lighter/vapor regions can be seen.

On the other hand, propane in Figure 3-3 (g-l) depicts greater plume-to-plume interactions influencing a much narrower overall injection angle creating a larger singular jet. The spray structure of propane is observed to have a strong dependence on temperature. When observing propane at colder cases (G2C and G3C), the initial injection of the spray starts with a wide angle and small amounts of vaporization. Over time the spray structure begins to collapse into a singular spray jet. Increasing the temperature of the fuel and the chamber (G2 and G3) amplifies this behavior as seen in Figure 3-3 (j-l). Contrary to the behavior observed in Figures 3-3 (g-i), propane's collapse is more evident at G3 conditions, seen in Figures 3-3 (j-l), as the width of the jet is narrower and stays consistent throughout the injection duration; propane also propagates further axially at hotter conditions. At G3 conditions, propane's axial penetration length is much greater than iso-octane for all tested conditions. Propane does not display a clear distinction between liquid and vapor regions for both G2/C and G3/C cases.

The quantitative vapor penetration measurements of iso-octane, agree strongly with the qualitative analysis. As seen in Figures 3-4 (a) and 3-4 (b), both the penetration lengths and widths overlap within the margin of error over the duration of the injection. A small deviation of around ± 7.5 mm for both penetration lengths and widths can be seen after 870 μs ASI. The penetration lengths increase in the order of G3 < G2 ≈ G3C < G2C, i.e., penetration lengths are inversely proportional to temperature and pressure. Temperature on the other hand, has a negligible effect on the penetration widths. Figure 3-4 (b) also reveals that penetration widths are inversely proportional to pressure after the end of injection. As seen in Figure 3-4 (c), iso-octane at the start of injection exhibits higher velocities at higher temperatures but, decreases at a faster rate compared to colder conditions, which results in a slower velocities at the end of injection.

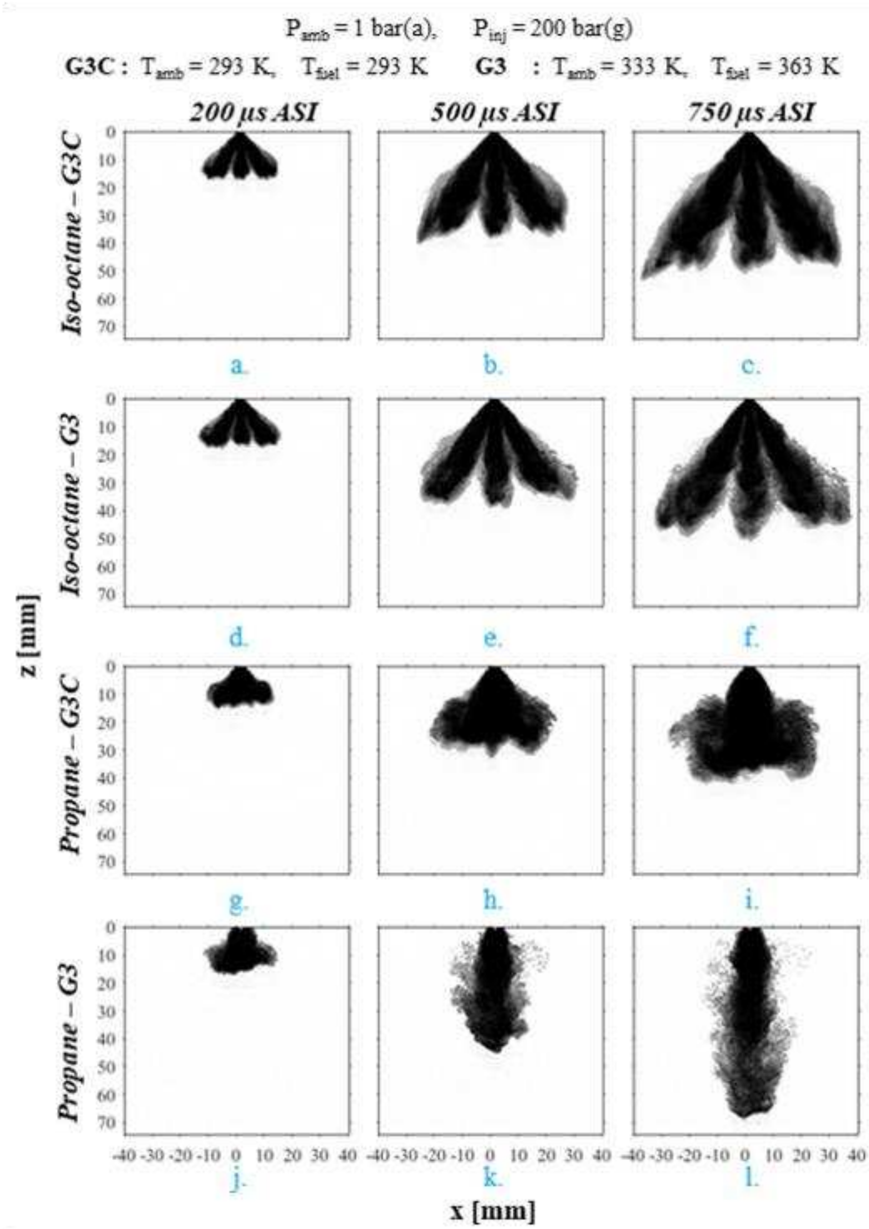

Figure 3-3 High-speed Schlieren images for Spray-G injector at various timesteps after the start of injection for various fuels and conditions, namely: (a) - (c) for iso-octane at G3C, (d) - (f) for iso-octane at G3, (g) - (i) for propane at G3C, and (j) - (l) for propane at G3 condition, respectively.

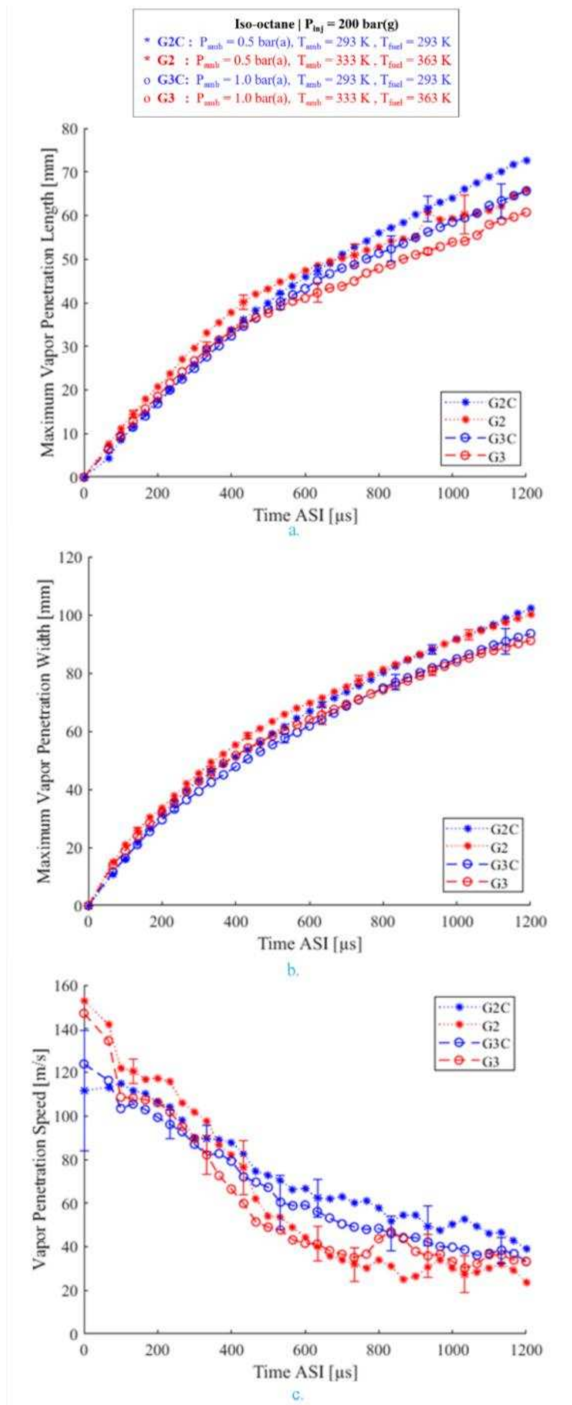

Figure 3-4 Measurements for iso-octane including a) maximum axial vapor penetration length, b) maximum transverse vapor penetration width, and c) vapor penetration speed of iso-octane. Error bars are included at suitable timestamps for improved legibility. Mean error of ± 2.0 mm in vapor penetration lengths, ± 1.8 mm in vapor penetration widths, and ± 8.3 m/s in vapor speeds were observed over all tests for iso-octane.

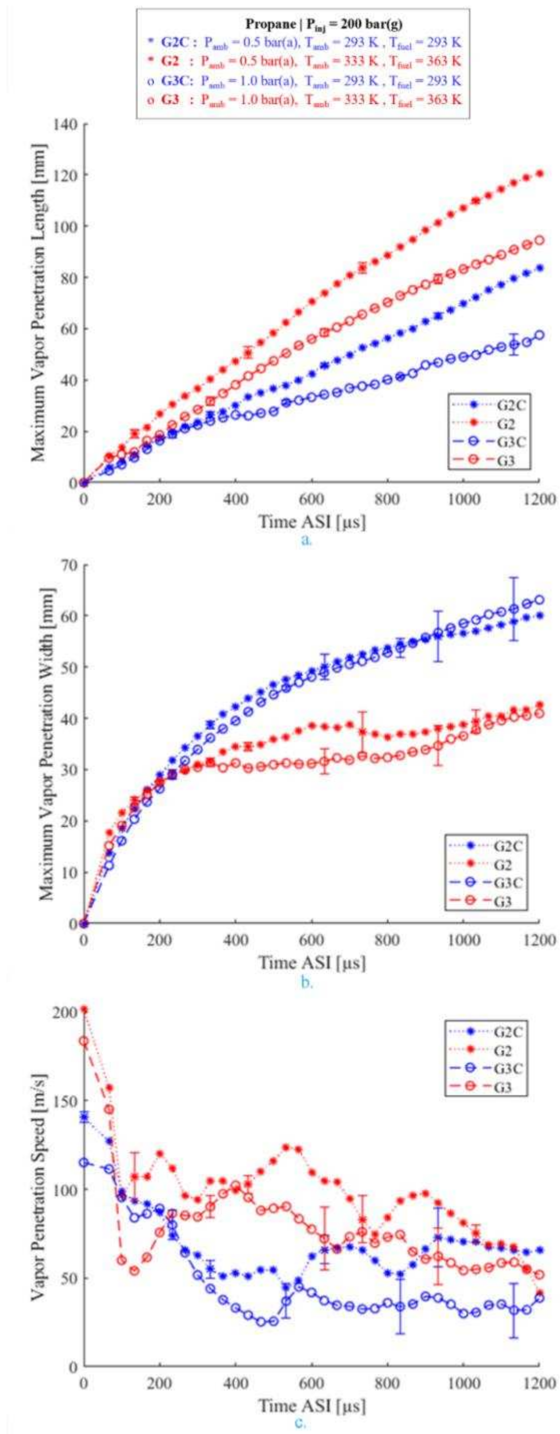

Figure 3-5 Measurements for propane including a) maximum axial vapor penetration length, b) maximum transverse vapor penetration width, and c) vapor penetration speed of propane. Error bars are included at suitable timestamps for improved legibility. Mean error of ± 1.5 mm in vapor penetration lengths, ± 2.4 mm in vapor penetration widths, and ± 8.6 m/s in vapor speeds were observed over all tests for propane.

On the contrary to iso-octane, propane displays a clear trend for penetration lengths and the influences of various conditions. As seen in Figure 3-5 (a), propane's axial penetration length increases for conditions in the order of G3C < G2C < G3 < G2, exhibiting that propane is directly proportional to temperature and inversely proportional to pressure. Generally, propane displays larger axial penetration lengths than iso-octane by approximately 20 mm more at 1200 μs. Propane's penetration widths as seen in Figure 3-5 (b) are considerably less compared to iso-octane, approximately 50 mm less at 1200 μs. In addition, qualitative images in Figures 3-3 (g-l), display a narrower singular jet of propane. These features of a narrower and longer jet of propane also impact the penetration speeds plotted in Figure 3-5 (c), which are approximately 30 m/s higher than that of iso-octane. A higher initial axial velocity at hotter temperature conditions (G2 and G3) is seen compared to colder temperature conditions (G2C and G3C). Similarly, propane's vapor penetration speeds, as shown in Figure 3-5 (c), and distinctive features are exhibited, such as a steep drop at 100 μs for each condition, and pulsating velocities after.

3.4 <u>Experimental Spray-G Planar Mie Scattering Results</u>

Planar Mie scattering provides a finer resolution and enhances the liquid regions of a singular spray plume. Figure 3-4 displays iso-octane and propane at G3C and G3 conditions at previously stated time stamps. As seen in all images in Figure 3-4, only a single plume is seen in the plane of the laser sheet, this is due to laser attenuation as mentioned earlier. In Figure 3-6 (a-f), a singular, distinct narrow liquid core for iso-octane is seen that has an overall wide injection angle.

The temperature difference in G3C and G3 conditions, are seen to affect the liquid penetration length, while injection spray angle and horizontal spray penetration are minimally changed. These results from planar Mie agree strongly with the results obtained for iso-octane using Schlieren imaging (Figures 3-6 (a-f)). Figures 3-6 (g-i) and Figures 3-6 (j-l), present planer Mie scattering imaging for propane at G3C and G3 conditions, respectively. Similarly, Schlieren imaging of propane in most presented cases, is observed as a singular jet. This jet is unlike the singular front plume observed for iso-octane and is seen to be brighter, longer, more axial, and with a wider liquid core. When observing propane in Figure 3-6 (g), similarly to iso-octane a singular liquid spray plume is observed. As the spray progresses, shown in Figures 3-6 (h) and 3-6 (i), the spray structure begins to resemble a large singular spray jet. Likewise, Schlieren imaging at hotter G3 conditions, presents a liquid length of propane that is much longer than at colder G3C conditions. The penetration length of propane is also observed to be longer than that of iso-octane for all tested conditions.

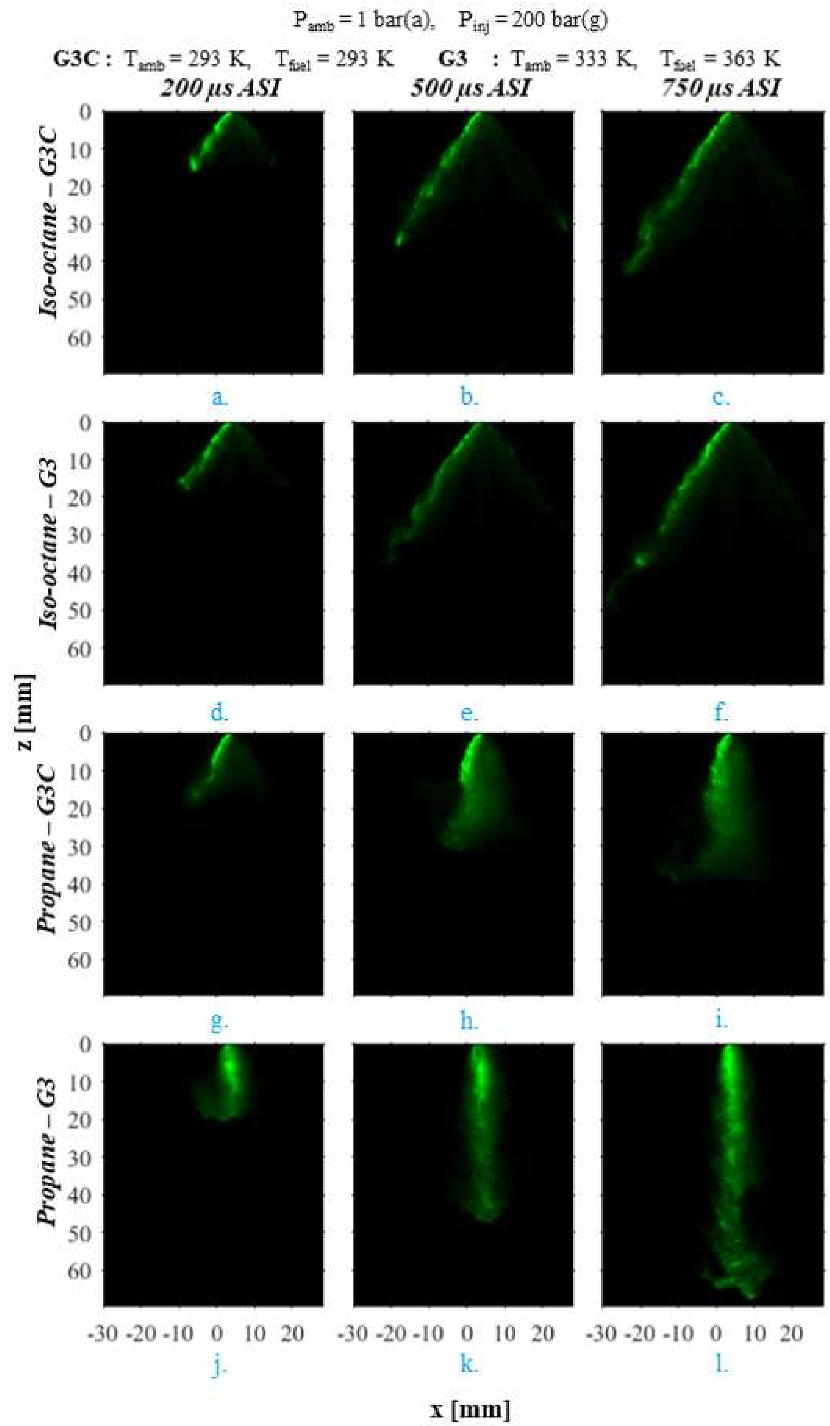

Figure 3-6 Planar Mie scattering images at various denoted timesteps (across) after the start of injection for various fuels and conditions (down), namely: (a) - (c) for iso-octane at G3C, (d) - (f) for iso-octane at G3, (g) - (i) for propane at G3C, and (j) - (l) for propane at G3 condition, respectively.

As seen in Figure 3-7 (a), the liquid penetration lengths for all conditions overlap until 400 µs ASI, with minor deviations approaching the end of injection. On the other hand, when observing hotter conditions (G2 and G3), the liquid penetration lengths begin to fall around 800 µs and decrease to zero at 1200 µs. This demonstrates that temperature is inversely proportional to the liquid penetration lengths for iso-octane spray propagation after the end of injection. Contrary to iso-octane, propane exhibits a clear trend for penetration lengths due to influences from the various conditions. The liquid penetration length is seen to be increasing for conditions in the order of G3C < G2C < G3 < G2, which is inversely proportional to pressure and directly proportional to temperature. This trend is identical for vapor penetration of propane as observed in Schlieren imaging. Propane's liquid penetration length, as seen in Figure 3-7 (b), falls sharply around 1000 µs at hotter temperature conditions, while at colder temperature conditions (G2C and G3C) the penetration lengths continue to increase. At colder conditions, liquid propane is seen to propagate farther than liquid iso-octane by approximately 15 mm more at 1200 µs, however, at hotter conditions no liquid is observed for both fuels at 1200 µs.

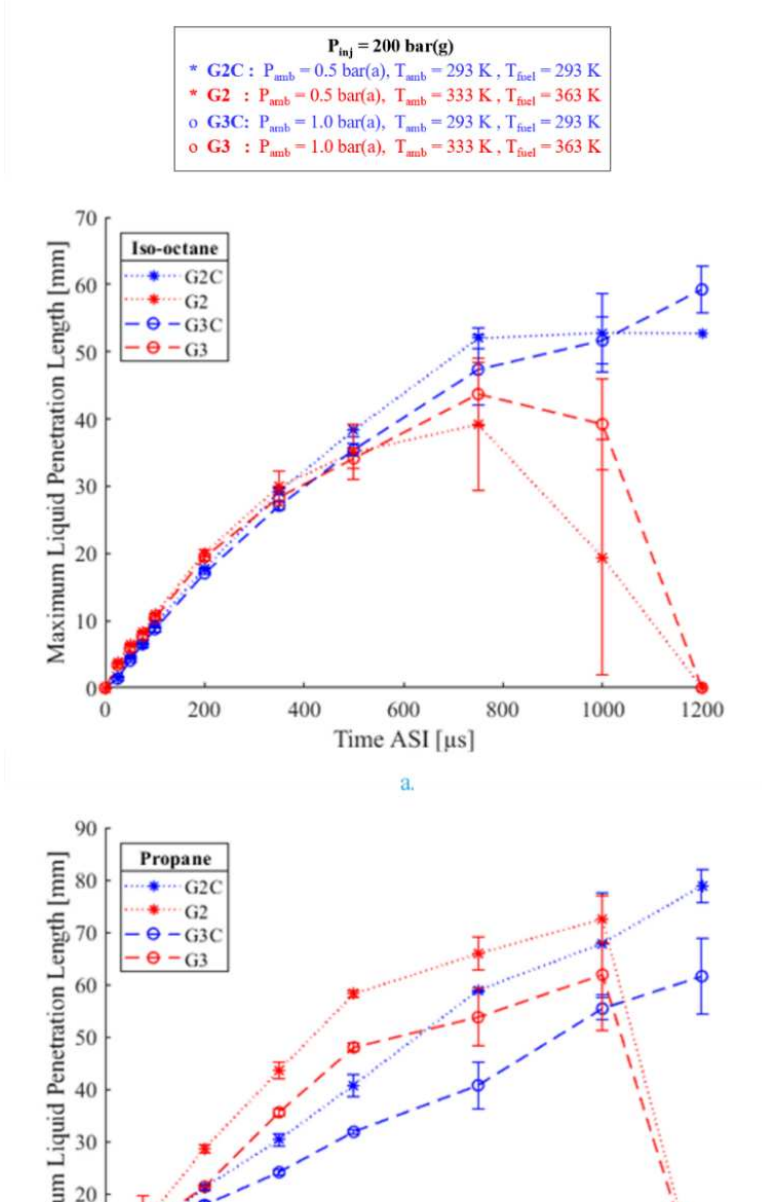

Figure 3-7 Maximum axial liquid penetration length measurements for a) iso-octane, and b) propane at corresponding conditions and timesteps measured using planar Mie Scattering imaging. A strong directly proportional relationship of the increased error and duration after start of injection was observed for both tested fuels.

Both vapor and liquid penetration lengths are crucial measurements that define the spray structure and provide useful information describing how the spray propagates through time.

Iso-octane and propane are presented in Figures 3-8 (a) and 3-8 (b), displaying their vapor and liquid penetration lengths at G3C and G3 conditions. For both conditions, it is observed that in Figure 3-8 (a) that iso-octane's vapor penetration length leads the liquid penetration length by a small margin for the entire duration of the spray. Contrary to hotter temperature conditions, the liquid starts to fall significantly once injection has ended, causing the liquid-vapor difference to increase. Unlike iso-octane, a clear distinction can be made between the penetrations for hot and cold conditions for propane, as observed in Figure 3-8 (b). For G3C conditions, liquid and vapor mostly overlap for the entirety of the spray propagation, however, the penetration length for the cold case is less than the hotter case, about 40 mm shorter at 1200 μs. Unlike the overlap as seen in G3C, G3 cases show a steep drop in liquid penetration after the end of injection, leading to vapor penetrating to 90 mm and no liquid at 1200 μs.

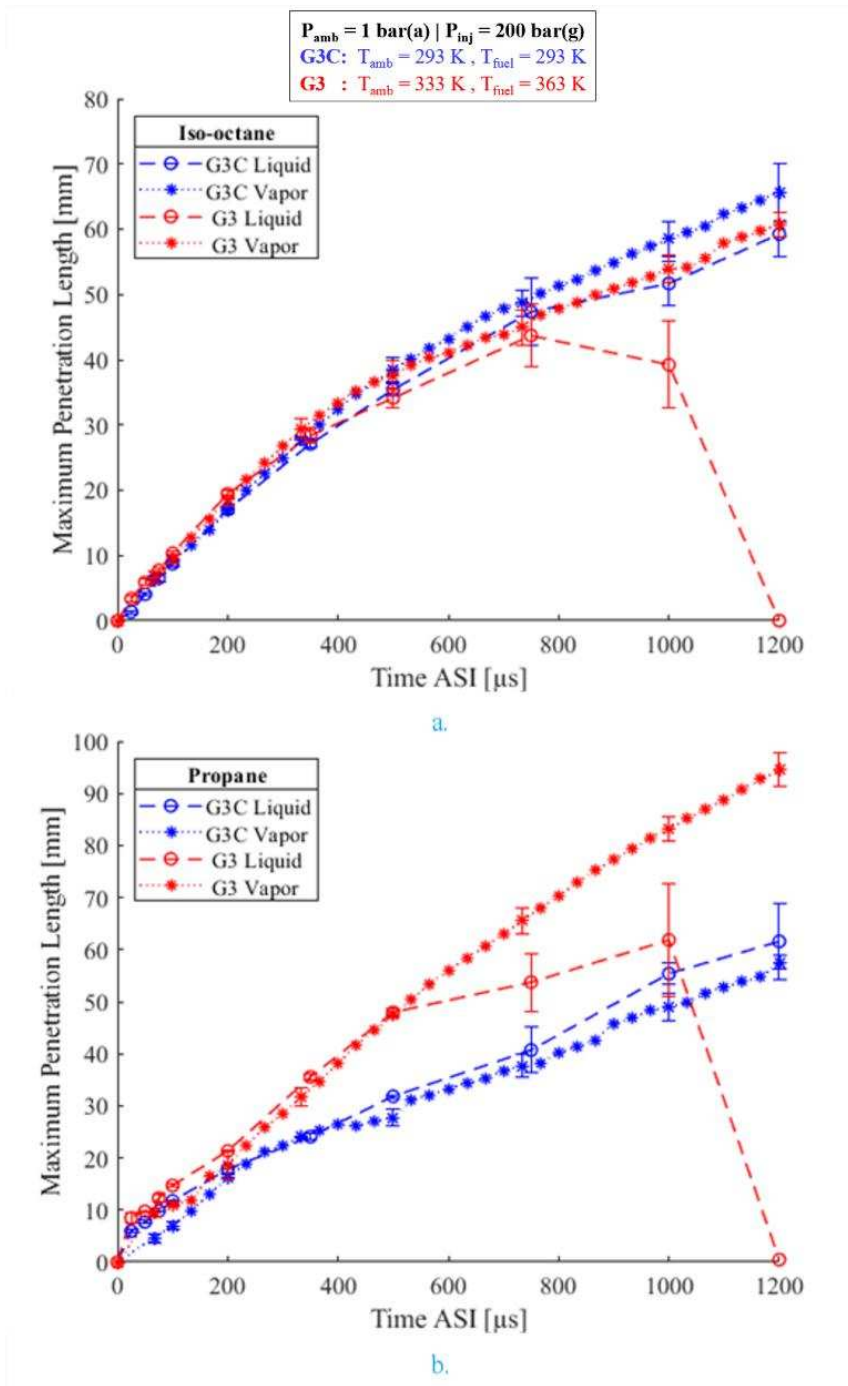

Figure 3-8 A comparison of maximum axial liquid vs. vapor penetration length for a) iso-octane, and b) propane at corresponding conditions and timesteps as a combined effort of high-speed Schlieren and planar Mie scattering imaging techniques. The error ratios are same as observed in corresponding single phase experimental results.

3.5 Experimental Delphi High-Speed Schlieren Results

Figures 3-9 – 3-11 shows Schlieren imaging for the Delphi injector injecting propane at engine-like conditions at three timestamps: 200 μs, 500 μs, and 750 μs ASI. These conditions represent a wide array of potential temperatures and pressures that would be seen in heavy-duty engines. These conditions cover: T_{fuel} = 15, 50, and 85 °C, T_{cvc} = 50 and 85 °C, P_{fuel} = 100, 200, and 300 bar (gage), and P_{cvc} = 0, 5, 10 bar (gage). The average ambient pressure in Fort Collins, CO is around 0.85 bar. With such a large dataset collected (36 tests) it would be impractical to display every test and discuss trends that are portrayed by a smaller dataset. For this reason, only some test will be displayed both qualitatively and quantitatively, which will exhibit extremes of the overall dataset.

Figure 3-9 (a-c) depicts propane at three previously stated time stamps, and it can be observed at lower pressures, similarly to the Spray-G injector, propane exhibits large plume-to-plume interactions, which influences a much narrower injection angle creating a large singular jet. When comparing Figures 3-9 (a-c) and 3-9 (d-f), it is seen that chamber pressure influences the overall spray morphology. At lower pressures for all temperature cases, a singular jet is formed with a dark/liquid core. As temperature increases at lower pressures, the dark/liquid core within the jet is observed to shrink in size, indicating that temperature has a large influence on the spray structure, this feature can be seen progressing in Figures 3-9 (a-c) and 3-11 (a-c). Generally, all lower chamber pressure conditions, regardless of changing chamber and fuel temperatures, have a much larger penetration length. At higher chamber pressures, the spray structure has an initial injection angle that is much wider than lower chamber pressure conditions. Additionally, at high chamber pressures and low fuel and chamber temperature conditions, the fuel is observed to have a denser and darker spray region when compared to higher fuel and chamber temperature conditions. The spray structure seems to start at 200 μs, with a similar dense/dark core but, at later time stamps, the dense/dark liquid core seems to decrease. This can be contributed to the influence of higher fuel and chamber temperatures. This has also been observed at higher chamber pressures and fuel and chamber temperatures, where individual plumes are more apparent and become more distinguishable.

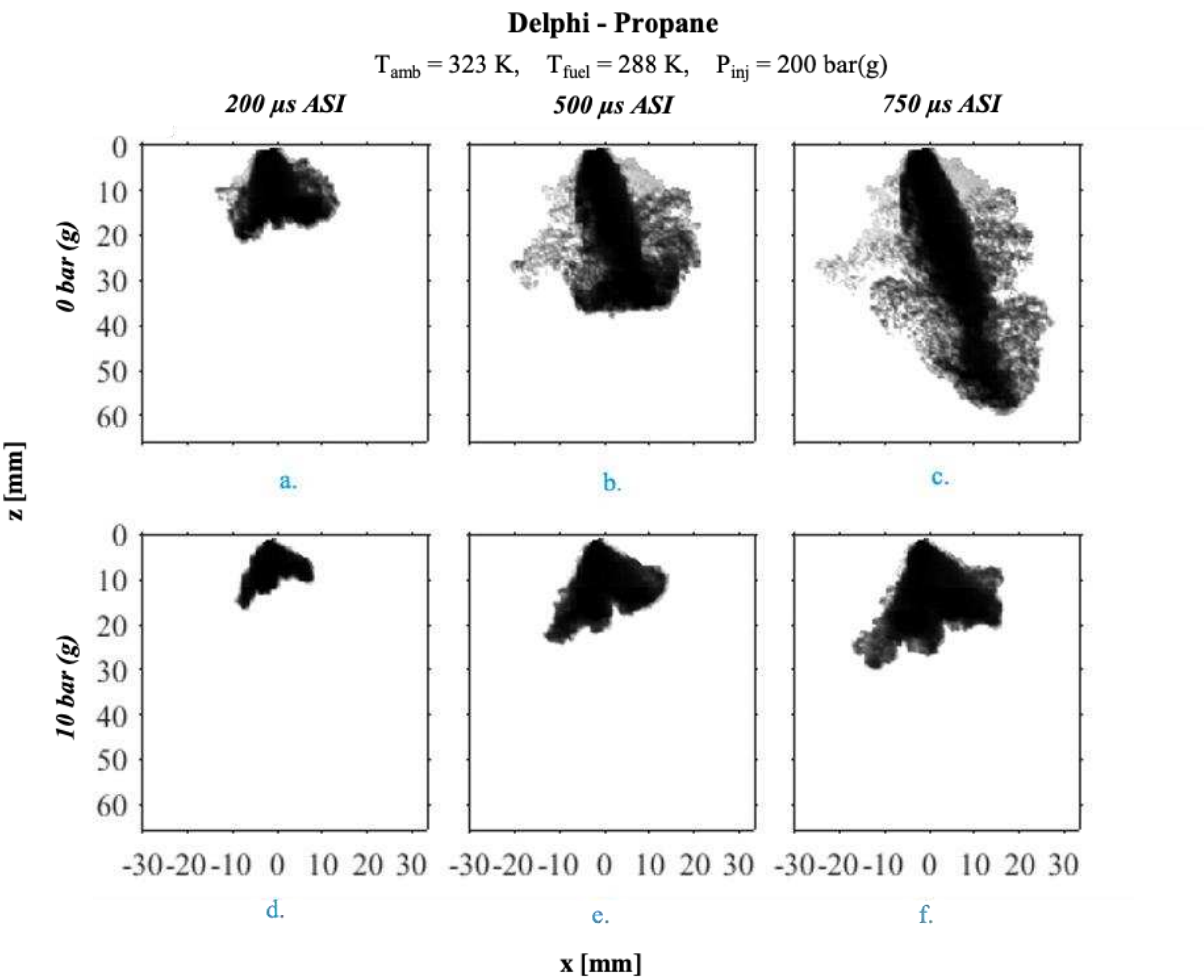

Figure 3-9 High-speed Schlieren images for Delphi injector at various timesteps after the start of injection for propane at various conditions, namely: T_{cvc} = 50 °C, T_{fuel} = 15 °C, P_{fuel} = 200 bar (gage) for (a) - (c) at P_{cvc} = 0 bar (gage) and (d) - (f) at P_{cvc} = 10 bar (gage)

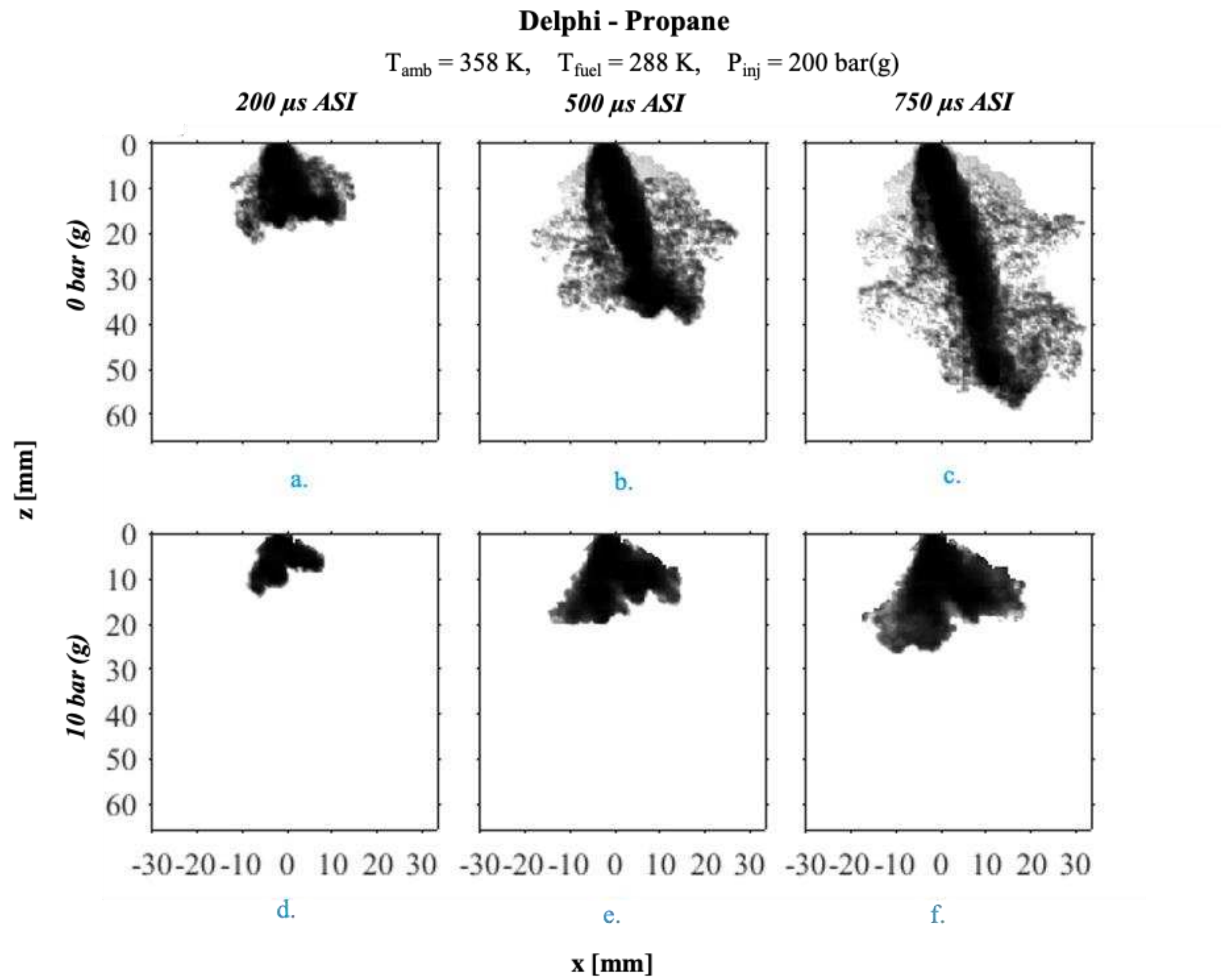

Figure 3-10 High-speed Schlieren images for Delphi injector at various timesteps after the start of injection for propane at various conditions, namely: T_{cvc} = 85 °C, T_{fuel} = 15 °C, P_{fuel} = 200 bar (gage), for (a) - (c) at P_{cvc} = 0 bar (gage) and (d) - (f) at P_{cvc} = 10 bar (gage)

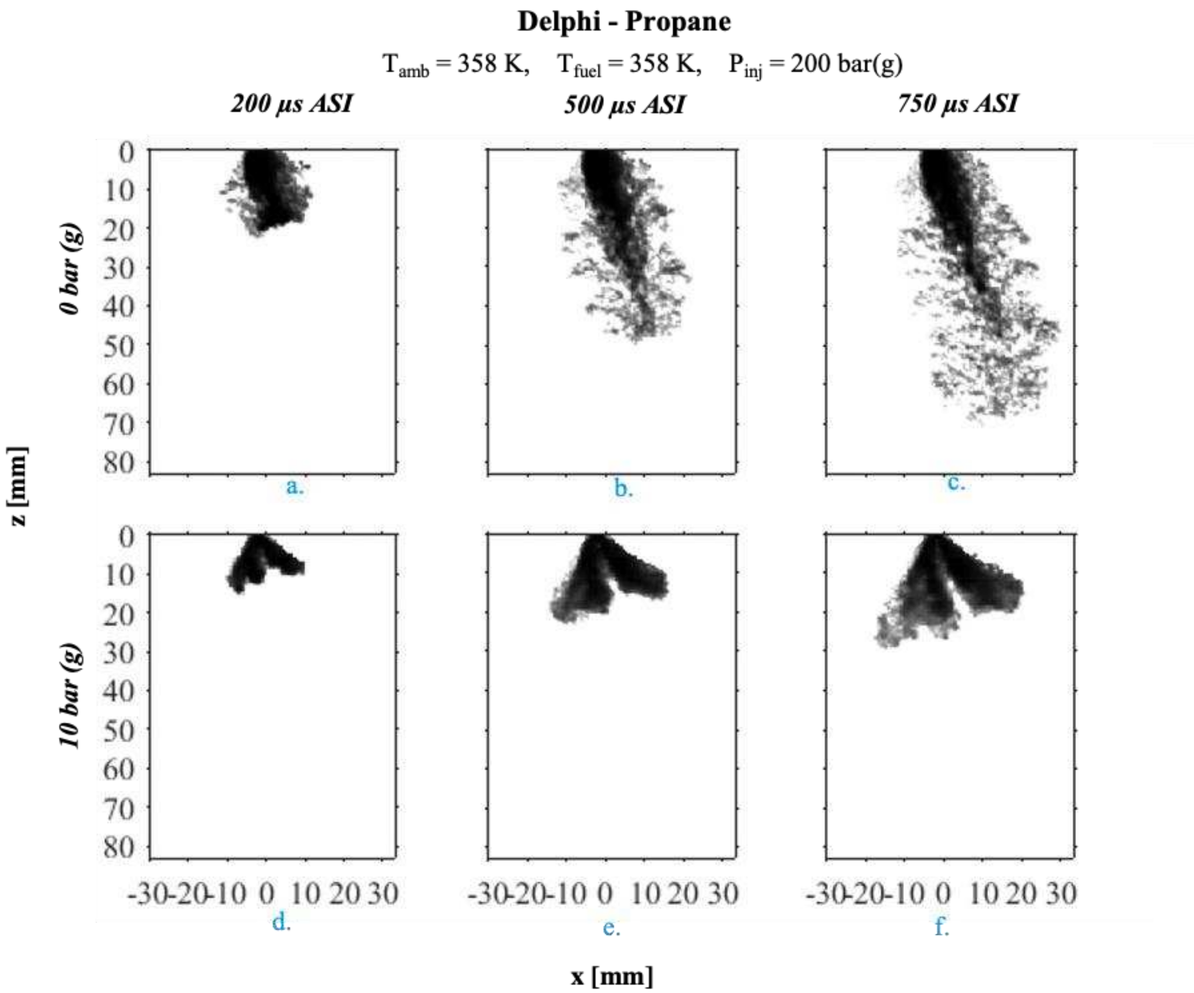

Figure 3-11 High-speed Schlieren images for Delphi injector at various timesteps after the start of injection for propane at various conditions, namely: T_{cvc} = 85 °C, T_{fuel} = 85 °C, P_{fuel} = 200 bar (gage) for (a) - (c) at P_{cvc} = 0 bar (gage) and (d) - (f) at P_{cvc} = 10 bar (gage)

Figures 3-12 (a), 3-13 (a), and 3-14 (a), display maximum vapor penetration lengths for different injection and chamber pressures. Similarly, to the Spray-G results, propane exhibits a much higher penetration length at higher pressures compared to lower pressures. Moreover, it can be observed that at higher temperatures for both the chamber and fuel, propane exhibits an increase in penetration length. These results show that propane has a directly proportional relationship to temperature and an inversely proportional relationship to chamber pressure.

Figures 3-12 (a), 3-13 (a), and 3-14 (a), also presents that, as temperatures are increased for both the chamber and fuel, the difference between low chamber pressure cases (0 bar) and high chamber pressure cases (10 bar) grows larger. Figure 3-10a shows approximately a 50 mm difference at 1200 μs, while in Figure 3-14 (a) there is approximately a 70 mm difference at 1200 μs. Additionally, vapor penetration length measurements demonstrate a directly proportional relationship to injection pressure, and this can be observed across all test conditions. Interestingly, at T_{cvc} = 85 °C and T_{fuel} = 85 °C, both 0 bar and 10 bar cases start to converge at 30 mm and 100 mm at 1200 μs, regardless of injection pressure variations. Similarly, to vapor penetration lengths, vapor penetration widths of propane exhibit a consistent trend of an indirect proportionality to chamber pressure for all cases, as seen in Figures 3-12 (b), 3-13 (b), and 3-14 (b). On the other hand, temperature seems to have a negligible influence on penetration width. There is a good agreement between the qualitative and quantitative results as generally similar trends can be distinguished. When observing vapor penetration speeds, generally 0 bar cases and 10 bar cases have a similar profile over the duration of the spray. There is a sharp decrease in penetration speed initially and then over time the speed begins to fall, to an equilibrium for most cases. It can be observed in Figures 3-12 (c), 3-13 (c), and 3-14 (c), that 0 bar pressure cases, on average, have a larger penetration speed than at 10 bar pressure cases with around a 30 to 40 mm difference over the duration of the spray. Additionally, an obvious correlation is exhibited where injection pressure has a directly proportional relationship to vapor penetration length. Interestingly, at T_{cvc} = 85 °C, T_{fuel} = 85 °C, and P_{cvc} = 0 bar, over all injection pressures display what appears to be a linear decrease in penetration speed, over the time domain of 200 μs to 1200 μs.

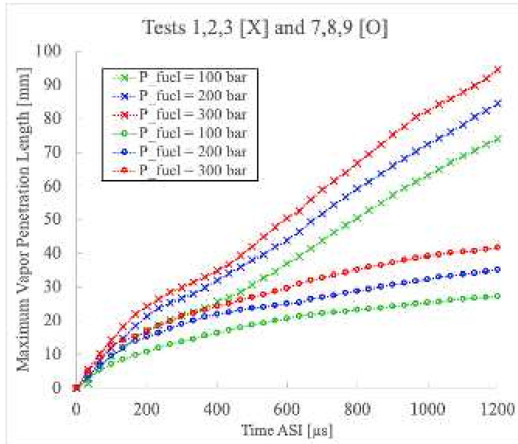

a.

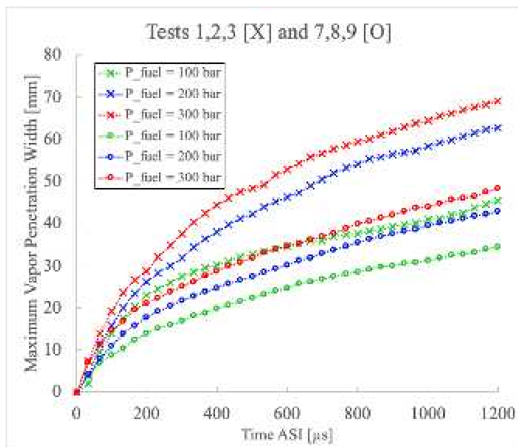

b.

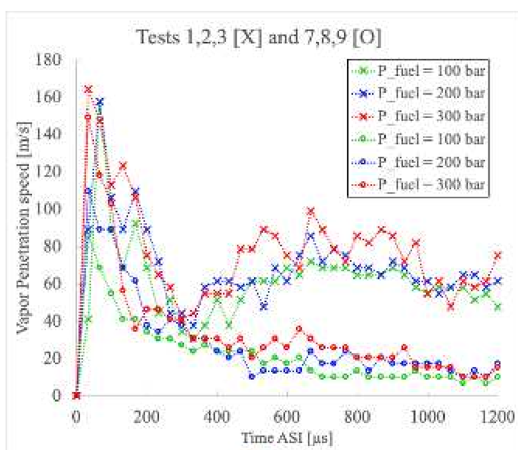

c.

Figure 3-12 Test 1, 2, 3, 7, 8, and 9 represent T_{cvc} = 50 °C, T_{fuel} = 15 °C, and P_{cvc} = 0 & 10 bar (gage) with varying injection pressures (100, 200, 300 bar (gage)) portraying measurements for propane including a) maximum vapor penetration lengths, b) maximum vapor penetration widths, and c) maximum vapor penetration speeds

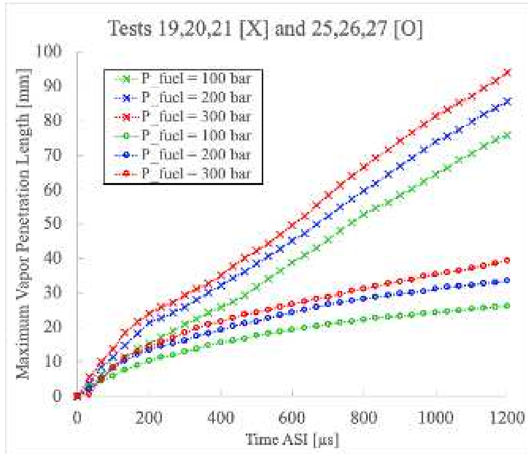

a.

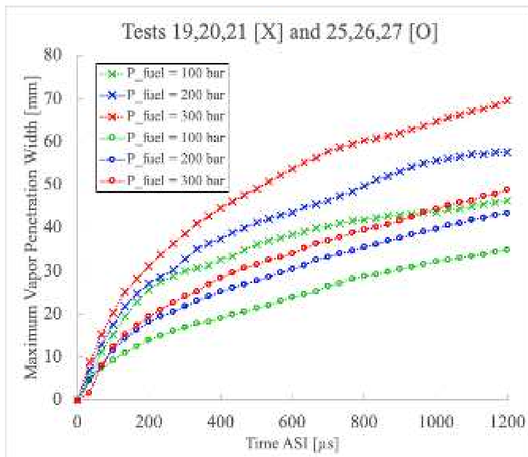

b.

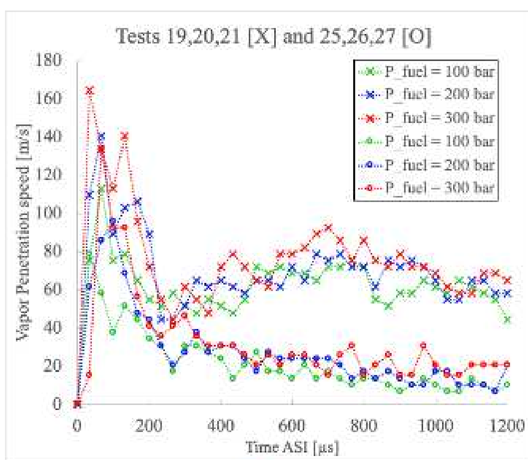

c.

Figure 3-13 Test 19, 20, 21, 25, 26, and 27 represent T_{cvc} = 85 °C, T_{fuel} = 15 °C, and P_{cvc} = 0 & 10 bar (gage) with varying injection pressures (100, 200, 300 bar (gage)) portraying measurements for propane including a) maximum vapor penetration lengths, b) maximum vapor penetration widths, and c) maximum vapor penetration speeds

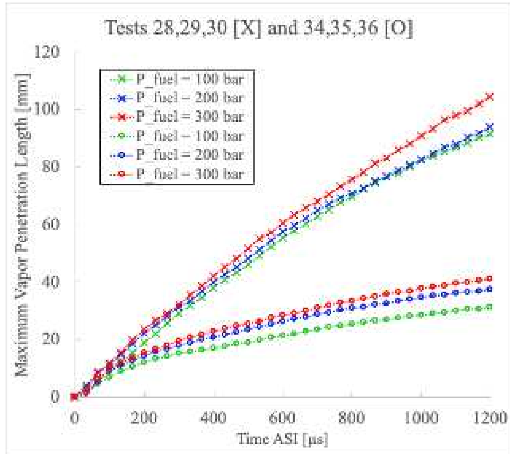

a.

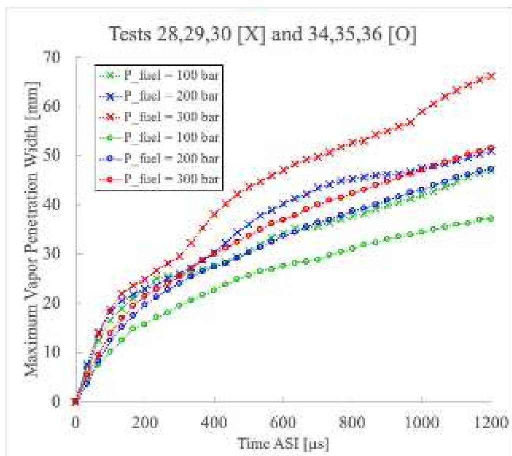

b.

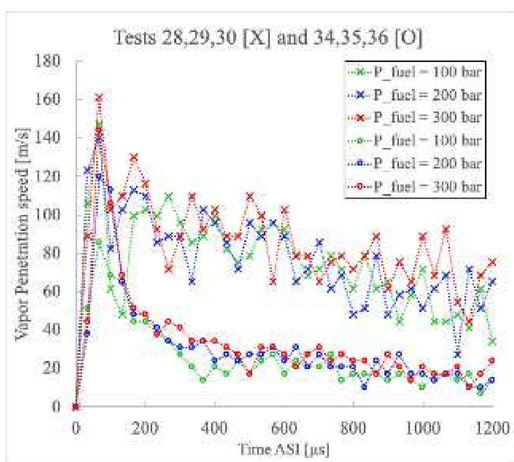

c.

Figure 3-14 Test 28, 29, 30, 34, 35, and 36 represent T_{cvc} = 85 °C, T_{fuel} = 85 °C, and P_{cvc} = 0 & 10 bar (gage) with varying injection pressures (100, 200, 300 bar (gage)) portraying measurements for propane including a) maximum vapor penetration lengths, b) maximum vapor penetration widths, and c) maximum vapor penetration speeds

3.6 Experimental Delphi Planar Mie Scattering Results

Figures 3-15 – 3-17 display planar Mie scattering imaging for the Delphi injector injecting propane at three timestamps of 250, 500, 750 μs for 0 and 10 bar cases. Both temperature and pressure have a large influence on the spray morphology. Observing Figure 3-15 (a-c), or lower pressure cases, a singular liquid jet is seen protruding slightly to the left off the axis of the injector, along with a more dispersed jet expanding to the right of the axis of the injector. The overall liquid core of the Mie images resembles a similar profile to that which is seen in Schlieren images, as seen in Figure 3-9. Likewise, for the higher chamber temperature conditions seen in Figure 3-16 (a-c), a similar liquid profile can be seen when compared to Figure 3-15 (a-c). On the other hand, when observing Figure 3-17 (a-c), the liquid jet to the left of the axis is completely gone, while the more disperse liquid jet to the right of the axis appears to be amplified in brightness. Increases in brightness between these cases, is caused by the attenuation of the laser sheet by the left leading liquid jet as seen in Figures 3-16 (a-c) and 3-17 (a-c), while in Figure 3-18 (a-c) the laser is no longer attenuated by the left leading jet. The difference in spray structure between these conditions is contributed to the increase of temperature in both the fuel and chamber.

Comparing Figure 3-15 (a-c) and 3-15 (d-f), the spray structure is much different as only a singular liquid jet protruding to the left of the injector axis is seen. In addition, in Figures 3-16 (a-c) and 3-17 (a-c), only a singular liquid jet can be seen. This affect is contributed to the rise in chamber pressure. Between Figures 3-15 (a-c), 3-16 (a-c), and 3-17 (a-c), there appears little to no difference between cases, other than at a $T_{cvc} = T_{fuel} = 85$ °C, the liquid core is slightly smaller.

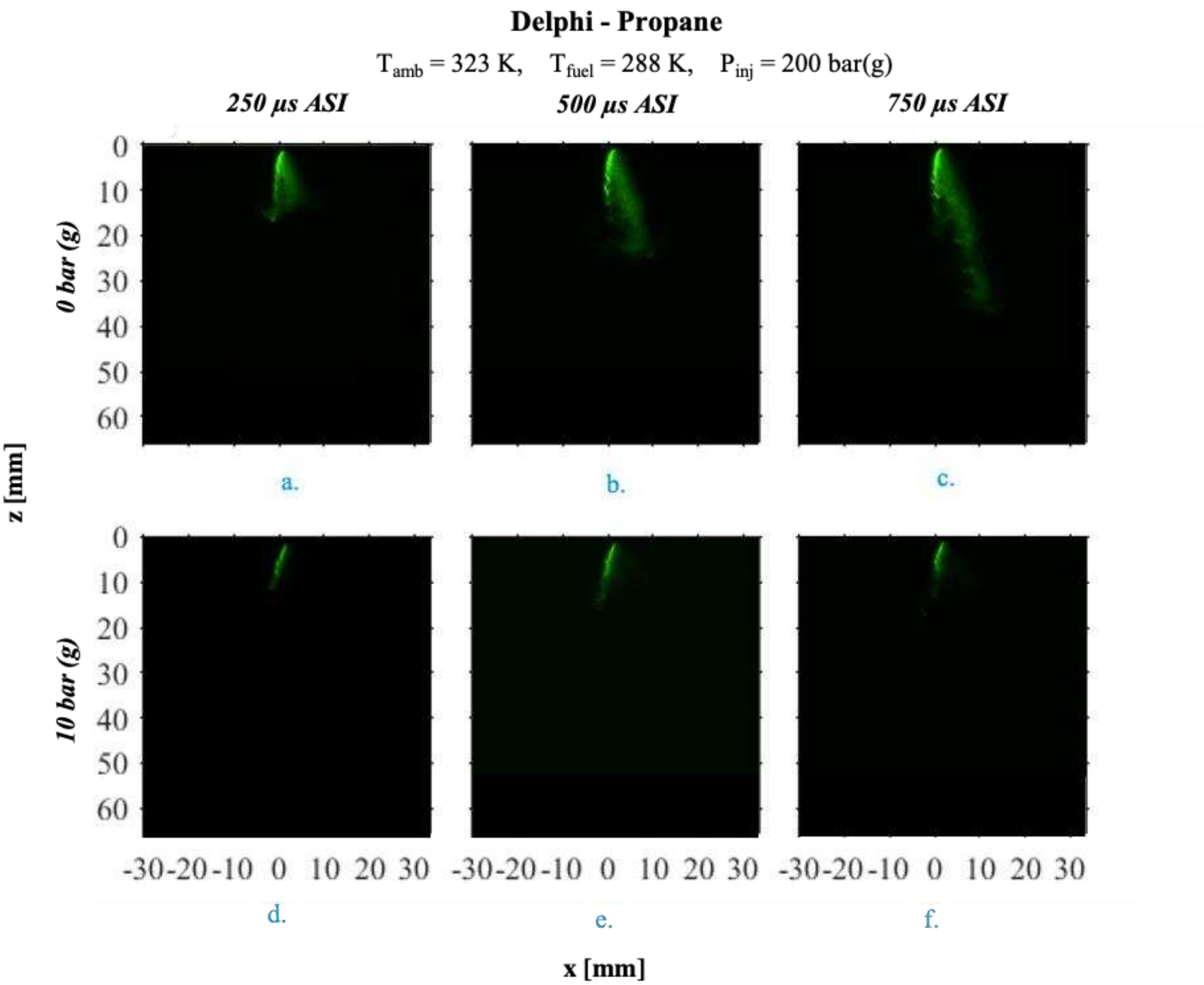

Figure 3-15 Planar Mie images for Delphi injector at 250, 500, and 750 μs after the start of injection for propane at various conditions, namely: T_{cvc} = 50 °C, T_{fuel} = 15 °C, P_{fuel} = 200 bar (gage), (a) - (c) P_{cvc} = 0 bar (gage) and (d) - (f) P_{cvc} = 10 bar (gage)

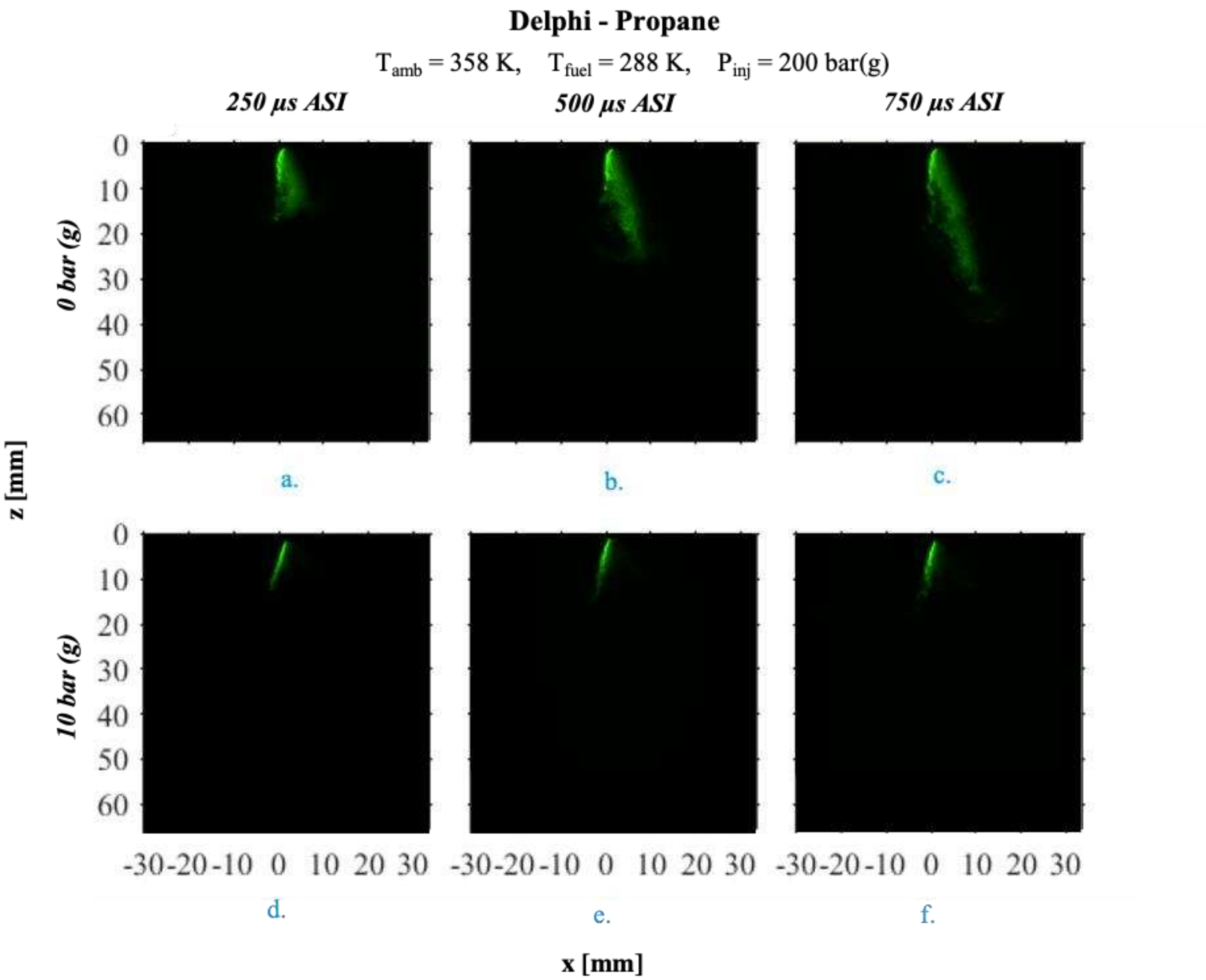

Figure 3-16 Planar Mie images for Delphi injector at 250, 500, and 750 µs after the start of injection for propane at various conditions, namely: T_{cvc} = 85 °C, T_{fuel} = 15 °C, P_{fuel} = 200 bar (gage) for (a) - (c) at P_{cvc} = 0 bar (gage) and (d) - (f) at P_{cvc} = 10 bar (gage)

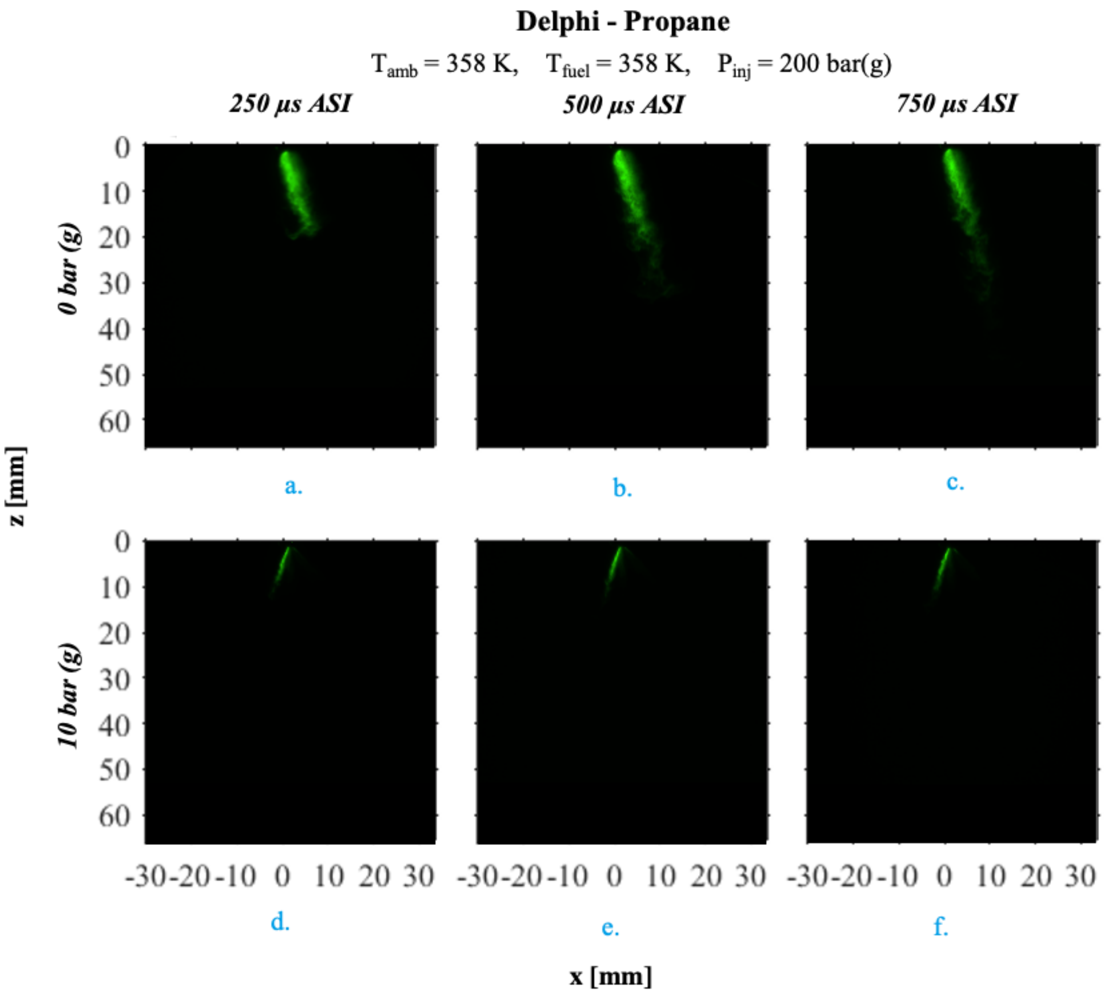

Figure 3-17 Planar Mie images for Delphi injector at 250, 500, and 750 µs after the start of injection for propane at various conditions, namely: T_{cvc} = 85 °C, T_{fuel} = 85 °C, P_{fuel} = 200 bar (gage) for (a) - (c) at P_{cvc} = 0 bar (gage) and (d) - (f) at P_{cvc} = 10 bar (gage)

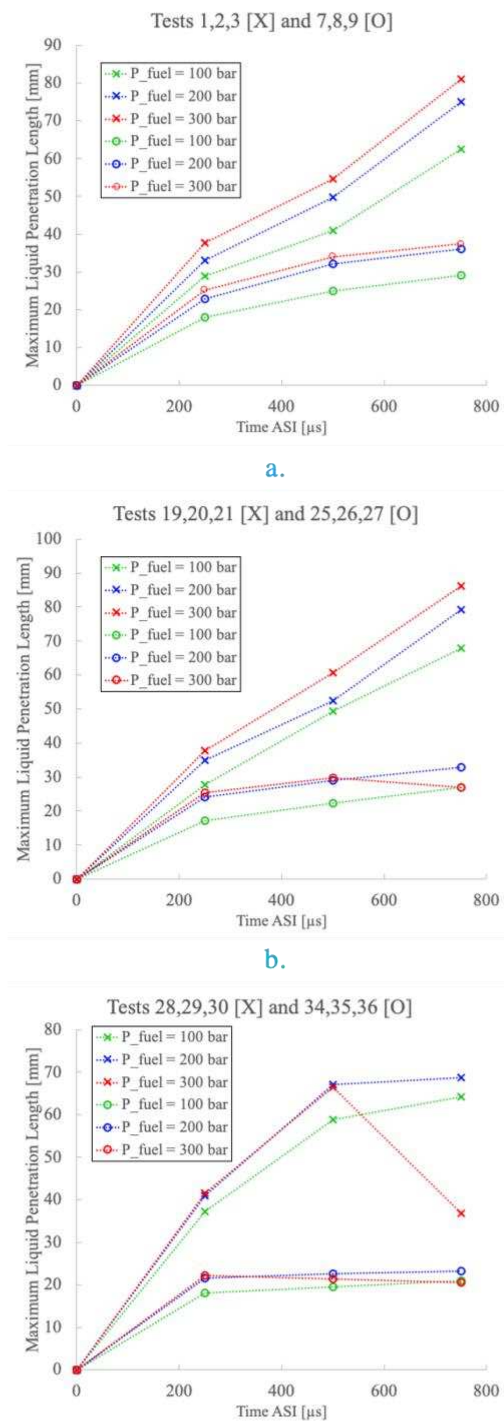

Figure 3-18 Maximum liquid penetration lengths with varying injection pressures (100, 200, 300 bar (gage)) displaying measurements for propane at test conditions a) 1, 2, 3, 7, 8, and 9, b) 19, 20, 21, 25, 26, and 27c) 28, 29, 30, 34, 35, and 36 (missing data point for Test 30) – hand measured calculations with potential of high error

Figure 3-18 displays the maximum liquid penetration length in observed cases. As represented in Figure 3-18 (a), the liquid penetration length at 0 bar conditions is much higher when compared to 10 bar conditions, with an approximate 40 mm difference. Additionally, in Figure 3-18 (a) and 3-18 (b), similar results are observed where lower pressure cases exhibit a larger liquid penetration length than higher pressure conditions. This is evidence that ambient pressure has an inversely proportional relationship to liquid penetration length. Furthermore, for most cases injection pressure appears to have a direct proportional relationship to liquid penetration length. Interestingly, in Figure 3-18 (c), when the temperature of both the fuel and chamber are increased the liquid penetration lengths begin to level out for both 0 and 10 bar cases. This phenomenon is also represented at 10 bar in Figure 3-18 (b). Noteworthy, and represented, in Schlieren vapor penetration lengths, temperature of both the fuel and chamber are increased (Figure 3-18 (a-c)), regardless of injection pressure, both 0 and 10 bar cases appear to begin to converge to a common value.

3.7 Discussion

As seen for both Schlieren and Mie imaging and the Spray-G and Delphi injectors, crucial information from vapor and liquid penetration length, width, and speed measurements are used to define characteristics of the spray morphology. For the Spray-G injector, iso-octane is minimally affected by temperature and pressure as seen in the qualitative and quantitative analysis from Schlieren and Mie imaging. The overall spray morphology and propagation are strongly influenced by the presence of the liquid cores in iso-octane.

The high viscosity, low volatility and higher density of iso-octane compared to propane are considered the main contributing factors. These properties help prolong the existence of the liquid phase of the fuel and produce a conventional spray pattern in iso-octane, i.e., wider spray angles and distinct plumes as observed in Figures 3-3 (a-f) and Figures 3-5 (a-f). This leads to a homogenous mixture both axially and transversely throughout the HPSC for all tested conditions. When comparing planar Mie with Schlieren, there is a clear and consistent relationship for both the liquid and vapor penetration of iso-octane. The observation of distinct plumes can be inferred in the absence of flash boiling effects in iso-octane, due to its low volatility, and high viscosity. Iso-octane does not display extreme flash boiling and collapse, which impacts the overall light intensity when compared to only one illuminated spray plume as shown in Figure 3-6.

Unlike iso-octane for both the Spray-G and Delphi injectors, propane given its' high volatility and low viscosity, experiences severe flash boiling at all tested conditions for both test campaigns. The spray morphology, structure and mixing process are all greatly influenced by severe flash boiling. Figures 3-3 (g-l), displays Schlieren imaging of the Spray-G injector and all eight individual plumes collapse into a singular jet due to the high super-heat degree of propane. Similarly, the Delphi injector in Figures 3-15 (a-c) and 3-16 (a-c), also exhibits intense spray collapse as an additional disperse jet is viewed slightly to the right of the injector axis in Figures 3-15 (a-c) and 3-16 (a-c). Especially in Figure 3-17 (a-c), all seven individual jets collapse into a large singular plume. For the Spray-G injector, propane at colder conditions appears to have some plume-to-plume distinctions, minimal collapse, and wider spray angles, whereas these features are completely absent at hotter conditions. Alternatively, since the Delphi injector was tested at hotter chamber temperatures, similar features compared to the Spray-G injector are seen but, overall flash boiling, and spray collapse are dominant for most cases. Hence, the magnitude of high super-heat degree of propane is strongly dependent on temperature. This affect also impacts the mixing processes of propane, as it transitions from semi-axially dependent mixing at colder conditions to strongly axially dependent mixing at hotter conditions for the Spray-G injector. The Delphi injector exhibits strong axial mixing for most temperature conditions. On the other hand, pressure influences the spray structure. Higher pressures induce semi-axial mixing effects, while at lower pressures there is a strong relationship to axial mixing. Another key feature to note about propane is at tested conditions, the majority of propane's spray propagation is fed by its flash boiling, spray collapse, and high degree of vaporization. This also explains the direct proportionality of propane's penetration length with temperature for the Spray-G injector.

When comparing Mie images for both propane and iso-octane for the Spray-G injector, propane's jet appears to be brighter compared to iso-octane's singular plume. This evidence can be misleading as it might signify presence of more liquid in the cases of propane. This effect is also seen in propane for the Delphi injector ($T_{cvc} = T_{fuel} = 85$ °C) where the overall spray plume seems to be brighter at other temperature conditions. However, it is worth noting that the collected Mie images in Figures 3-6 are for planar Mie, not global Mie. For iso-octane only one nozzle of the injector is contributing to the liquid concentration inside the laser plane. Propane, on the other hand, displays multiple nozzle jets collapses and contribute to its liquid concentration within the plane making it appear brighter. From Schlieren measurements in Figure 3-3 (c), it was also observed that propane's velocity pulsated after the first 100 μs for all conditions. This effect was only seen in propane and can be attributed to the presence of shock structures within the fuel jet and gas-like injection of propane.

Additionally for the Delphi injector, as previously stated, there is a 5° offset applied to the injector holes. This offset is obviously seen in both Schlieren and planar Mie imaging results and contributes to some physical features of the spray. Interestingly, the 5° offset is directing in the opposite direction that most cases appear to be. This potentially is due to a larger mass flow rate of fuel in the opposite direction of the offset, however, without correct geometry measurements and simulated results this phenomenon is not a parameter viewed in this study. All these unique features of propane and its variation from iso-octane's spray pattern, contribute to its classification as an unconventional spray.

Using propane for both the Spray-G and Delphi injectors, it is observed at lower chamber pressures, that all jets collapse to become a large individual single jet that has a much longer penetration length than iso-octane at identical conditions. Ultimately, this individual jet is caused by a few factors such as the saturation vapor pressure, the fuel rail and chamber temperatures, and the expansion of the individual jets. When observing both the Spray-G and Delphi injectors, during low chamber pressure operation, both the fuel and chamber temperatures are high, the fuel exist as a supercritical fluid or compressed fluid in the fuel rail. Once the fuel exits the injector nozzle, the fuel begins to vaporize almost instantaneously, and the rapid expansion of the vapor begins to influence/interfere with the development of the neighboring jets. If this interference of the expanded plume is within the length of the neighboring nozzle holes, then the plumes will begin to combine and form into one singular jet. The rapid vaporization and expansion of the liquid fuel can be defined by Lacey's et al. new pressure ratio, where the expansion of the plume is considered to be choked at the throat of the nozzle and creates an under expanded jet [30]. The expansion of the individual jets is caused by the saturation vapor pressure of propane, where if the chamber pressure is lower than that of the saturation vapor pressure, at the corresponding fuel and chamber temperatures, there is a greater expansion of the fuel when exiting the nozzle. This phenomenon is also known as flash boiling.

The large individual jet is a combination of flash boiling, where plumes are drawn towards each other, and a shielding effect is created by the edges of the plumes. When the plumes expand, once exiting the nozzle, the plumes begin to interfere with each other where the center of the combined plumes have a similar axial vapor penetration speed. While the edges of the plumes are creating a shielding effect where the edges have a slower penetration speed, they enable the core to continue to have a faster penetration speed. These phenomena, help produce the common large individual jet plume (tube like shape) seen at lower chamber pressures and higher fuel and chamber temperatures. When observing propane spray at higher chamber pressures, the spray morphology begins to resemble that of iso-octane's conventional spray definition. At higher chamber pressures, individual plumes expand less than at lower chamber pressures. While each plume is expanding less than at lower pressure conditions, the plumes do not interfere/interact with each other aggressively, and spray collapse is not observed. Additionally, while flash boiling is still present at these conditions, the small amount of vapor interaction between plumes is not enough to generate spray collapse.

In Figure 3-19, both high and low pressure cases are represented, showing the extreme temperatures that would also be seen for these cases. The low pressure – high temperature case can be observed which is represented by the blue trajectory line, where the fuel is seen existing as compressible liquid, then transitioning into a liquid, and then into a vapor phase. The lower pressure – higher temperature case would be representative of strong plume-to-plume interaction occurring due to the expansion of the jets at the nozzle, which would then lead into spray collapse, due to transitioning across the saturation vapor pressure line. The higher pressure –

lower temperature case is represented by the green trajectory line, which similarly, exists as a compressible liquid, transitioning into a liquid, and then a vapor. The high pressure case shows that a high chamber pressure greatly influences the spray morphology, due to propane's saturation pressure, where the fuel spends less time in the vapor region. Additionally, a higher temperature of the fuel and the chamber, consequently, increases the saturation pressure. With a higher saturation pressure, the spray morphology is greatly influenced.

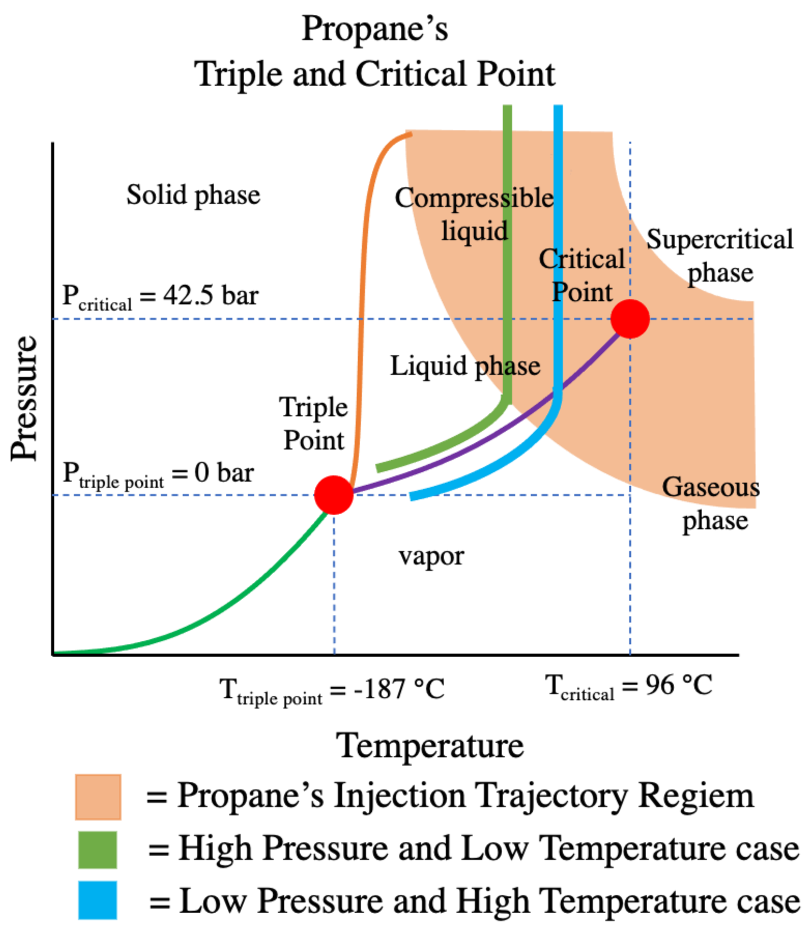

Figure 3-19 Propane's triple point and critical point plot. Displaying possible regimes where propane would exist at engine like conditions. Propane's vapor pressure is 9.25 bar,135 psi @25 °C. Also displaying a high pressure and low temperature trajectory line (green) and a low pressure and high temperature trajectory line (blue)

Chapter 4 - Numerical Results and Comparisons

4.1 Introduction

All simulation results were solely modeled and produced by Lorenzo Nocivelli and Katherine Aszalos at Argonne National Laboratory and they have generously provided results as a comparison to experimental studies.

4.1.1 Lagrangian Spray Simulation Results for Spray-G Injector

The Lagrangian spray simulations in this work, presents preliminary results from an effort to define a computational framework capable of reproducing the behavior of propane sprays at engine-like conditions for the Spray-G injector [64]. The focus of this simulation campaign is to capture fuel development in the HPSC, which will be validated against optimal experimental measurements. Three conditions have been simulated: (i) G3 with iso-octane, (ii) G3C with propane, and (iii) G3 with propane. The results are qualitatively compared with experimental results from the HPSC obtained through Schlieren and Mie scattering imaging techniques. The numerical results are compared with the experimental data in terms of spray morphology and axial penetration lengths. The setup for the injection of iso-octane at G3 conditions is based on the previous work by Nocivelli et al. and re-processed to replicate Schlieren and Mie scattering images [62].

Vaporization-driven collapse is represented by enlarging the initial cone angle (C_A) of the blob injector to 40°, while keeping the inclusion angle (I_A) consistent with the nominal geometry of the nozzle i.e., 37°. The I_A and the C_A, are defined by the deviation from the injector axis for a singular nozzle. Both I_A and the C_A, influence the spray morphology, axial penetration lengths, as well as potentially influencing the spray breakup and atomization at different conditions. The simulation results for propane were found to be sensitive to both the I_A and the nominal direction of the nozzles.

The influence of C_A and I_A on the spray morphology indicates spray collapse is promoted as C_A is increased. By further investigating the breakup model, noticeable differences in the spray morphology become apparent. When comparing experimental Schlieren vapor penetration lengths and widths, an I_A of 37° and C_A of 40° were found to accurately model the penetration profile of propane at both G3C and G3 conditions. The final geometry modeling decisions made for the blob injector at G3C and G3 conditions are shown in Figures 4-1(b) and 4-2(c), respectively.

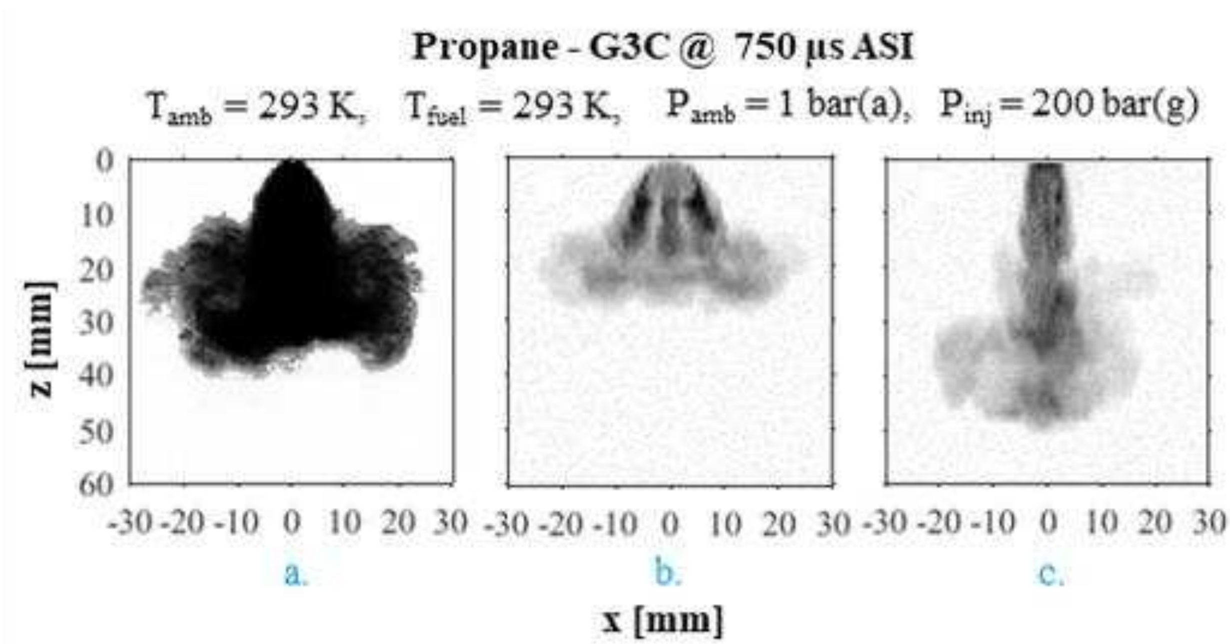

Figure 4-1 (a) Spray-G experimental Schlieren image of propane at G3C; projected density gradient of the gas phase from Lagrangian spray simulations (simulated Schlieren) of injection of propane at G3C conditions modeled with Rayleigh-Taylor breakup time and model size constants corresponding to (b) non-extreme flashing conditions, and (c) extreme flashing conditions. Final modeling decisions made for G3C conditions shown in (b).

Additionally, to I_A and C_A providing a better representation of spray morphology, by considering the KH model time and model size constants for the Rayleigh-Taylor (RT) model, improvements can be made to capture a more accurate spray model [65]. Extreme flashing conditions are simulated by decreasing the model breakup time constant from 1.0 (corresponding to non-extreme flashing conditions) to 0.1, and by decreasing the model size constant from 0.6 (corresponding to non-extreme flashing conditions) to 0.25.

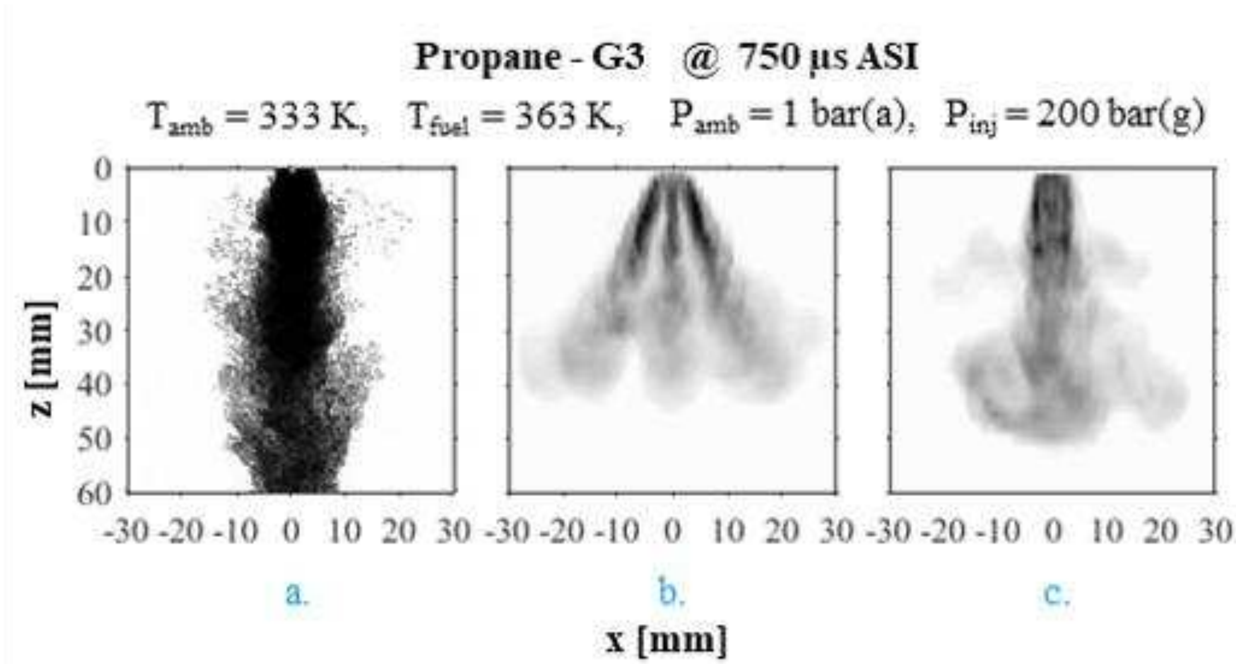

Figure 4-2 (a) Spray-G experimental Schlieren image of propane at G3; projected density gradient of the gas phase from Lagrangian spray simulations (simulated Schlieren) of injection of propane at G3 conditions modeled with Rayleigh-Taylor breakup time and model size constants corresponding to (b) non-extreme flashing conditions, and (c) extreme flashing conditions. Final modeling decisions made for G3 conditions shown in (c).

In particular, two conditions were simulated: (i) parameters corresponding to conditions without extreme flashing, and (ii) with extreme flashing. Figures 4-1 and 4-2, represent results for propane injected at G3C and G3 conditions, respectively. For G3 conditions, extreme flashing improved the overall spray morphology mimicking results like the experimental results as seen in Figure 4-6(a). At G3C conditions, improvement in terms of comparable morphology of the Lagrangian spray was observed. Experimental results achieved parameters corresponding to non-extreme flashing conditions, most notably in the spray collapse and the maximum spray penetration. For the different conditions simulated, the chosen setup is given by Figure 4-1(b) for G3C, and Figure 4-2(c) for G3. The differences in modeling parameters are due to the different spray morphologies observed for the two conditions simulated. The model breakup effect is quite strong for higher temperatures. During G3 conditions, it is necessary to account for rapid vaporization of small droplets, and modeling parameters corresponding to extreme flashing, to capture these effects. For lower temperature conditions, i.e., G3C, the vaporization rate is lower and does not drive morphology as acutely, and the model breakup effect is less dominant.

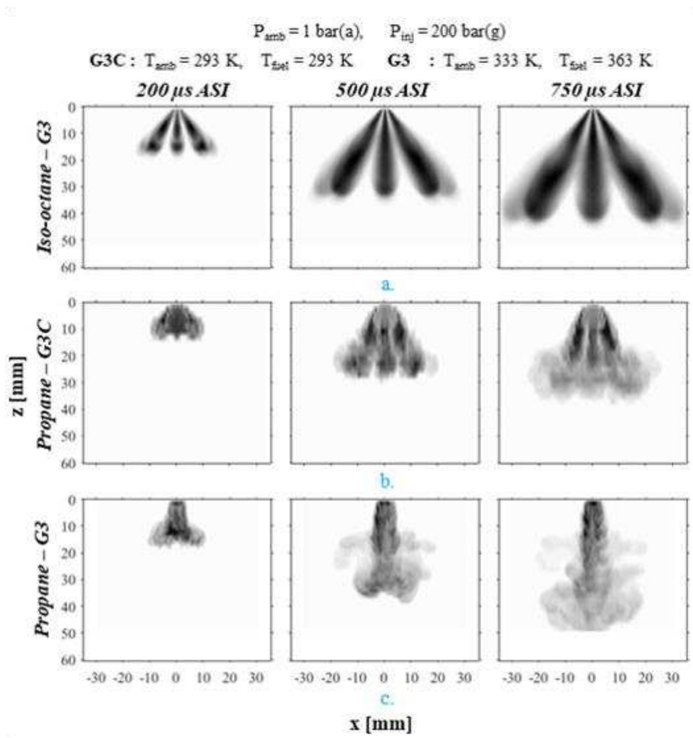

Figure 4-3 Spray-G injector projected density gradients of the gas phase from Lagrangian spray simulations (simulated Schlieren) for (a) iso-octane at G3, (b) propane at G3C, and (c) propane at G3 condition at denoted timestamps.

Figure 4-3 displays three different conditions for iso-octane and propane at 200 μs ASI, 500 μs ASI and 750 μs ASI. These images portray the projected gradients of the gaseous phase density in the Eulerian domain, which includes both fuel vapor and ambient N_2.

For both G3C and G3 conditions, propane displays a strong plume-to-plume interaction and complete collapse of the spray around the axis of the injector. This behavior is directly correlated to the temperature of the fuel and its corresponding vaporization propensity, when propane is injected into a chamber at ambient conditions. At G3C conditions, the vaporization rate of the fuel decreases due to the lower vapor pressure and the reduced thermal energy available in the chamber. The collapse is less abrupt, and the axial velocity of the resulting vapor jet is lower, generating a wider and shorter spray.

Figure 4-8 displays both the experimental and numerical vapor penetration lengths. Numerical results were calculated from the maximum axial distance from the injector location. The gradient portraying these measurements was normalized to binarize the images, which convey that propane is under predicted at G3C and G3 conditions (Figure 4-8b). The discrepancy between these experimental and numerical results, is attributed to the lack of a dedicated flash-boiling model for the parcels and a simplified injector model when used with propane.

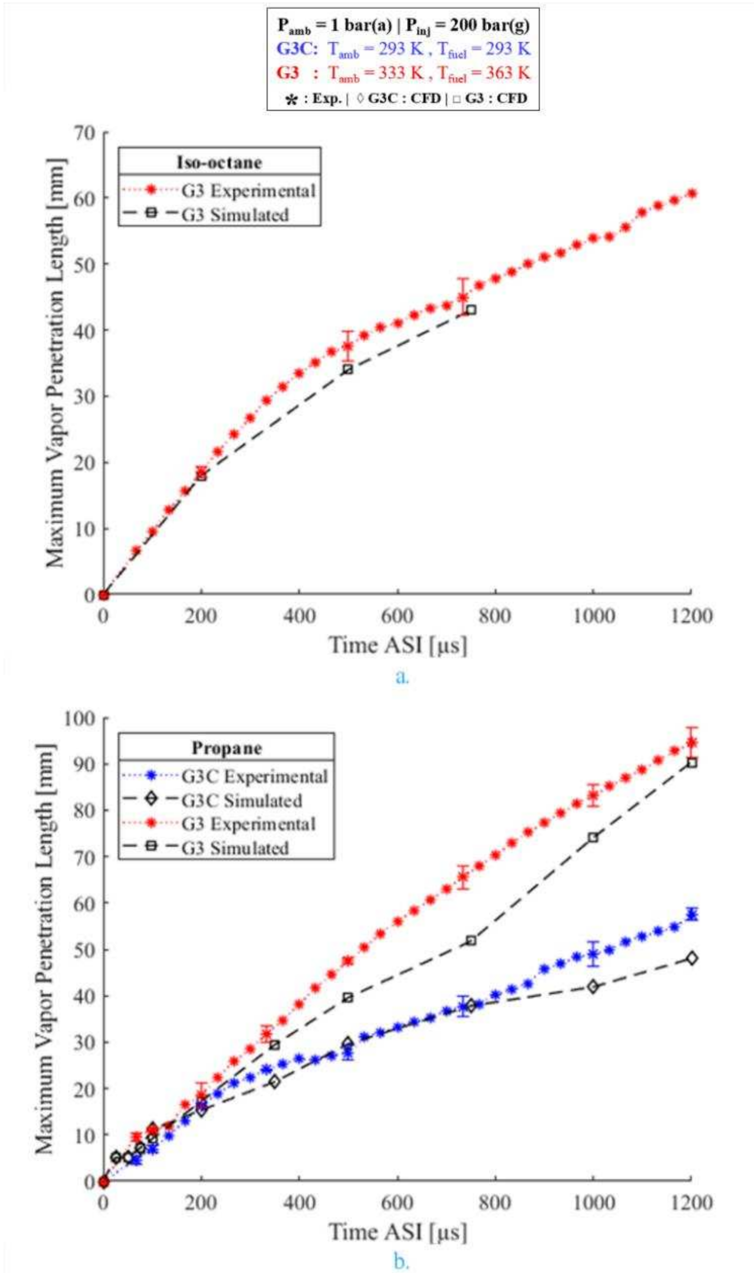

Figure 4-4 Comparison for the Spray-G injector between the experimental results of maximum axial vapor penetration for high-speed Schlieren imaging and computational results from projected density gradient of gas phase from Lagrangian spray simulations (simulated Schlieren) of (a) iso-octane at G3, and (b) propane at G3C and G3 conditions.

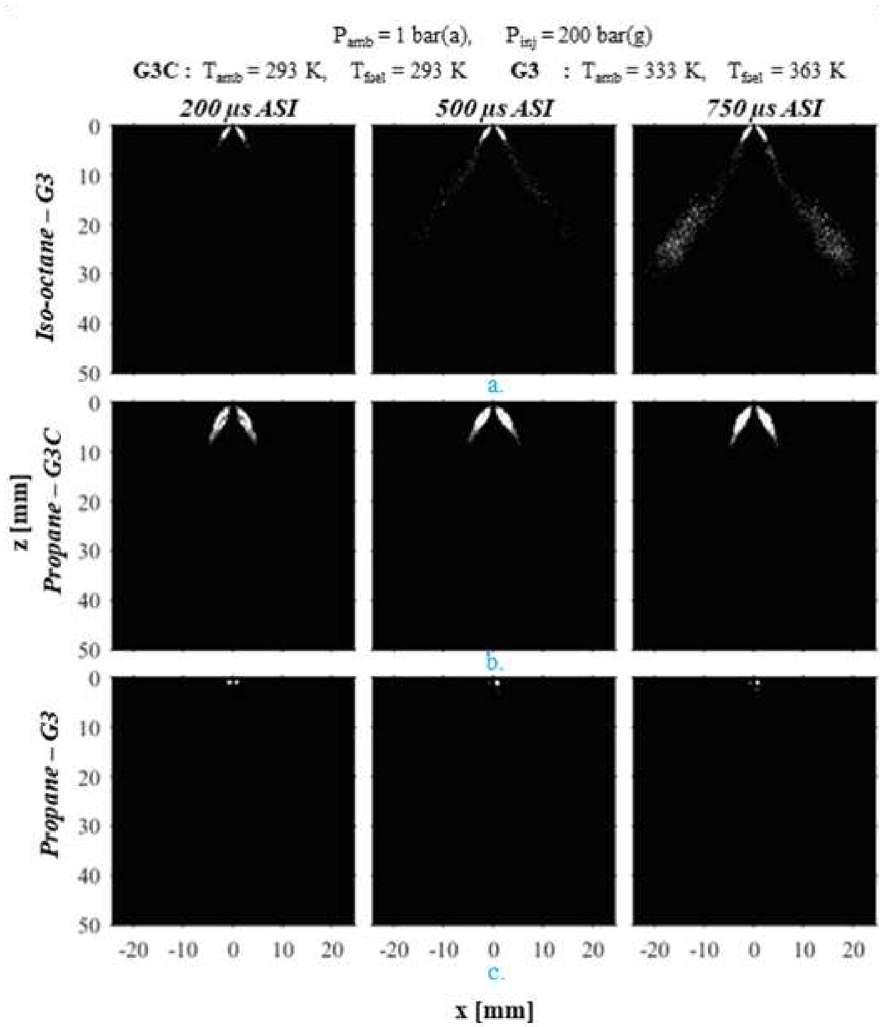

Figure 4-5 Projected density gradient over the line-of-sight of the liquid phase from Lagrangian spray simulations for the volume of the laser sheet (simulated planar Mie) of injection of (a) iso-octane at G3, (b) propane at G3C, and (c) propane at G3 conditions at denoted timestamps.

Figure 4-5 displays a lack of accuracy in the simulation imaging when compared to experimental planar Mie scattering results as shown in Figure 3-4. Notable highlights of the simulation imaging show that phase-change trends are not consistent. In Figure 4-3 the penetration of the liquid parcels is strongly correlated to the density gradients in the gas phase at low-vaporization conditions, such as iso-octane at G3 conditions. Contrary to iso-octane, propane at super-heated conditions such as G3, vaporization is almost instantaneous, which also differs from the collapse spray core seen in the experimental results. These results underline the lack of accuracy of the Lagrangian spray models in representing vaporizing sprays.

The results presented above represent a first assessment for the Spray-G injector. Commonly available models for engine-spray simulations, highlight the fact, that despite the reasonable agreement obtained in the fuel vapor morphology, the representation of the liquid phase lacks accuracy. In addition, the flash-boiling vaporization terms on the phase-change modeling, further reduces the liquid penetration without improving the representation of the vapor dynamics. Propane at both G3C and G3 conditions are considered to be extreme flashing conditions, with a super-heat degree defined as P_{amb}/P_{sat} (T_{fuel}) – (0.12 and 0.03 for G3C and G3, respectively), the empirical correlation tends to over-estimate the phase-change of the fuel.

4.1.2 Lagrangian Spray Simulation Results for Delphi Injector

Additionally, to the Spray-G simulation campaign, additional testing was conducted for the Delphi injector. As previously stated, the geometry provided was incorrect and the true nozzle sizes were unknown. Because of this reason, only one condition was simulated as a full simulation campaign would have wasted time and resources. The condition simulated had a T_{fuel} =15 °C, T_{cvc} = 50 °C, P_{fuel} = 300 bar, P_{cvc} = 10 bar (gage) for propane. Similarly, to the Spray-G campaign, this Delphi injector simulation utilized model constants in the KH-RT model, which either promote flashing or non-extreme flashing conditions. Figure 4-6 shows simulated Schlieren results for propane, at 200 μs ASI, 500 μs ASI, and 750 μs ASI. These images display the projected gradients of the gaseous phase density in the Eulerian domain, including both fuel vapor and ambient N_2 within the environment.

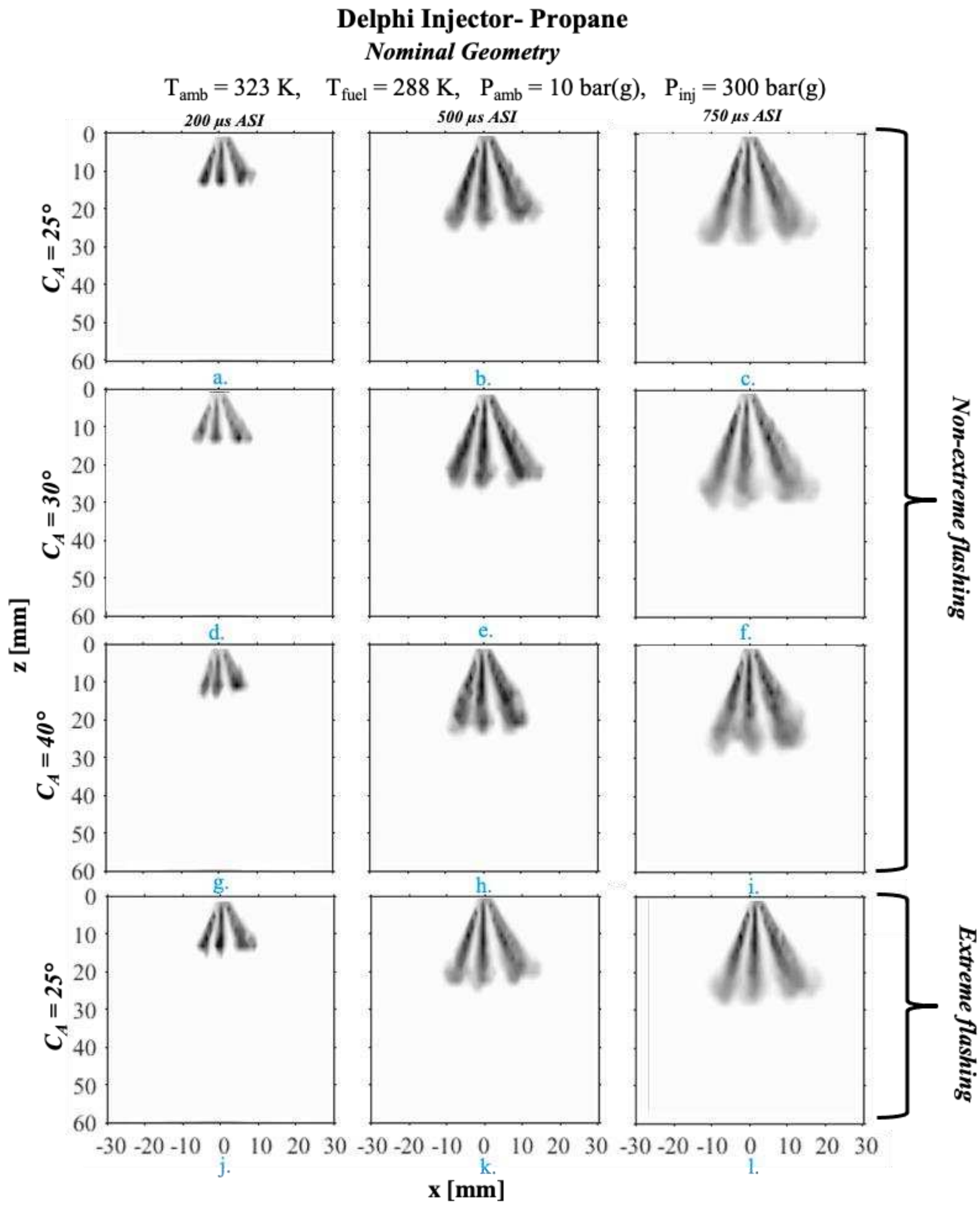

Figure 4-6 Delphi injector projected density gradients of the gas phase from Lagrangian spray simulations of non-extreme flashing conditions (simulated Schlieren) for (a-c) $C_A = 25°$, (d-f) $C_A = 30°$, (g-i) $C_A = 40°$, and extreme flashing conditions for (j-l) $C_A = 25°$

Since the nozzle geometry was not accurate, but the only reference for the nozzle were these measurements, the inclusion angle was fixed to the internal geometry that was provided. In

Figure 4-6, the C_A was the parameter that was changed between 25°, 30°, and 40° to accurately model the spray morphology for non-extreme flashing and extreme flashing conditions. To note again, since the geometry of the injector provided was inaccurate, these results are not tuned by any experimental results and portray a dry run of the simulation and at the time were considered "best-fit" results. The non-extreme flashing conditions reveal that the breakup characteristics have minimal effect due to low vaporization propensity. Also, the increase in the spray surface caused by the breakup does not disrupt the spray. Additionally, the increase in cone angle for non-extreme flashing conditions, promotes some plume-to-plume interactions. Furthermore, some plume-to-plume interaction can be seen at a lower cone angle for extreme flashing conditions. Further, the 5°offset is apparent in these simulated cases, although the effects of the offset are not as extreme when compared to experimental Schlieren imaging.

Figure 4-7 displays simulated planar Mie scattering results for timestamps of 200 µs ASI, 500 µs ASI, and 750 µs ASI. Although these images closely relate the experimental planar Mie imaging shown in Figures 3-13, 3-14, and 3-15, given its geometry, accurate representations of the vaporizing fuel are not a good predictor of the spray morphology. However, a similar liquid core can be seen in both experimental and numerical results. It is observed that the length and shape of the liquid core are influenced by the change of the cone angle. Contrary to cases seen in Figure 4-11(j-k), the extreme flashing conditions accelerate vaporization only exposing a small liquid core towards the tip of the nozzle. Additionally, the 5° offset is not as apparent in the simulated Mie cases compared to simulated Schlieren cases.

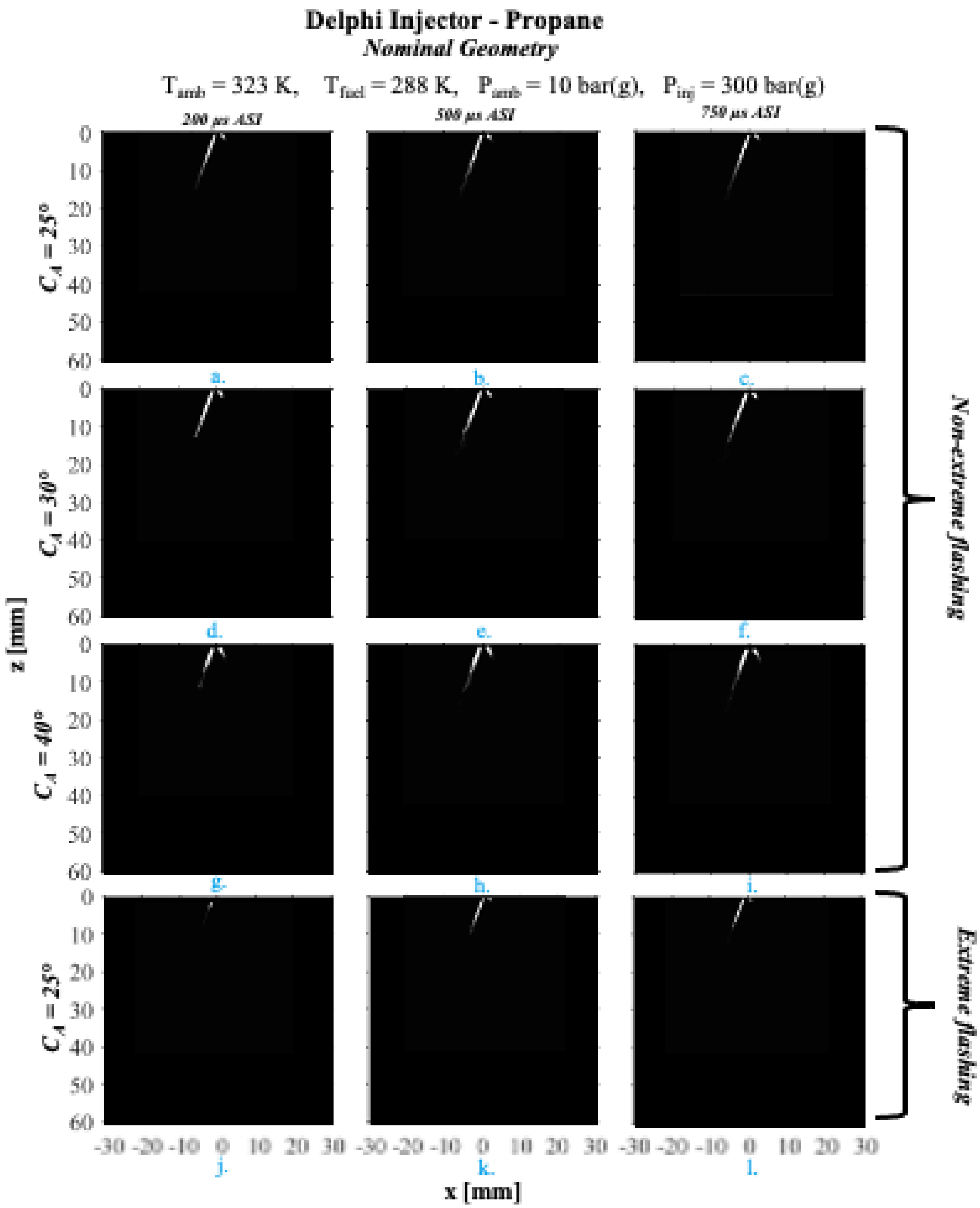

Figure 4-7 Delphi injector projected density gradients over the line-of-sight of the liquid phase from Lagrangian spray simulations for the volume of the laser sheet (simulated planar Mie) for (a-c) $C_A = 25°$, (d-f) $C_A = 30°$, (g-i) $C_A = 40°$, and extreme flashing conditions for (j-l) $C_A = 25°$

Chapter 5 - Conclusions

Heavy duty on-road vehicles transport roughly 72.5% of the nation's freight by weight. Within the transportation sector, 36.5 billion gallons of diesel were consumed and around a quarter of GHG emissions were produced in 2019 by heavy duty vehicles. LPG used in DISI engine platforms utilizing advanced combustion techniques has the potential to reduce emissions while achieving high thermal efficiencies comparable to that of a diesel engine. To support development of high efficiency LPG engines, improved modeling of the spray process was achieved with the aid of detailed spray morphology data to help validate and tune the simulations. This study covers the development of a HPSC capable of mimicking engine-like conditions where two GDI fuel injectors (Spray-G and Delphi) using iso-octane and propane as surrogates for gasoline and LPG, respectively, were deployed to characterize spray morphological features. Two imaging techniques were utilized: high-speed Schlieren and planar Mie scattering imaging which provided detailed information regarding both vapor and liquid penetration length, width, and speed measurements. These measurements provided qualitative and quantitative results that were incorporated into the numerical simulations for model validation, selection, and tuning. Key conclusions from this work are as follows:

- Iso-octane and its' spray structure were minimally affected by temperature and pressure. Iso-octane exhibits a conventional spray pattern with wide spray angles and distinct plume-to-plume features. Additionally, Iso-octane's penetration lengths were inversely proportional to both temperature and pressure.

- Propane exhibited a strong dependence on temperature as severe flash boiling, spray collapse, and high degree of vaporization produced a large singular spray jet for most cases observed. It was also observed that propane's penetration length had a directly proportional relationship to temperature. Given propane's unique physical characteristics compared to iso-octane, adds to its' contribution of classifying propane as an unconventional spray.
- The simulations were based on a Lagrangian spray framework, and the characteristics of the injected droplets were modified according to higher-resolution multi-phase nozzle flow results. The simulated results for the Spray-G injector were found to be sensitive to cone angle and inclusion angles of the blob injector. Final selections for C_A and I_A were chosen by comparing the experimental results that provided a good representation of the spray morphology although there was lack of accuracy for representation of the liquid phase.

The presented work represents a preliminary assessment of the capabilities of both experimental and numerical models and their efforts in aiding and identifying an optimal DI nozzle geometry for a homogenous and stratified charge mixture. With pinpointing the right coupling between timed injection events, in-cylinder motion, and accurate spray models will serve to the overarching goal of achieving near diesel engine efficiency for a Cummins X-15 heavy-duty diesel engine using LPG.

5.1 Future Work

Moving forward, additional optical imaging techniques such as, planar laser induced fluorescence (PLIF) simultaneously used with planar Mie scattering imaging would provide a higher resolution and further insight into the vapor and liquid regions of propane. As seen in Figure 5-1, a PLIF schematic is seen, displaying the simultaneous capabilities of both Mie scattering imaging and PLIF imaging.

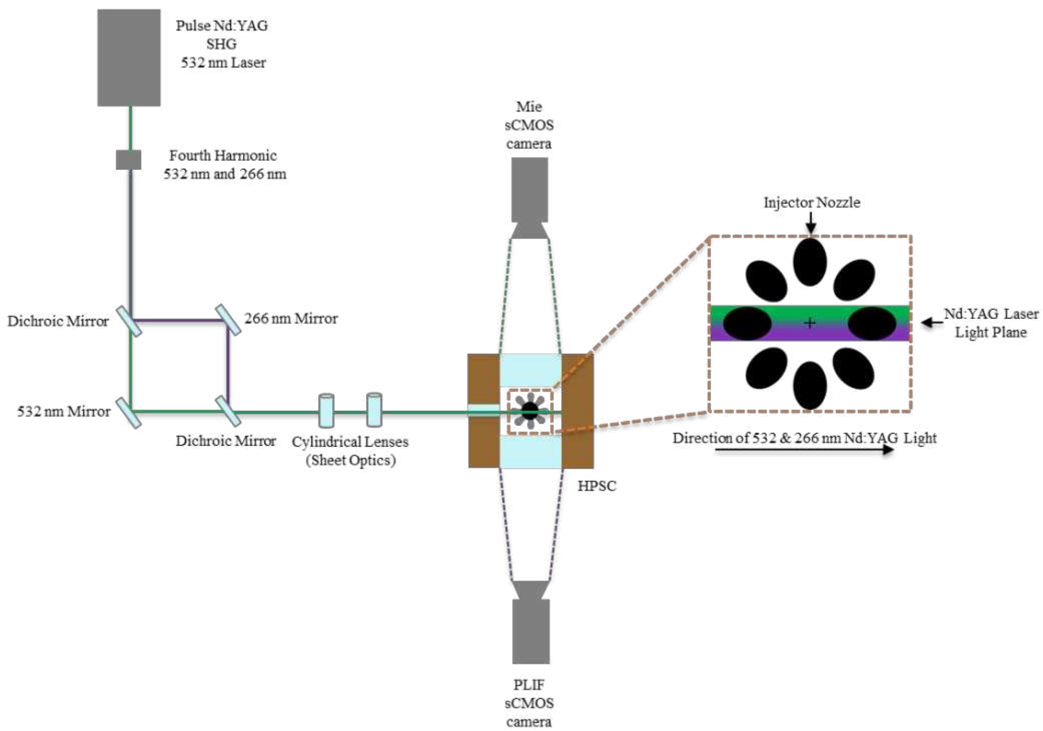

Figure 5-1 Planar laser induced fluorescence (PLIF) top-view schematic

Additionally, higher ambient pressure conditions would benefit the overall dataset. This would offer more insight into, high load, homogenous charge, early injection conditions and part load, stratified charge, late injection conditions often seen in DISI engines using various commercially available and modified GDI nozzle geometries.

Utilizing a computational framework that accommodates high-resolution nozzle flow simulations, such as vapor formation, in the nozzle, droplet size distribution, and detailed multi-phase flow momentum initialization, would benefit further research. Moreover, since flash-boiling is a dominant characteristic in propane spray, detailed modeling of the phase-change should be addressed to predict LPG and its' liquid injection. Finally, CFD results are to be improved including the fuel dependency on the scattered light and possible dense fuel vapor effects to allow for more meaningful comparison to experimental data.

Bibliography

[1] P. Zhai *et al.*, “IPCC, 2021: Climate Change 2021: The Physical Science Basis. Contribution of Working Group I to the Sixth Assessment Report of the Intergovernmental Panel on Climate Change,” *Cambridge University Press. In Press.*, 2021, Accessed: Mar. 14, 2022. [Online]. Available: https://www.ipcc.ch/

[2] “FACT SHEET: President Biden Sets 2030 Greenhouse Gas Pollution Reduction Target Aimed at Creating Good-Paying Union Jobs and Securing U.S. Leadership on Clean Energy Technologies | The White House.” https://www.whitehouse.gov/briefing-room/statements-releases/2021/04/22/fact-sheet-president-biden-sets-2030-greenhouse-gas-pollution-reduction-target-aimed-at-creating-good-paying-union-jobs-and-securing-u-s-leadership-on-clean-energy-technologies/ (accessed Dec. 26, 2021).

[3] J. Li *et al.*, “Toward Low-Cost, High-Energy Density, and High-Power Density Lithium-Ion Batteries,” *JOM 2017 69:9*, vol. 69, no. 9, pp. 1484–1496, Jun. 2017, doi: 10.1007/S11837-017-2404-9.

[4] K. Kim, J. Kim, S. Oh, C. Kim, and Y. Lee, “Evaluation of injection and ignition schemes for the ultra-lean combustion direct-injection LPG engine to control particulate emissions,” *Applied Energy*, vol. 194, pp. 123–135, 2017, doi: 10.1016/j.apenergy.2017.03.012.

[5] “Economics and Industry Data | American Trucking Associations.” https://www.trucking.org/economics-and-industry-data (accessed Feb. 26, 2022).

[6] “Fast Facts on Transportation Greenhouse Gas Emissions | US EPA,” *United State Enviormental Protection Agency*, 2019. https://www.epa.gov/greenvehicles/fast-facts-transportation-greenhouse-gas-emissions (accessed Feb. 27, 2022).

[7] Q. Xin, “The analytical design process and diesel engine system design,” *Diesel Engine System Design*, pp. 3–112, 2013, doi: 10.1533/9780857090836.1.3.

[8] Y. Zhang, D. Lou, P. Tan, Z. Hu, and L. Fang, “Effect of SCR downsizing and ammonia slip catalyst coating on the emissions from a heavy-duty diesel engine,” *Energy Reports*, vol. 8, pp. 749–757, Nov. 2022, doi: 10.1016/J.EGYR.2021.12.009.

[9] A. Walker, “Future Challenges and Incoming Solutions in Emission Control for Heavy Duty Diesel Vehicles,” *Topics in Catalysis*, vol. 59, no. 8–9, pp. 695–707, May 2016, doi: 10.1007/S11244-016-0540-Z/FIGURES/19.

[10] “Compression Ignition - an overview | ScienceDirect Topics,” *ScienctDirect - Plant Engineer’s Reference Book (Second Edition)*, 2002. https://www.sciencedirect.com/topics/engineering/compression-ignition (accessed Mar. 09, 2022).

[11] I. G. Crow and K. Shippen, “Electricity generation,” *Plant Engineer’s Reference Book*, pp. 22-1-22–33, 2002, doi: 10.1016/B978-075064452-5/50077-8.

[12] “Diesel Fuel Injection - How-It-Works,” *MotorTrend*, 2022. https://www.motortrend.com/features/0706dp-diesel-fuel-injection/ (accessed Mar. 09, 2022).

[13] Knapp. M. , Kubitzek. A. , Obermeier. F. , Schneider. T. Chaves. H., “Experimental Study of Cavitation in the Nozzle Hole of Diesel Injectors Using Transparent Nozzles on JSTOR,” *SAE International*, 1995. https://www.jstor.org/stable/44633242?casa_token=Fh2roSdP8UIAAAAA%3AnrDWGVIoliRnZ-QKMP8SZFUBepJV8Phu9yA5y6ncik9A5y2g5yeHC0vQqJM3BUVTj0qnJguJ8KajhoEr2fjVgGNXL2LOiwPVgjDpUKuuxNPKSO5yONQ&seq=1#metadata_info_tab_contents (accessed Mar. 09, 2022).

[14] “Compression Ignition Engine - Definition, Main Components, Working with Application - Mechanical Booster,” *Mechanical Booster*, 2022. https://www.mechanicalbooster.com/2017/10/compression-ignition-engine.html (accessed Mar. 09, 2022).

[15] “Fuel Injection Fundamentals.” https://www.motortrend.com/how-to/1507-fuel-injection-fundamentals/ (accessed Mar. 09, 2022).

[16] S. Curran, R. M. Wagner, and S. Kokjohn, “In-Cylinder Fuel Blendingof Gasoline/Diesel for Improved Efficiencyand Lowest Possible Emissionson a Multi-Cylinder Light-Duty Diesel Engine,” *SAE International* , 2010, doi: 10.4271/2010-01-2206.

[17] “MECHANICALFUNDA for Mechanical Engineer,” *MechanicalFunda*, 2019. https://www.mechanicalfunda.com/2018/03/multi-point-fuel-injection-system.html (accessed Mar. 09, 2022).

[18] “DI Engine Guide - Direct Injection,” *Motortrend*, 2022. https://www.motortrend.com/how-to/hrdp-0909-direct-injection-guide/ (accessed Mar. 09, 2022).

[19] C. Wang, H. Xu, J. M. Herreros, J. Wang, and R. Cracknell, “Impact of fuel and injection system on particle emissions from a GDI engine,” *Applied Energy*, vol. 132, pp. 178–191, Nov. 2014, doi: 10.1016/J.APENERGY.2014.06.012.

[20] “Should You Buy a Car With Direct Injection? » AutoGuide.com News,” *AutoGuide*, 2022. https://www.autoguide.com/auto-news/2012/12/should-you-buy-a-car-with-direct-injection.html (accessed Mar. 09, 2022).

[21] “Natural gas and the environment - U.S. Energy Information Administration (EIA),” *The US Energy Information Administration*, 2021. https://www.eia.gov/energyexplained/natural-gas/natural-gas-and-the-environment.php (accessed Mar. 14, 2022).

[22] "Alternative Fuels Data Center," *United States Department of Energy - Clean Cities* , 2021. https://afdc.energy.gov/data/widgets/10661 (accessed Feb. 27, 2022).

[23] "Gasoline explained - U.S. Energy Information Administration (EIA)," *United States Energy Informatiion Administration (EIA)*, 2021. https://www.eia.gov/energyexplained/gasoline/ (accessed Mar. 09, 2022).

[24] "Alternative Fuels Data Center: Propane Basics." https://afdc.energy.gov/fuels/propane_basics.html (accessed Dec. 26, 2021).

[25] K. J. Morganti, T. M. Foong, M. J. Brear, G. da Silva, Y. Yang, and F. L. Dryer, "The research and motor octane numbers of Liquefied Petroleum Gas (LPG)," *Fuel*, vol. 108, pp. 797–811, 2013, doi: 10.1016/J.FUEL.2013.01.072.

[26] F. Poursadegh, "An experimental and theoretical investigation of direct fuel injection," 2017, Accessed: Mar. 09, 2022. [Online]. Available: http://minerva-access.unimelb.edu.au/handle/11343/129311

[27] J. Lacey *et al.*, "Optical Characterization of Propane at Representative Spark Ignition, Gasoline Direct Injection Conditions," in *SAE 2016 World Congress and Exhibition*, 2016, pp. 2016-01–0842. doi: 10.4271/2016-01-0842.

[28] D. Splitter, V. Boronat, F. D. F. Chuahy, and J. Storey, "Performance of direct injected propane and gasoline in a high stroke-to-bore ratio SI engine: Pathways to diesel efficiency parity with ultra low soot:," *https://doi.org/10.1177/14680874211006981*, vol. 22, no. 12, pp. 3475–3488, Apr. 2021, doi: 10.1177/14680874211006981.

[29] Y. Li, H. Guo, Z. Zhou, Z. Zhang, X. Ma, and L. Chen, "Spray morphology transformation of propane, n-hexane and iso-octane under flash-boiling conditions," *Fuel*, vol. 236, pp. 677–685, Jan. 2019, doi: 10.1016/J.FUEL.2018.08.160.

[30] J. Lacey *et al.*, "Generalizing the behavior of flash-boiling, plume interaction and spray collapse for multi-hole, direct injection," *Fuel*, vol. 200, pp. 345–356, 2017, doi: 10.1016/j.fuel.2017.03.057.

[31] J. K. Dukowicz, "A particle-fluid numerical model for liquid sprays," *Journal of Computational Physics*, vol. 35, no. 2, pp. 229–253, Apr. 1980, doi: 10.1016/0021-9991(80)90087-X.

[32] G. Tinarelli, D. Anfossi, S. Trini Castelli, M. Bider, and E. Ferrero, "A New High Performance Version of the Lagrangian Particle Dispersion Model Spray, Some Case Studies," *Air Pollution Modeling and Its Application XIII*, pp. 499–507, 2000, doi: 10.1007/978-1-4615-4153-0_51.

[33] J. B. Ghandhi, P. G. Felton, B. F. Gajdeczko, and F. v. Bracco, "Investigation of the Fuel Distribution in a Two-Stroke Engine with an Air-Assisted Injector," *SAE Technical Papers*, Mar. 1994, doi: 10.4271/940394.

[34] H. Guo, L. Nocivelli, R. Torelli, and S. Som, “Towards understanding the development and characteristics of under-expanded flash boiling jets,” *International Journal of Multiphase Flow*, vol. 129, p. 103315, Aug. 2020, doi: 10.1016/J.IJMULTIPHASEFLOW.2020.103315.

[35] F. Payri, J. v Pastor, J. M. Pastor, and J. E. Juliá, “Diesel Spray Analysis by Means of Planar Laser-Induced Exciplex Fluorescence,” *International Journal of Engine Research*, vol. 7, no. 1, pp. 77–89, 2006, doi: 10.1243/146808705X27723.

[36] F. J. Salvador, J. Gimeno, J. M. Pastor, and P. Martí-Aldaraví, “Effect of turbulence model and inlet boundary condition on the Diesel spray behavior simulated by an Eulerian Spray Atomization (ESA) model,” *International Journal of Multiphase Flow*, vol. 65, pp. 108–116, Oct. 2014, doi: 10.1016/J.IJMULTIPHASEFLOW.2014.06.003.

[37] “Numerical Study on Flash Boiling Spray of Multi-Hole Injector on JSTOR.” https://www.jstor.org/stable/26274119?casa_token=iN8D1G_8UlUAAAAA%3AsIPsOrES7qUpQkqUOnNSuw0wZO05Ftw4Gx_XF11bpZ45oDo-JiCZMCsEOhAQGh_VR0K8MNMo7iJoVURH0NAycMalyDpq6jshEHSA0GM01CMw5iEdZw&seq=6#metadata_info_tab_contents (accessed Mar. 15, 2022).

[38] S. K. Rachakonda, A. Paydarfar, and D. P. Schmidt, “Prediction of spray collapse in multi-hole gasoline direct-injection fuel injectors:,” *https://doi.org/10.1177/1468087418819527*, vol. 20, no. 1, pp. 18–33, Dec. 2018, doi: 10.1177/1468087418819527.

[39] R. Schlüßler, J. Gürtler, J. Czarske, and A. Fischer, “Planar fuel velocity measurements in the near-nozzle region of a high pressure Diesel injection nozzle,” in *18th International Symposium on the Application of Laser and Imaging Techniques to Fluid Mechanics*, 2016, pp. 1–13.

[40] L. A. Melton, “Spectrally separated fluorescence emissions for diesel fuel droplets and vapor,” *Applied Optics*, vol. 22, no. 14, pp. 2224–2226, 1983, doi: 10.1364/AO.22.002224.

[41] H. Fujimoto, Dae Choi, Y. Shima, J. Senda, and A. R. Jones, “Two-dimensional imaging of fuel-vapour concentration by use of LIEF technique during mixture formation process in a DI diesel engine,” *Measurement Science and Technology*, vol. 13, no. 3, p. 391, Feb. 2002, doi: 10.1088/0957-0233/13/3/322.

[42] R. Payri, J. Gimeno, P. Marti-Aldaravi, and M. Martínez, “Nozzle Flow Simulation of GDi for Measuring Near-Field Spray Angle and Plume Direction,” *SAE Technical Papers*, vol. 2019-April, no. April, Apr. 2019, doi: 10.4271/2019-01-0280.

[43] P. Rogler, R. Grzeszik, S. Arndt, and M. Aigner, “3D analysis of vapor and liquid phase of GDI injectors using laser induced exciplex fluorescence tomography in a high pressure/high temperature spray chamber,” *SAE Technical Papers*, Jul. 2007, doi: 10.4271/2007-01-1827.

[44] F. Poursadegh *et al.*, "On the phase and structural variability of directly injected propane at spark ignition engine conditions," *Fuel*, vol. 222, pp. 294–306, 2018, doi: 10.1016/j.fuel.2018.02.137.

[45] B. A. Sforzo *et al.*, "X-ray Characterization and Spray Measurements of ECN Spray G Using Alternative Fuels Under Flashing Conditions," *ILASS Americas*, 2019.

[46] P. Downar-Zapolski, Z. Bilicki, L. Bolle, and J. Franco, "The non-equilibrium relaxation model for one-dimensional flashing liquid flow," *International Journal of Multiphase Flow*, vol. 22, no. 3, pp. 473–483, 1996, doi: 10.1016/0301-9322(95)00078-X.

[47] M. Adachi, V. G. McDonell, D. Tanaka, J. Senda, and H. Fujimoto, "Characterization of Fuel Vapor Concentration Inside a Flash Boiling Spray," *SAE Technical Papers*, Feb. 1997, doi: 10.4271/970871.

[48] P. H. Mesman and B. Veenhuizen, "The Spray Behavior of Liquid LPG at Different Back Pressures During Injection in a Constant Volume Chamber," *SAE Technical Papers*, Jun. 2009, doi: 10.4271/2009-01-1834.

[49] Y. L. Qi, B. Y. Xu, and S. L. Cai, "An application of digital image processing techniques to the characterization of liquid petroleum gas (LPG) spray," *Measurement Science and Technology*, vol. 17, no. 12, p. 3229, Nov. 2006, doi: 10.1088/0957-0233/17/12/005.

[50] J. Lacey *et al.*, "Flash vaporization of propane in an optically accessible, directly injected engine," *International Journal of Engine Research*, vol. 22, no. 2, pp. 685–696, 2021, doi: 10.1177/1468087419849989.

[51] S. E. Parrish, "Evaluation of Liquid and Vapor Penetration of Sprays from a Multi-Hole Gasoline Fuel Injector Operating Under Engine-Like Conditions," *SAE International Journal of Engines*, vol. 7, no. 2, pp. 1017–1033, 2014, [Online]. Available: https://www.jstor.org/stable/26277820

[52] W. Zeng, M. Xu, M. Zhang, Y. Zhang, and D. J. Cleary, "Macroscopic characteristics for direct-injection multi-hole sprays using dimensionless analysis," *Experimental Thermal and Fluid Science*, vol. 40, pp. 81–92, 2012, doi: 10.1016/j.expthermflusci.2012.02.003.

[53] H. Guo, L. Nocivelli, and R. Torelli, "Numerical study on spray collapse process of ECN spray G injector under flash boiling conditions," *Fuel*, vol. 290, p. 119961, 2021, doi: 10.1016/j.fuel.2020.119961.

[54] L. Allocca *et al.*, "ECN Spray G Injector: Assessment of Numerical Modeling Accuracy," *SAE Technical Papers*, vol. 2018-April, Apr. 2018, doi: 10.4271/2018-01-0306.

[55] "Spray G Parametric Variation – Engine Combustion Network," *Engine Combustion Network*. https://ecn.sandia.gov/gasoline-spray-combustion/target-condition/spray-g-parametric-variation/ (accessed Dec. 20, 2021).

[56] B. Mohan, J. Badra, J. Sim, and H. G. Im, "Coupled in-nozzle flow and spray simulation of Engine Combustion Network Spray-G injector," *International Journal of Engine Research*, vol. 22, no. 9, pp. 2982–2996, 2021, doi: 10.1177/1468087420960612.

[57] J. Hwang, L. Weiss, I. K. Karathanassis, P. Koukouvinis, L. M. Pickett, and S. A. Skeen, "Spatio-temporal identification of plume dynamics by 3D computed tomography using engine combustion network spray G injector and various fuels," *Fuel*, vol. 280, p. 118359, 2020, doi: 10.1016/j.fuel.2020.118359.

[58] C. K. Mohapatra *et al.*, "Collaborative investigation of the internal flow and near-nozzle flow of an eight-hole gasoline injector (Engine Combustion Network Spray G)," *International Journal of Engine Research*, p. 1468087420918449, 2020, doi: 10.1177/1468087420918449.

[59] L. Sileghem *et al.*, "Laminar burning velocity of gasoline and the gasoline surrogate components iso-octane, n-heptane and toluene," *Fuel*, vol. 112, pp. 355–365, 2013, doi: 10.1016/j.fuel.2013.05.049.

[60] K. J. Richards, P. K. Senecal, and E. Pomraning, "CONVERGE 3.0*." Convergent Science, Madison, WI, 2021.

[61] L. Nocivelli *et al.*, "Analysis of the Spray Numerical Injection Modeling for Gasoline Applications," *SAE Technical Papers*, vol. 2020-April, no. April, Apr. 2020, doi: 10.4271/2020-01-0330.

[62] L. Nocivelli, J. Yan, K. Saha, G. M. Magnotti, C. F. Lee, and S. Som, "Effect of Ambient Pressure on the Behavior of Single-Component Fuels in a Gasoline Multi-Hole Injector," *ASME 2019 Internal Combustion Engine Division Fall Technical Conference, ICEF 2019*, Dec. 2019, doi: 10.1115/ICEF2019-7258.

[63] Z. Yue, M. Battistoni, and S. Som, "Spray characterization for engine combustion network Spray G injector using high-fidelity simulation with detailed injector geometry," *International Journal of Engine Research*, p. 146808741987239, 2019, doi: 10.1177/1468087419872398.

[64] B. Windell *et al.*, "Bulk Spray and Individual Plume Characterization of LPG and Iso-Octane Sprays at Engine-Like Conditions," Mar. 2022, Accessed: Mar. 15, 2022. [Online]. Available: https://www.sae.org/publications/technical-papers/content/2022-01-0497/

[65] P. K. Senecal *et al.*, "A New Parallel Cut-Cell Cartesian CFD Code for Rapid Grid Generation Applied to In-Cylinder Diesel Engine Simulations," *SAE Technical Papers*, Apr. 2007, doi: 10.4271/2007-01-0159.